The Dissertation Committee for Seungsoo Kim
Certifies that this is the approved version of the following dissertation:

Ultrasound and Photoacoustic Imaging for Cancer Detection and Therapy Guidance

Committee:

Stanislav Y. Emelianov, Supervisor

Salavat R. Aglyamov

Konstantin V. Sokolov

Mark F. Hamilton

John A. Pearce

Ultrasound and Photoacoustic Imaging
for Cancer Detection and Therapy Guidance

by

Seungsoo Kim, B.E.; M.S.E.E.

Dissertation

Presented to the Faculty of the Graduate School of
The University of Texas at Austin
in Partial Fulfillment
of the Requirements
for the Degree of

Doctor of Philosophy

The University of Texas at Austin
August 2011

Dedicated to my wife, Jiyoung Ko, for her love and belief

and to my family members for their continuous support

Acknowledgements

The past four years at the University of Texas at Austin will never be forgotten in my life. All professors, colleagues and friends whom I've met in Austin truly deserve to share this accomplishment. Without their support, this dissertation would have never been possible.

First of all, I sincerely thank Prof. Stanislav (Stas) Emelianov for supervising, encouraging, financially supporting and being patient with me. He was always besides me and carefully listened to my ideas and thoughts, and kindly gave me the right direction to achieve those. Without his advice, I might have lost my way toward the end of this Ph.D. journey.

I would also like to express my gratitude and appreciation to Dr. Salavat Aglyamov. He's been a great friend as well as teacher to me. He always gave me correct answers whenever I asked him about theoretical and/or mathematical questions. Also, I'll never forget our several trips including 15-hour one-way driving to Santa Fe for attending a conference and multiple trips to Houston for the prostate study.

I am also greatly thankful to other committee members, Dr. Konstantin (Kostia) Sokolov, Dr. Mark Hamilton and Dr. John Pearce for their advice to make this dissertation move in the right direction.

There are so many individuals, who helped me for this dissertation in their own ways, in the lab from the age of Panscopic Laboratory to the age of Ultrasound Imaging and Therapeutic Research Laboratory. Dr. Suhyun Park and Dr. Jignesh Shah initiated projects (i.e., elasticity imaging and photothermal therapy, respectively) that I have conducted. Without their efforts in an early stage of these studies, I could never accomplish the goal of this dissertation. Dr. Shriram Sethuraman initiated IVUS and

IVPA projects, and therefore I could continue the study regarding IVUS image reconstruction. Dr. Srivalleesha Mallidi contributed to animal imaging protocol and spectroscopic photoacoustic imaging, and thus I could perform *in-vivo* experiments and continue the study regarding optical absorption spectral analysis algorithm. I would also like to thank Dr. Andrei Karpiouk for his help in laser systems, Dr. Wolfgang Frey for advice to my research, Dr. Kimberly Homan for her contribution to the wet lab, Dr. Bo Wang for her efforts to the dry lab and helping me use the Volcano system, Mohammad Mehrmohammardi for helping me settle down in Austin, Jimmy Su for his pioneer spirit in marriage life such as having a baby and becoming a father prior to me, Jason Cook for his strength, Sangpil Yoon for many conversations, Yun-Sheng Chen for nanoparticles, Doug Yeager for silence in the office, Seung Yun Nam and Soon Joon Yoon for being Koreans in the lab, Min Qu for doing TA together, Geoff Luke for many discussions, Alex Hannah for organizing my graduation party, Katie Wilson for delicious cup cakes, Pratixa Joshi for collaborating macrophage study, Iulia Graf, Carolyn Bayer, and Richard Bouchard for helping me in many aspects as post-doctoral fellows, and Tera Sherrard for her great help in administrative stuffs.

I can never explain this accomplishment without mentioning my former supervisor, Dr. Tai-Kyong Song, who introduced me to the ultrasound world. I sincerely appreciate his advice, support, motivation, and encouragement when I was at Sogang University, Seoul, Korea.

The last but not the least persons whom I would like to thank are my family members. My wife, Jiyoung Ko, truly deserves my appreciation. Without her love, belief, and support, I could never accomplish my Ph.D. study. She always understood me and tried to support me in many ways. I dedicate this dissertation to Jiyoung. I also thank my parents, Yeungeui Kim and Insoo Park, and parents-in-law, Wonmyoung Ko and

Moonsook Park, for their unconditional love and support. I promise I’ll repay them for all their love.

Ultrasound and Photoacoustic Imaging for Cancer Detection and Therapy Guidance

Seungsoo Kim, Ph.D.

The University of Texas at Austin, 2011

Supervisor: Stanislav Y. Emelianov

Cancer has been one of main causes of human deaths for many years. Early detection of cancer is essential to provide definitive treatment. Among many cancer treatment methods, nanoparticle-mediated photothermal therapy is considered as one of the promising cancer treatment methods because of its non-invasiveness and cancer-specific therapy. Ultrasound and photoacoustic imaging can be utilized for both cancer detection and photothermal therapy guidance. Ultrasound elasticity imaging can detect cancer using tissue elastic properties. Once cancer is diagnosed, spectroscopic photoacoustic imaging can be used to monitor nanoparticle delivery before photothermal therapy. When nanoparticles are well accumulated at the tumor, ultrasound and photoacoustic-based thermal imaging can be utilized for estimating temperature distribution during photothermal therapy to guide therapeutic procedure.

In this dissertation, ultrasound beamforming, elasticity imaging, and spectroscopic photoacoustic imaging methods were developed to improve cancer detection and therapy guidance. Firstly, a display pixel based synthetic aperture focusing method was developed to fundamentally improve ultrasound image qualities. Secondly, an autocorrelation based sub-pixel displacement estimation method was developed to enhance signal-to-noise ratio of elasticity images. The developed elasticity imaging method was utilized to clinically evaluate the feasibility of using ultrasound elasticity imaging for prostate cancer detection. Lastly, a minimum mean square error based spectral separation method was developed to robustly utilize spectroscopic photoacoustic imaging. The developed spectroscopic photoacoustic imaging method was utilized to demonstrate ultrasound and photoacoustic image-guided photothermal cancer therapy using *in-vivo* tumor-bearing mouse models. The results of these studies suggest that ultrasound and photoacoustic imaging can assist both cancer detection and therapy guidance.

Table of Contents

List of Tables xiv

List of Figures xv

Chapter 1: *Introduction* 1

1.1 Ultrasound Imaging 1

1.1.1 Beamforming 3

1.1.2 Spatial Resolution 6

1.1.3 Elasticity Imaging 7

1.1.4 Ultrasound-based Thermal Imaging 10

1.2 Photoacoustic Iimaging..10

1.2.1 Fundamentals of Photoacoustics 11

1.2.2 Nanoparticles 13

1.2.3 Spectroscopic Photoacoustic Imaging 14

1.2.4 Photoacoustic-based Thermal Imaging........................16

1.3 Photothermal Therapy..17

1.4 Organization of the Dissertation 17

References..20

SECTION 1: *ULTRASOUND IMAGE RECONSTRUCTION* 25

Chapter 2: *Display Pixel-based Synthetic Aperture Focusing Method for Intravascular Ultrasound Imaging* 25

Abstract..25

2.1 Introduction...26

2.2 Intravascular Ultrasound Image Reconstruction....................................27

2.2.1 Synthetic Aperture Focusing.......................................27

2.2.2 Digital Scan Converter..27

2.2.3 Display Pixel-based Focusing.....................................28

2.2.4 Phase Rotation Beamforming 29

2.3 Materials and Methods..30

2.4 Results and Discussion 31

2.4.1 Point Spread Function and Contrast-to-Noise Ratio..................31

2.4.2 Computational Complexity...34

2.5 Conclusion 35

References..35

SECTION 2: *CANCER DETECTION USING ULTRASOUND ELASTICITY IMAGING*...37

Chapter 3: *An Autocorrelation-based Method for Improvement of Sub-pixel Displacement Estimation in Ultrasound Elasticity Imaging* 37

Abstract 37

3.1 Introduction...38

3.2 Approach..39

3.3 Materials and Methods..42

3.3.1 Simulated Phantom 42

3.3.2 Tissue-mimicking Phantom and Data Acquisition 42

3.3.3 Processing Algorithm and Signal-to-Noise Ratio......................43

3.3.4 Computational Complexity...45

3.4 Results and Discussion 45

3.4.1 Axial Displacements 45

3.4.2 Lateral Displacements...46

3.5 Conclusion 48

References..48

Chapter 4: *Ultrasound Elasticity Imaging for Prostate Cancer Detection: Initial Clinical Study*...50

Abstract 50

4.1 Introduction...50

4.2 Materials and Methods..52

4.2.1 Patients 52

4.2.2 Data Acquisition and Elasticity Imaging Algorithm 52

4.3 Results and Discussion 55

4.3.1 Comparison between *In-vivo* and *Ex-vivo* Results......................55
4.3.2 Transversal Plane vs. Sagittal Plane 57
4.3.3 Non-uniform Stress Field by Convex Array Transducer............59
4.3.4 Lateral Motion by Convex Array Transducer.............................60
4.4 Conclusion 61
References...61

SECTION 3: *PHOTOTHERMAL CANCER THERAPY GUIDED BY ULTRASOUND AND PHOTOACOUSTIC IMAGING*..............................63

Chapter 5: *In vivo Three-dimensional Spectroscopic Photoacoustic Imaging for Monitoring Nanoparticle Delivery* 63
Abstract...63
5.1. Introduction..64
5.2. Materials and Methods...65
5.2.1 Nanoparticles 65
5.2.2 Mouse bearing a subcutaneous tumor...66
5.2.3 *In vivo* imaging system 67
5.2.4 Spectroscopic photoacoustic imaging...69
5.2.5 Histological analysis (silver staining)...74
5.3. Results...75
5.4. Discussion...80
5.5. Conclusion 81
References..81

Chapter 6: *Ultrasound and Photoacoustic Image-guided Photothermal Therapy using Silica-coated Gold Nanorods: In-vivo Study* 85
Abstract...85
6.1 Introduction..85
6.2 Materials and Methods...87
6.2.1 *In-vivo* Mouse Model of Cancer 87
6.2.2 Silica-coated Gold Nanorods 87
6.2.3 Mouse Imaging Setup and Data Acquisition 87

6.2.4 Spectroscopic Photoacoustic Imaging 89
6.2.5 Photoacoustic-based Thermal Imaging.....................................90
6.3 Results and Discussion 90
6.3.1 Monitoring of Nanoparticle Delivery Before Therapy 90
6.3.2 Monitoring of Temperature Rise During Therapy.....................91
6.4 Conclusion 94
References...95

Chapter 7: *Conclusions and Future Work* 97
7.1 Summary...97
7.2 Physiological Motion in Ultrasound-based Thermal Imaging...............99
7.3 Optical Absorption Spectra Separation in Spectroscopic Photoacoustic Imaging 101
7.4 3-D Photoacoustic Beamforming...103
7.5 Spectroscopic Photoacoustic Imaging for Monitoring Macrophage Cells with Nanoparticles 105
7.6 Ultrasound Elasticity Imaging for Monitoring Photothermal Therapeutic Outcomes 106
7.7 Conclusions...107
References...108

Bibliography 110

Vita 121

List of Tables

Table 2.1: IVUS imaging conditions 34

List of Figures

Figure 1.1: Block diagram of ultrasound imaging system (HV MUX: high voltage multiplexer, TxBF: transmit beamformer, RxBF: receive beamformer, ATGC: analog time gain compensator, LPF: low pass filter, ADC: analog-to-digital convertor, DSC: digital scan convertor).................3

Figure 1.2: Simulated ultrasound beam pattern produced by (a) unfocused transducer and (b) transducer focused at 30 mm. The same central frequency of 4 MHz was used for both. (Adapted from [21])...........4

Figure 1.3: 1-D aperture model...5

Figure 1.4: (a) Modeling of array element transducer and (b) corresponding beam pattern...6

Figure 1.5: Block diagram of ultrasound elasticity imaging................................9

Figure 1.6: Block diagram of photoacoustic imaging system............................11

Figure 1.7: Optical absorption of tissue (Adapted from [45])............................13

Figure 1.8: Optical absorption spectra of gold nanoparticles with different shapes (Adapted from [47])..14

Figure 2.1: Graphical representation of bilinear interpolation in the DSC.........28

Figure 2.2: Illustration of IVUS image reconstruction. Crosses represent focused data on scan-lines. Circles represent display pixels on the screen....29

Figure 2.3: IVUS images of point targets obtained using the SAF method with (a) 64 beams and (b) 256 beams, then converted into 512 by 512 pixels, and (c) using the DPBSAF method with 512 by 512 pixels. The dynamic range of all images is 40 dB. The second row images are zoomed-in point targets positioned at 4.5-mm apart from the center of a catheter. Clearly, the image obtained using the DPBSAF method has better angular resolution compared to images obtained using the SAF method. 32

Figure 2.4: Angular profile of the point spread function at (a) 2.6, (b) 4.5, and (c) 7.9mm apart from the center of a catheter. In each graph, the DPBSAF method compares with the SAF method. At all positions, the DPBSAF method has better performance, especially for the farther position from the catheter. 32

Figure 2.5: PVA phantom images obtained using (a) the SAF method with 256 beams, and (b) the DPBSAF method with 300 by 300 pixels. All images are shown using 40 dB display dynamic range. 33

Figure 2.6: Rabbit artery images obtained using (a) the SAF method with 256 beams, and (b) the DPBSAF method with 300 by 300 pixels. All images are shown using 40 dB display dynamic range. 33

Figure 2.7: MPUs for the SAF with 256 and 512 beams, and the DPBSAF method. 35

Figure 3.1: Block diagram of the autocorrelation-based method for improved sub-pixel displacement estimation. The autocorrelation output denotes displacement estimation errors related to the intrinsic method and speckle statistics. Clearly, outputs of the autocorrelation-based method do not have high frequency noise caused by sub-pixel estimation errors. The autocorrelation approach based on (a) reference frame and (b) both reference and displaced frames. 41

Figure 3.2: Ultrasound images of (a) simulated phantom and (b) the tissue mimicking phantom. Regions of interest (ROIs) for axial and lateral displacements are outlined by dotted and dashed lines, respectively.44

Figure 3.3: Axial and lateral displacement SNR for 0.3% to 1.5% axial deformations in 0.3% increments. (a) and (d) are for axial and lateral displacement SNR from the simulated phantom while (b) and (e) are from the tissue-mimicking phantom. (c) and (f) indicate computational cost comparisons for axial and lateral displacement estimators, respectively. 48

Figure 4.1: (a) Prostate anatomy and zones, (b) transversal plane of prostate, and (c) sagittal plane of prostate (Adapted from Nature Review Cancer)....53

Figure 4.2: ex-vivo elasticity imaging examination 54

Figure 4.3: Prostate ultrasound and elasticity images of (a) *in-vivo* and (b) *ex-vivo* examination (case #5). Outlines on images are manually drawn based on ultrasound and elasticity imaging results. 55

Figure 4.4: pathological analysis of the excised prostate (case #5). 56

Figure 4.5: Ultrasound and elasticity images of transversal and sagittal planes obtained from (a) case #8 and (b) case #11. Pathological analysis is also shown here to compare it with elasticity imaging results. 58

Figure 4.6: Example of strain image induced non-uniform stress field (case #9).59

Figure 4.7: Example of strain image when lateral motion is induced (case #9). 60

Figure 5.1: The absorption spectra of deoxyhemoglobin (Hb, blue dashed line) and oxyhemoglobin (HbO2, red dash-dotted line) [17] compared to the absorbance spectrum of the PEGylated gold nanorod (PEG-Au NR, green solid line) measured by UV-Vis spectroscopy. Dots on each line correspond to wavelengths used for spectroscopic photoacoustic imaging. The transmission electron microscopy (TEM) image of PEG-Au NRs is also shown. 66

Figure 5.2: Schematic diagram of the developed *in vivo* three-dimensional ultrasound and photoacoustic imaging system. 69

Figure 5.3: Schematic diagram of the developed spectroscopic photoacoustic imaging algorithm. 72

Figure 5.4: Comparison between linear least square (LLS) and minimum mean square error (MMSE) methods. Ultrasound image (a) was used for the skin-tissue segmentation. The fluence compensated photoacoustic image (b) at 800 nm is shown as a reference. Spectral analysis based on LLS method can produce negative concentrations (c) of optical absorbers due to imperfect fluence compensations, noisy measurements, etc. The regions producing a negative NP concentration by LLS method get removed from the NP image. (d). However, the developed MMSE method can reliably reconstruct spatial distribution and concentration of NP – white arrows in panel (e) indicate locations where NP concentrations were recovered using MMSE method. 76

Figure 5.5: Three-dimensional ultrasound images (panels a,g), photoacoustic images (panels b,h), and PA-derived oxygen saturation images (SO_2, panels c,i), and images of oxyhemoglobin ($C[HbO_2]$, panels d,j), deoxyhemoglobin (C[Hb], panels e,k), and nanoparticle (C[NP], panels f,l) concentration before and 31 hours after tail vein injection of PEGylated gold nanorods into tumor bearing mouse. PA and PA-derived images are shown with ultrasound images in the background. Oxygen saturation was calculated using the concentrations of oxyhemoglobin and deoxyhemoglobin. Furthermore, anatomical features of the tumor (i.e., tumor size and location) are better shown in rotating 3-D images: ultrasound (panel g), 3-D photoacoustics (panel h), oxygen saturation (panel i), and nanoparticle concentration (panel l). 78

Figure 5.6: (a) Photograph of the mouse with dotted lines indicating the approximate location of imaging planes and corresponding histological slides. (b) PA-derived maps of NP concentration displayed over the ultrasound images of the tumor. (c) Silver stained tissue slides where gray to black colors indicate presence of NPs. The enlarged areas of silver stained slides are shown in panels (d) and (e)........................79

Figure 6.1: Block diagram of mouse imaging setup..88

Figure 6.2: 3-D ultrasound, photoacoustic, and spectroscopic photoacoustic images of before nanoparticle injection (a~e), and after the injection (f~j). (a) and (f) (ultrasound images) show tumor size and location. (b) and (g) are photoacoustic images obtained at wavelength of 800 nm. (c) and (h), (d) and (i), and (e) and (j) show oxygenated hemoglobin, deoxygenated hemoglobin, and nanoparticle distributions, respectively. Color bars for spectroscopic photoacoustic images (red, blue, and yellow) represent 50% to 100% of relative concentrations of oxygenated hemoglobin, deoxygenated hemoglobin, and nanoparticles, respectively. The field of view (FOV) for each volume is 22.4 mm (width) by 25.8 mm (depth) by 20.0 mm (length)..92

Figure 6.3: Combined ultrasound and photoacoustic images, and photoacoustic-based thermal images are shown in (a~c) and (d~f), respectively. The white arrow represents the direction of CW laser irradiation (808 nm, 1 W). (d) Photothermal therapy of 5 minutes result in maximum temperature rise of about 19°C in the tumor...................................93

Figure 6.4: (a) Nanoparticle distribution obtained from spectroscopic photoacoustic imaging and (b) temperature distribution after 3 minutes of therapy obtained from photoacoustic-based thermal imaging. Both nanoparticle and temperature distribution are closely related to each other. 94
Figure 7.1: Temperature estimation by ultrasound-based thermal imaging. 100
Figure 7.2: Spectroscopic photoacoustic images obtained at (a) before nanoparticle injection, (b) 6 hours and (c) 24 hours after the injection. Macrophage loaded with nanospheres of which absorption peak was around 530 nm was injected..102
Figure 7.3: Normalized optical absorption specta of oxygenated hemoglobin (red), deoxygenated hemoglobin (blue), and macrophage cells loaded with nanospheres (green). 103
Figure 7.4: 3-D photoacoustic imaging by (a) 2-D beamforming and (b) 3-D beamforming. 104
Figure 7.5: Spectroscopic photoacoustic imaging results to evaluate the feasibility of using macrophage cells for delivering nanoparticles. 106
Figure 7.6: Ultrasound elasticity imaging for accessing photothermal therapeutic outcomes. Black dotted line indicates tumor. 107

Chapter 1: *Introduction*

Cancer is the second leading cause of death in the United States, exceeded only by heart disease. According to the American Cancer Society, there are about 1.6 million estimated new cases of cancer and about 572,000 estimated deaths caused by cancer in the United States in 2011 [1].

Ultrasound and photoacoustic imaging techniques can be used for both cancer detection and therapy guidance [2-16]. Ultrasound elasticity imaging can assist the cancer detection. Spectroscopic photoacoustic imaging can monitor nanoparticle delivery before photothermal therapy. Ultrasound and photoacoustic-based thermal imaging can non-invasively estimate temperature distribution during photothermal therapy [12, 13].

1.1 ULTRASOUND IMAGING

Ultrasound imaging is a real-time, cost-effective, and non-ionizing medical imaging modality. In ultrasound imaging, tissue anatomy can be obtained based on mainly two wave effects: *reflection* and *scattering* [17]. When the short pulsed ultrasonic wave is transmitted to the body, the wave travels through many different layers of tissues. Each layer of tissues will have different density and speed of sound resulting in acoustical impedance mismatch between two layers.

The acoustical impedance (Z) is defined as

$$Z = \rho c, \tag{1.1}$$

where ρ is the density of the material [kg/m^3] and c is the speed of sound [m/s]. Because of difference in impedance at the boundary, some part of the transmitted waves is reflected from the boundary, and the other part of waves continues to propagate through the tissue. Those reflected ultrasound signals are used for the reconstruction of ultrasound images. Along with the reflection, scattering plays a great role in ultrasound imaging.

Because of small size of scatterers (i.e., below the acoustical wavelength) and irregularities of their acoustical impedance, ultrasound waves are not just reflected, but also redirected from their original direction. The scattering effect generates very unique speckle patterns on an ultrasound image due to constructive and destructive compositions of multiple scattered waves from the specific distribution of scatterers.

A typical two-dimensional (2-D) ultrasound imaging system equipped with an array transducer is presented in Figure 1.1. The array element transducer is used for both transmitting and receiving ultrasound waves. In a transmission side, a transmit-beamformer (TxBF) triggers pulsers at different timings based on a transmit-focal depth. These high voltage electrical pulses are converted into pressure waves via piezoelectric materials inside the transducer. The transmitted ultrasound waves are reflected from tissue boundaries and scattered from scatterers in tissues. The echo signals are again converted into electrical voltages through the transducer. The received signals are first compensated for depth-dependent attenuations using an analog time gain compensator (ATGC), and then converted into digital signals via an analog-to-digital convertor (ADC). Since the diagnostic ultrasound signals transmitted to the tissue are typically ranging from 3 to 15 MHz, the sampling frequency of ADCs in ultrasound imaging systems is usually 40 MHz satisfying the Nyquist criterion. In order to avoid aliasing artifacts, an anti-aliasing low pass filter (LPF) is placed between ATGC and ADC. The digitized signals are then dynamically focused at each depth using a receive-beamformer (RxBF) [18]. After beamforming, several different imaging modes such as brightness-mode (b-mode), Doppler-mode, and elasticity-mode require their own processing blocks. Finally, a digital scan conversion is performed to display ultrasound images on the screen [19].

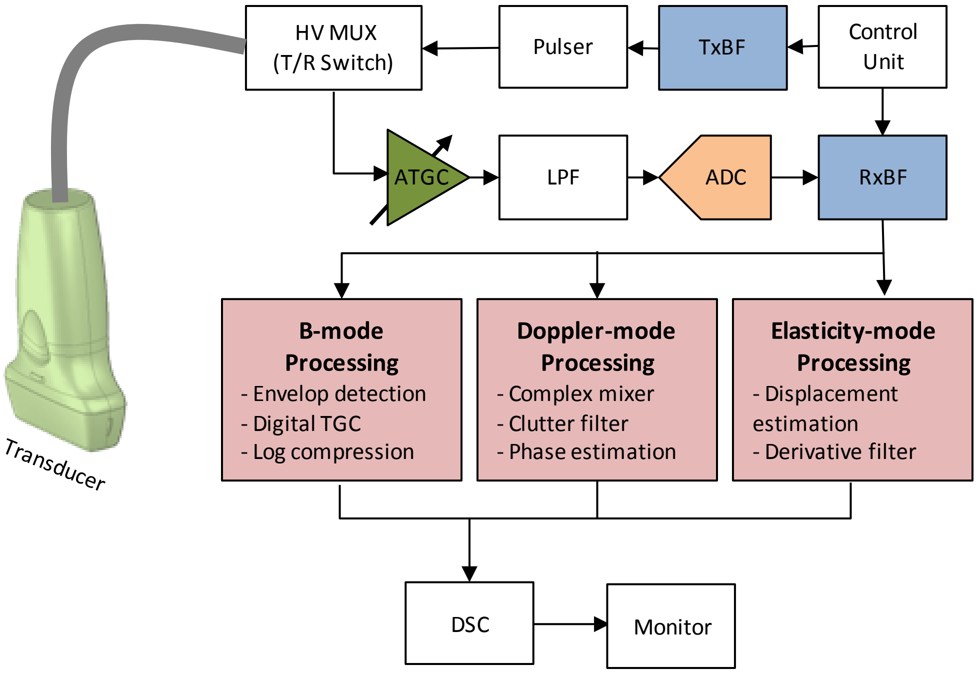

Figure 1.1: Block diagram of ultrasound imaging system (HV MUX: high voltage multiplexer, TxBF: transmit beamformer, RxBF: receive beamformer, ATGC: analog time gain compensator, LPF: low pass filter, ADC: analog-to-digital convertor, DSC: digital scan convertor)

1.1.1 Beamforming

Beamforming is the most important part in ultrasound image reconstruction because spatial resolution of an ultrasound image relies on it [20]. Figure 1.2 shows ultrasonic beam patterns (i.e. spatial distributions of ultrasound pressure) in water produced by single element unfocused (Figure 1.2(a)) and focused (Figure 1.2(b)) ultrasound transducers at the central frequency of 4 MHz. The graphs clearly show how focusing is important to have narrower beam pattern resulting in finer spatial resolution of an ultrasound image.

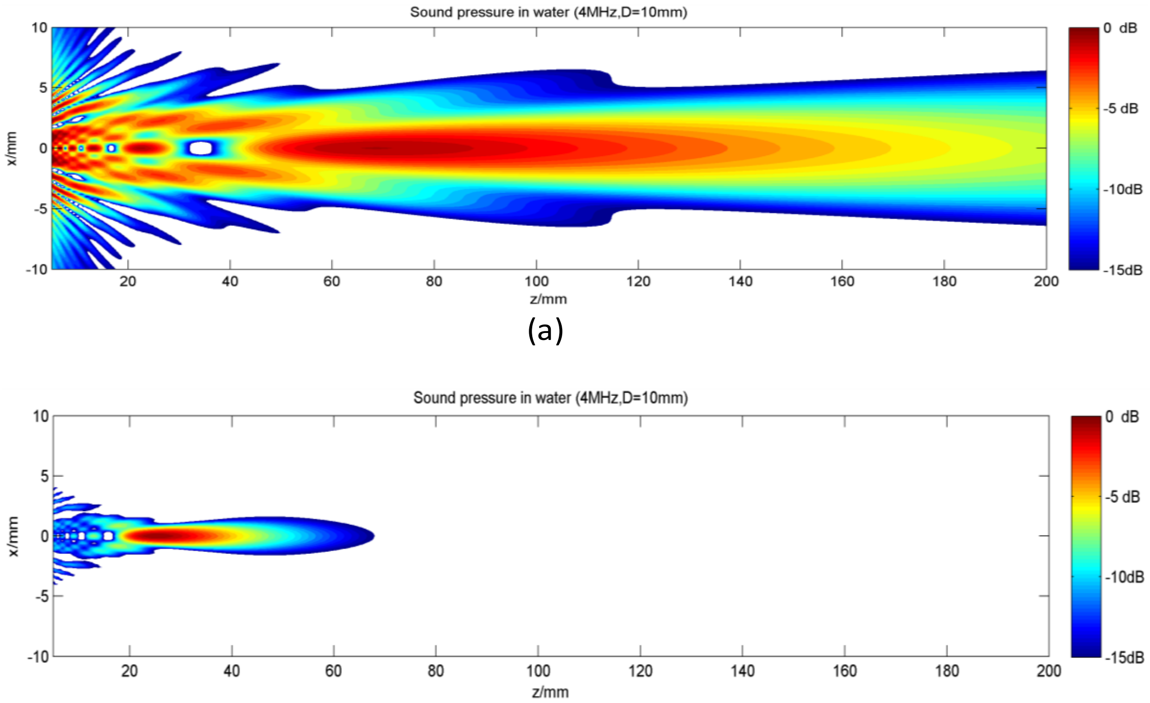

(a)

(b)

Figure 1.2: Simulated ultrasound beam pattern produced by (a) unfocused transducer and (b) transducer focused at 30 mm. The same central frequency of 4 MHz was used for both. (Adapted from [21])

The beam pattern shown in Figure 1.2 can be explained by the one of wave effects: *diffraction*. Every point along the transducer aperture can be modeled as an isotropic radiator of sound. The pressure (p) generated by the isotropic radiator can be defined by

$$p(r) = \frac{e^{ikr}}{r}, \tag{1.2}$$

where r is the distance from the radiator source and k is the wave number defined by

$$k = \frac{\omega_0}{c} = \frac{2\pi}{\lambda_0}, \tag{1.3}$$

where c is the speed of sound, ω_0 is the radial frequency, and λ_0 is the wavelength. Since the 1-D aperture presented in Figure 1.3 can be modeled as the sum of multiple point sources on the aperture, the pressure distribution (i.e., beam pattern) in a 2-D plane can be defined by

$$p(z, x_z) = \int_{-a_0}^{+a_0} \frac{e^{ikd(x, x_z)}}{d(x, x_z)} dx . \tag{1.4}$$

Since only the small angle region with respect to the beam direction is interesting to analyze, the following constraint can be applied:

$$z^2 >> (x - x_z)^2 . \tag{1.5}$$

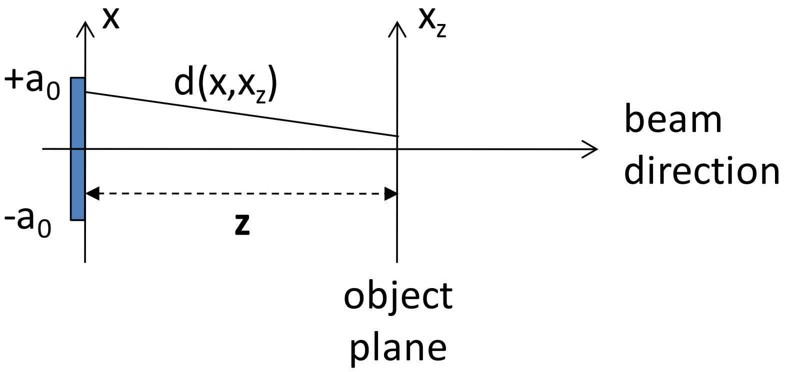

Figure 1.3: 1-D aperture model

This approximation called ‘small angle’ or ‘Fresnel’ approximation converts the original equation (1.4) into:

$$p(z, x_z) = \frac{e^{ikz} e^{ik\frac{x_z^2}{2z}}}{z} \int_{-\infty}^{\infty} a(x) e^{-ik\frac{xx_z}{z}} e^{ik\frac{x^2}{2z}} dx , \tag{1.6}$$

where *a(x)* is the aperture function.

Beamforming is basically to remove the quadratic phase term inside the integral operation in equation (1.6). As a result, the beam pattern in the field after beamforming can be viewed simply as Fourier transform of the aperture function:

$$\begin{aligned} p(z, x_z) &\propto \int_{-\infty}^{\infty} a(x) e^{-i\left(\frac{kx_z}{z}\right)x} dx \\ &\propto F\left[a(x)\right]_{f=\frac{x_z}{\lambda z}} \end{aligned} . \tag{1.7}$$

Figure 1.4 presents how a beam pattern produced by an array element transducer can be estimated based on transducer parameters such as width of transducer (*A*), element pitch (*p*) and element width (*w*).

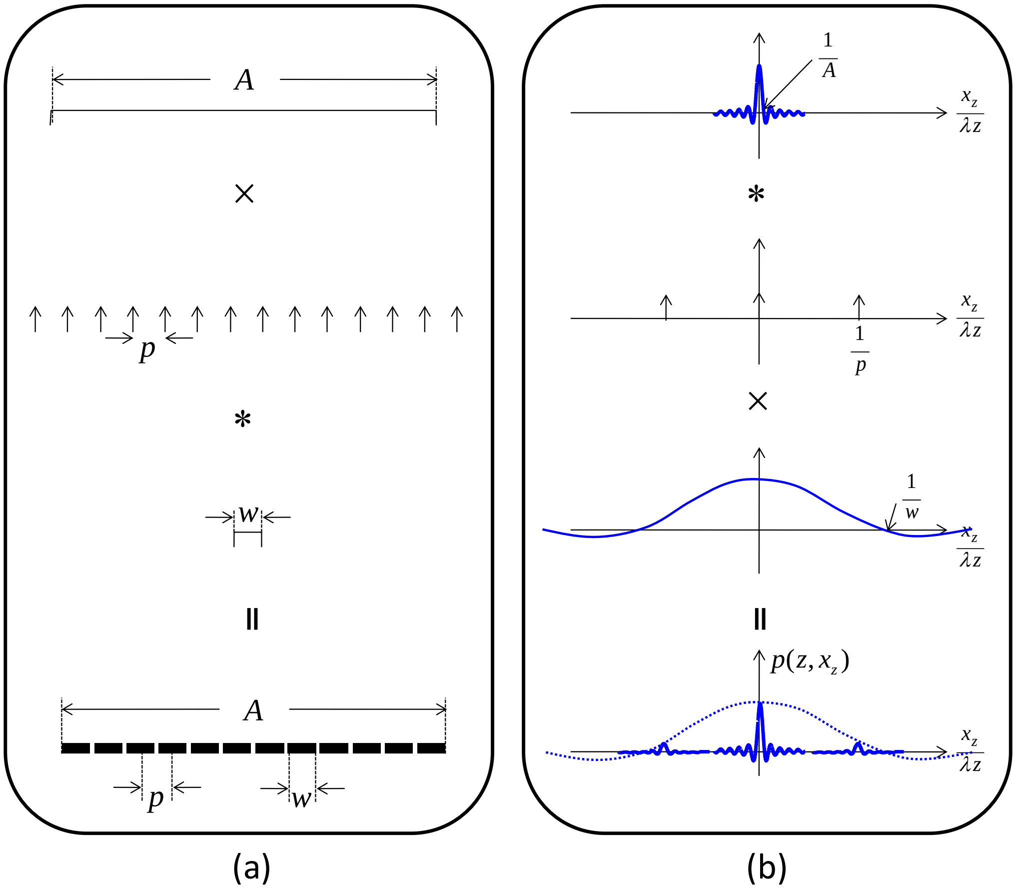

Figure 1.4: (a) Modeling of array element transducer and (b) corresponding beam pattern

1.1.2 Spatial Resolution

In ultrasound imaging, spatial resolutions are determined by the characteristics of the transducer and the transmitted ultrasound signal.

Spatial resolution of ultrasound images is divided into three parts: axial, lateral, and elevational resolutions along with each axis. The axial axis is in the beam propagation direction while the lateral axis is perpendicular to the beam direction. Therefore, the axial and lateral axes define a 2-D ultrasound imaging plane. The elevational axis is perpendicular to the imaging plane. The axial resolution is mainly determined by the central frequency and the bandwidth of a transducer. The lateral resolution can be improved by increasing the central frequency and/or the aperture size of a transducer. The lateral resolution (δ_x) and the axial resolution (δ_z) are calculated through the following equations:

$$\delta_x \approx \lambda f_\# = \frac{c}{f_0} \times \frac{z_f}{D}, \tag{1.8}$$

$$\delta_z = \frac{c}{2 \times BW_{-6dB}}, \tag{1.9}$$

where λ is the wavelength defined as the ratio of the speed of sound (c) and the central frequency (f_0) of the transducer utilized. $f_\#$ is the f-number defined as the ratio of focal depth (z_f) to aperture size (D). BW_{-6dB} represents a -6 dB bandwidth of the transfer function of the transducer.

1.1.3 Elasticity Imaging

In clinical breast and prostate exams, physicians use palpation to detect abnormally hard regions in the tissue. Infiltrating ductal carcinomas are much stiffer than any other breast tissues, and prostate cancer is also stiffer than normal prostate tissues [3, 8, 10, 22]. In general, changes in tissue stiffness are correlated to pathological changes [23]. Over the last two decades, ultrasound elasticity imaging techniques have been developed to noninvasively estimate the tissue elastic properties [24-30].

Ultrasound elasticity imaging can be categorized into two groups based on tissue excitation techniques: quasi-static elasticity imaging and dynamic elasticity imaging. Quasi-static elasticity imaging also called elastography uses quasi-static compression to estimate tissue strain [26, 30]. Since stiff tissues have less strain than soft tissues, tissue stiffness information can be obtained by elastography. The estimated strain is usually displayed, and thus this approach is also referred as strain imaging.

Dynamic elasticity imaging uses dynamic excitations such as low frequency vibration (< 1 kHz) or acoustic radiation force [24, 25, 28]. The technique using low frequency vibration is called sonoelasticity imaging while the one using acoustic radiation force is called acoustic radiation force impulse (ARFI) imaging. This dissertation focuses on quasi-static elasticity imaging, and therefore the term of 'elasticity imaging' in this dissertation means only elastography.

Ultrasound elasticity imaging algorithms consist of two main components: displacement estimation and strain estimation. The displacement estimation can be divided into two parts: integer level and sub-pixel level estimations. The block diagram of elasticity imaging is presented in Figure 1.5.

For the displacement estimation, block matching algorithms are widely utilized. There are several approaches for block matching: normalized cross-correlation (NCC), sum of absolute differences (SAD) and sum of squared differences (SSD) [31, 32]. The magnitude of each function is used to obtain an integer level estimate of the displacement. For the sub-pixel displacement estimation, many approaches have already been developed [33-39]. The most straightforward approach to achieve sub-pixel precision is to interpolate the sampled signal and then to estimate displacements in terms of interpolated integer pixels [34]. In this case, however, computational costs are significantly increased by the interpolation factor and sub-pixel precision may not be enough. A spline-based algorithm can be used to solve these problems but the method is still computationally expensive [38]. Another approach to estimate sub-pixel displacements is to interpolate block matching functions [33, 35, 37, 40]. Using the linear phase property of the NCC function, the best block matching position between two radiofrequency (RF) signals with sub-pixel precision can be obtained. However, to utilize phase information, the complex NCC function must be computed, and therefore, computational costs increase compared to curve-fit methods of block matching functions such as either parabola or cosine fit with either NCC, SSD, or SAD. In these methods, bias error degrades displacement SNR. Furthermore, for lateral displacement estimation, interpolating sparsely sampled lateral data was suggested to improve displacement SNR, and synthetic lateral phase was introduced to utilize the phase zero-crossing method in the lateral direction as well.

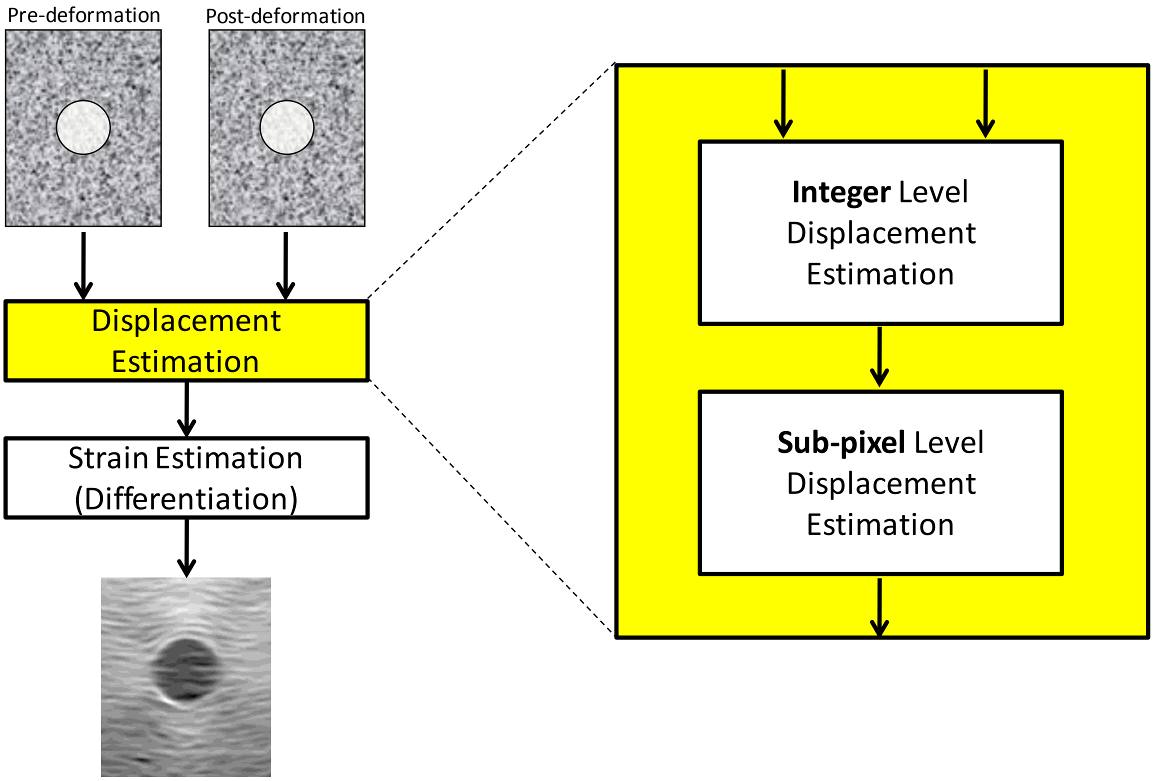

Figure 1.5: Block diagram of ultrasound elasticity imaging

1.1.4 Ultrasound-based Thermal Imaging

Ultrasound imaging has been shown to measure temperature change of less than 1°C at a spatial resolution similar to diagnostic ultrasound [2, 7, 12]. Using a real-time ultrasound imaging system, the temperature change can be estimated by monitoring the thermally induced speckle motion. The time of echo for ultrasound in a homogenous and uniformly heated medium is given by

$$t(T_0) = \frac{2z}{c(T_0)}, \tag{1.10}$$

where $t(T_0)$ is the time delay of echo from scatterer at position z at initial temperature T_0, and $c(T_0)$ is the speed of sound in the medium at initial temperature T_0. Since the speed of sound in tissue is dependent on temperature, apparent time shifts in ultrasound signal will be occurred when the temperature changes.

1.2 PHOTOACOUSTIC IIMAGING

Photoacoustic imaging (also called optoacoustic and, generally, thermoacoustic imaging) relies on the optical absorption as the contrast of the imaging modality. A nanosecond pulsed laser is used to initiate the photoacoustic phenomenon. The pulsed laser is absorbed by optical absorbers in the tissue. The absorbed light energy is converted into thermal energy that causes thermo-elastic expansion of the absorber. As a result, photoacoustic signal is detected by an ultrasound transducer and used to generate the image of tissue optical absorption distribution [41-43].

The block diagram of the photoacoustic imaging system is shown in Figure 1.6. Many parts of the photoacoustic imaging system are shared with an ultrasound imaging system. Therefore, it is relatively easy to combine two imaging modalities (ultrasound and photoacoustic) in one system to take advantages from both.

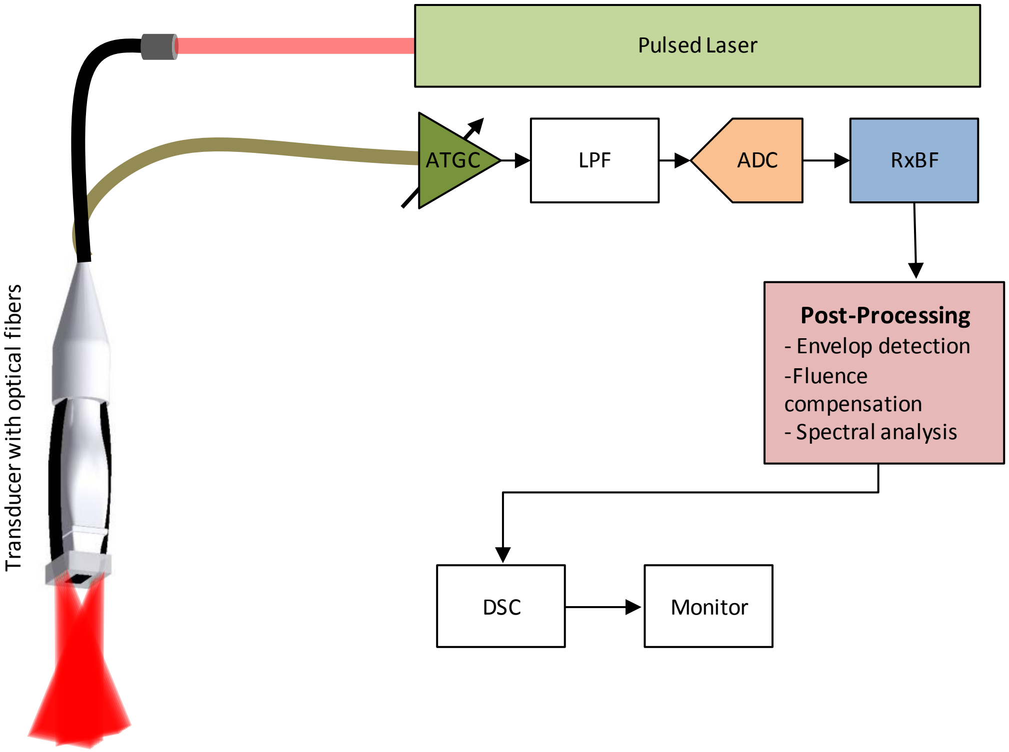

Figure 1.6: Block diagram of photoacoustic imaging system

1.2.1 Fundamentals of Photoacoustics

To generate photoacoustic signals efficiently, both thermal and stress confinement conditions should be satisfied. The thermal confinement is about the laser pulse duration as compared with the thermal diffusion time while the stress confinement is about the laser pulse duration as compared with the propagation time of the acoustic pulse. The thermal confinement condition is satisfied when the laser pulse duration is much shorter than the thermal diffusion time. In this case, all the energy will be confined inside the optically affected area. Moreover, if the laser pulse duration is much shorter than the acoustic wave propagation time through the absorber (i.e., under the stress confinement condition), the input energy is used with maximum efficiency to generate photoacoustic pressure. Typically, 3 to 10 ns pulsed lasers are utilized for photoacoustic imaging. The following equations show thermal (Equation 1.11) and stress (Equation 1.12) confinement conditions:

$$\tau_0 << d_c^2 \frac{\rho C_p}{\chi}, \tag{1.11}$$

$$\tau_0 << \frac{d_c}{c}, \tag{1.12}$$

where τ_0 is the laser pulse duration [s], d_c is the characteristic dimension of the heated region [m], ρ is the mass density [kg/m^3], C_p is the specific heat capacity at constant pressure [J/(kg K)], χ is the thermal conductivity [W/(m K)], and c is the speed of sound [m/s].

If both stress and thermal confinements are satisfied, the photoacoustic maximum pressure, p_0, at the pressure source can be expressed by:

$$p_0 = \Gamma \mu_a F, \tag{1.13}$$

$$\Gamma = \frac{\beta c^2}{C_p}, \tag{1.14}$$

where Γ is the Grüneisen coefficient [dimensionless], μ_a is the optical absorption coefficient [m^{-1}], F is the laser fluence [J/m^2], β is the volume expansion coefficient [K^{-1}], c is the speed of sound [m/s], and C_p is the heat capacity at constant pressure [J/(kg K)] [41, 43, 44].

The contrast of photoacoustic imaging mainly relies on optical absorption coefficients of the tissue. Since biological tissues have unique absorption spectra per each tissue component as shown in Figure 1.7, photoacoustic imaging can provide the information of tissue compositions.

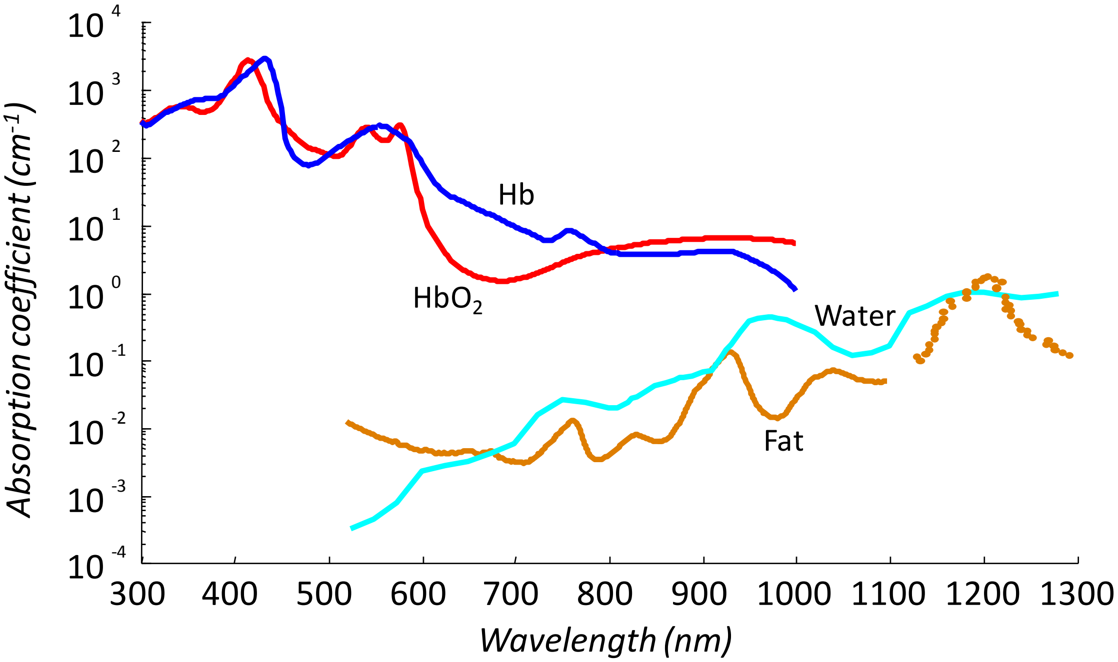

Figure 1.7: Optical absorption of tissue (Adapted from [45])

1.2.2 Nanoparticles

Because of several orders of magnitude higher optical absorption properties of metals than one of biological tissues, metallic particles are one of strong candidates for the photoacoustic imaging contrast agent. Especially, when the size of particles is in nanometer range, cellular and molecular level interactions with particles are anticipated. The gold nanoparticles can be used for photoacoustic contrast agents not only because of high optical absorption properties, but also because of superior biocompatibility [46], and capability of molecular specific targeting of cells. Another advantage of using nanoparticles is the ability to design the particles with the desired optical absorption spectrum by changing its shape as shown in Figure 1.8.

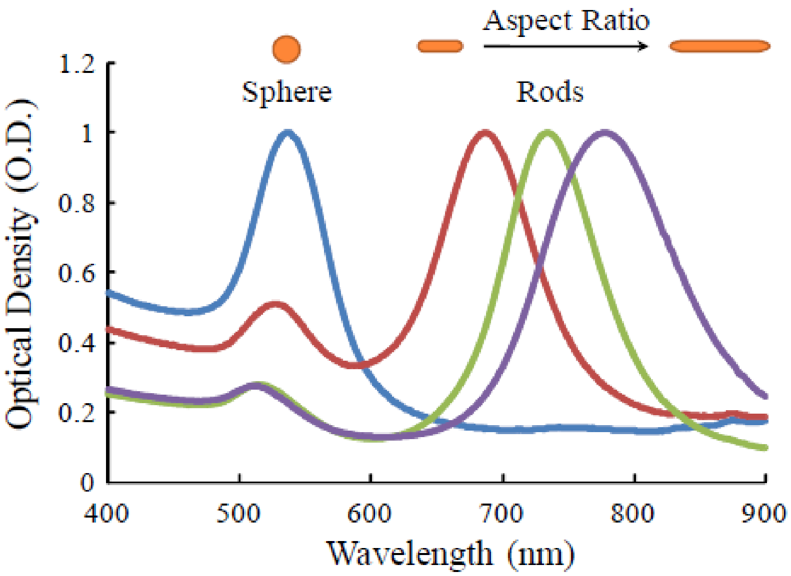

Figure 1.8: Optical absorption spectra of gold nanoparticles with different shapes (Adapted from [47])

1.2.3 Spectroscopic Photoacoustic Imaging

Spectroscopic photoacoustic imaging utilizes optical absorption spectra of absorbers in the tissue. By using this imaging technique, the distributions of nanoparticles as well as tissue compositions can be imaged.

There are two major optical absorbers inside the tissue within the near-infrared (NIR) window: *oxyhemoglobin* and *deoxyhemoglobin*. In addition to those, nanoparticles are also strong optical absorbers. The absorption coefficient of localized tissue can be defined by the sum of absorption coefficients for oxyhemoglobin (HbO_2), deoxyhemoglobin (Hb) and nanoparticle (NP) in the region. The absorption coefficient (μ_a) is the product of the molar absorption coefficient (ε) and the molar concentration (C) of the absorber. Therefore, the wavelength-dependent local absorption coefficient can be described as

$$\mu_a(\lambda) = C_{HbO_2}\varepsilon_{HbO_2}(\lambda) + C_{Hb}\varepsilon_{Hb}(\lambda) + C_{NP}\varepsilon_{NP}(\lambda), \tag{1.15}$$

where C_{HbO2}, C_{Hb} and C_{NP} are the molar concentrations [M], and ε_{HbO2}, ε_{Hb} and ε_{NP} are the molar absorption coefficients [$\text{cm}^{-1}\text{M}^{-1}$] of HbO_2, Hb and NP, respectively.

Linear least squares (LLS) method is widely utilized in this field to resolve the concentrations of multiple absorbers, and therefore distinguish tissue components. Moreover, the resolved HbO_2 and Hb concentrations can be used for estimating oxygen saturation in blood:

$$SO_2 = \frac{C_{HbO_2}}{C_{HbO_2} + C_{Hb}}. \tag{1.16}$$

When multiple wavelengths are considered, equation (1.15) can be expanded into vector forms:

$$\begin{bmatrix} \mu_a(\lambda_1) \\ \mu_a(\lambda_2) \\ \\ \mu_a(\lambda_N) \end{bmatrix} = \begin{bmatrix} \varepsilon_{HbO_2}(\lambda_1) & \varepsilon_{Hb}(\lambda_1) & \varepsilon_{NP}(\lambda_1) \\ \varepsilon_{HbO_2}(\lambda_2) & \varepsilon_{Hb}(\lambda_2) & \varepsilon_{NP}(\lambda_2) \\ \\ \varepsilon_{HbO_2}(\lambda_N) & \varepsilon_{Hb}(\lambda_N) & \varepsilon_{NP}(\lambda_N) \end{bmatrix} \begin{bmatrix} C_{HbO_2} \\ C_{Hb} \\ C_{NP} \end{bmatrix}, \tag{1.17}$$

Since the photoacoustic signal intensity is proportional to optical absorption coefficient under the assumption of the same laser fluence at different wavelengths, the following equation can be obtained:

$$\mathbf{P} = \mathbf{EC}, \tag{1.18}$$

where **P** are the multi-wavelength photoacoustic intensities in a column vector, **E** is the molar extinction coefficient matrix and **C** is the concentration values of HbO_2, Hb and NP in a column vector.

By using the LLS method, the concentration vector, **C**, can be obtained:

$$\mathbf{C} = \mathbf{E}^T(\mathbf{EE}^T)^{-1}\mathbf{P}, \tag{1.19}$$

where $\mathbf{E}^T(\mathbf{EE}^T)^{-1}$ is the pseudo-inverse matrix of the **E**.

1.2.4 Photoacoustic-based Thermal Imaging

Photoacoustic imaging can also be utilized for monitoring the temperature distribution in tissues noninvasively. Photoacoustic signal intensity is directly dependent on the dimensionless Grüneisen coefficient. The volume expansion coefficient and the speed of sound are both temperature dependent and linearly proportional to the temperature for water-based and fatty tissues between 10 and 55°C [48-50]. Therefore, the photoacoustic signal can be used to estimate tissue temperature [5, 13]. The temperature rise can be estimated by

$$\Delta T = a\frac{\Delta P}{P} = a\frac{\Delta \Gamma}{\Gamma}, \tag{1.20}$$

where a is the tissue-dependent constant that can be experimentally determined, ΔP is the pressure rise when the temperature rises by ΔT, and $\Delta \Gamma$ is the corresponding change in the Grüneisen coefficient.

The volume expansion coefficient of water changes from $0.2\cdot10^{-3}$ to $0.3\cdot10^{-3}(\mathrm{K})^{-1}$, while the speed of sound varies from 1481 to 1507 m/s when the temperature increases from 20 to 30°C [49, 50]. Therefore, about 51% increase in photoacoustic signal intensity, for water, will be occurred when the temperature increases by 10°C. The change in the speed of sound is 1.83 m/(°C·s) for bovine liver, and -7.4 m/(°C·s) for bovine fat [48], compared to 2.6 m/(°C·s) for water. Furthermore, the volume expansion coefficient of water-based tissues is in the range of $0.26\cdot10^{-3}$ to $0.37\cdot10^{-3}(\mathrm{K})^{-1}$, while lipid-based tissues have the volume expansion coefficient in the range of $-0.87\cdot10^{-3}(\mathrm{K})^{-1}$ to $-1.76\cdot10^{-3}(\mathrm{K})^{-1}$ [49]. The opposite signs of the speed of sound and the thermal expansion coefficient will lead to a positive and negative change in the photoacoustic signal.

1.3 PHOTOTHERMAL THERAPY

Photothermal therapy is one of the cancer treatment methods which can be noninvasive and tumor specific. It can be more effective if nanoparticles are used. Metal nanoparticles such as gold/silver nanospheres, nanorods, and nanoshells have highly absorbing optical properties compared to surrounding biological tissues, and it is possible to design the optical absorption peak of those nanoparticles. In pre-clinical investigations of photothermal therapy, temperature increases of greater than 30°C were produced using near infrared laser light tuned to matching nanoparticles causing irreversible tumor damage [51-54] . The temperature change during photothermal therapy is governed by two processes: heat generation by laser excitation and spatial redistribution due to combined effects of heat diffusion and blood perfusion. The following model can be used to describe both processes based on the bio-heat transfer equation:

$$\rho c \frac{\partial T}{\partial t} = \nabla(\lambda \nabla T) + Q_s + Q_p, \tag{1.21}$$

where T is the temperature [K], ρ is the tissue density [kg/m^3], c is the specific heat [J/kg/K], λ is the thermal conductivity of the tissue [W/m/K], Q_s is the external heat term [W/m^3], and Q_p is the heat removal due to perfusion [W/m^3]. The external heat term in photothermal therapy can be described by:

$$Q_s = W \mu_a, \tag{1.22}$$

where W is the laser fluence rate [W/m^2], and μ_a is the tissue optical absorption coefficient [1/m]. Therefore, the effective temperature rise is dependent on the laser irradiation and the optical properties of the tissue.

1.4 ORGANIZATION OF THE DISSERTATION

The aim of the research described in this dissertation is to develop and improve ultrasound and photoacoustic imaging methods especially for cancer detection and photothermal cancer therapy. To achieve the goal of the study, 4 specific parts of ultrasound and photoacoustic imaging techniques are focused on: ultrasound beamforming, ultrasound elasticity imaging, spectroscopic photoacoustic imaging, and ultrasound and photoacoustic thermal imaging.

Ultrasound elasticity imaging can be used for cancer detection. Once cancer is diagnosed, photothermal therapy can be performed to treat cancer. For the enhanced therapeutic outcomes, spectroscopic photoacoustic imaging can be utilized to ensure nanoparticle deposition at the tumor before therapy. During therapy, temperature monitoring is required to optimize therapeutic outcomes (i.e., maximize cancer tissue damage and minimize normal tissue damage). Ultrasound beamforming can affect all the imaging outcomes because it determines image qualities.

The research work is documented and organized into three sections: ultrasound image reconstruction, cancer detection using ultrasound elasticity imaging, and photothermal cancer theray guided by ultrasound and photoacoustic imaging.

Section 1 describes the improved ultrasound image reconstruction method. Specifically, beamforming method for intravascular ultrasound (IVUS) imaging is developed (Chapter 2). The results of this study were presented at the 31st Annual International Conference of the IEEE Engineering in Medicine and Biology Society: S. Kim, S.R. Aglyamov, S.Y. Emelianov, “Display pixel-based synthetic aperture focusing method for intravascular ultrasound imaging”, *Proceedings of the 2009 IEEE EMBS Conference*, pp. 4106-4109 (2009).

Section 2 describes ultrasound elasticity imaging for cancer detection. Firstly, the improved elasticity imaging algorithm is developed (Chapter 3). The results of this study were published in the journal: S. Kim, S.R. Aglyamov, S. Park, M. O’Donnell, S.Y. Emelianov, “An autocorrelation-based method for improvement of sub-pixel displacement estimation in ultrasound strain imaging," *IEEE Transactions on Ultrasonics, Ferrorelectrics and Frequency Control*, Vol. 58, No. 4, pp. 838-843 (2011). Some parts of this study were also presented at the International Conference on Ultrasonic Measurement and Imaging of Tissue Elasticity: S. Kim, S. Park, S.R. Aglyamov, M. O'Donnell, and S.Y. Emelianov, "Improvement of displacement estimation using autocorrelation," *Proceedings of the 7th International Conference on the Ultrasonic Measurement and Imaging of Tissue Elasticity*, pp. 58 (2008) and S. Kim, S. Park, S.R. Aglyamov, S. Claffey, W.G. Scott, and S.Y. Emelianov, "FPGA-based real-time ultrasound elasticity imaging system," *Proceedings of the 7th International Conference on the Ultrasonic Measurement and Imaging of Tissue Elasticity*, pp. 111 (2008). Secondly, prostate cancer detection using the developed ultrasound elasticity imaging method is evaluated (Chapter 4). The partial results of this study were presented at the Central Texas Clinical Research Forum: S. Kim, S.R. Aglyamov, J. Davis, S.Y. Emelianov, "Prostate cancer detection using ultrasound elasticity imaging," *Abstract and Poster presentation at the Central Texas Clinical Research Forum* (2009).

Section 3 describes ultrasound and photoacoustic image-guided photothermal therapy. Firstly, the improved spectroscopic photoacoustic imaging method for monitoring nanoparticle delivery is developed (Chapter 5). The results of this study were published in the journal: S. Kim, Y.-S. Chen, G.P. Luke, S. Emelianov, "*In vivo* three-dimensional spectroscopic photoacoustic imaging for monitoring nanoparticle delivery," *Biomedical Optics Express*, Vol. 2, No. 9, pp. 2540-2550 (2011). Secondly, ultrasound and photoacoustic image-guided photothermal cancer therapy is demonstrated (Chapter 6). The results of this study were presented at the 2010 IEEE International Ultrasonics Symposium: S. Kim, Y.-S. Chen, G.P. Luke, M. Mehrmohammadi, J.R. Cook, S.Y. Emelianov, "Ultrasound and photoacoustic image-guided photothermal therapy using silica-coated gold nanorods: *in-vivo* study," *Proceedings of the 2010 IEEE International Ultrasonics Symposium*, pp. 223-236 (2010).

Finally, the results of this work, discussions about ultrasound and photoacoustic imaging techniques, future directions of this research, and conclusions are addressed.

REFERENCES

[1] American Cancer Society, "Cancer Facts & Figures 2011," 2011.

[2] R. M. Arthur, W. L. Straube, J. W. Trobaugh, and E. G. Moros, "Non-invasive estimation of hyperthermia temperatures with ultrasound," *Int J Hyperthermia*, vol. 21, pp. 589-600, 2005.

[3] B. S. Garra, E. I. Cespedes, J. Ophir, S. R. Spratt, R. A. Zuurbier, C. M. Magnant, and M. F. Pennanen, "Elastography of breast lesions: initial clinical results," *Radiology*, vol. 202, pp. 79-86, 1997.

[4] B.Y. Karlan, "Ovarian cancer screening. The role of ultrasound in early detection," *Cancer*, vol. 76, pp. 2011-2015, 1995.

[5] I.V. Larina, "Real-time optoacoustic monitoring of temperature in tissues," *Applied Physics*, vol. 38, pp. 2633-2639, 2005.

[6] R. Marco, "Role of prostate fossa ultrasonography in the diagnosis of local recurrence after radical prostatectomy in case of PSA failure," *Associazione ricerche in urologia*, vol. 74, pp. 304-308, 2002.

[7] N. R. Miller, J. C. Bamber, and G. R. ter Haar, "Imaging of temperature-induced echo strain: preliminary in vitro study to assess feasibility for guiding focused ultrasound surgery," *Ultrasound Med Biol*, vol. 30, pp. 345-56, 2004.

[8] T. Miyagawa, M. Tsutsumi, T. Matsumura, N. Kawazoe, S. Ishikawa, T. Shimokama, N. Miyanaga, and H. Akaza, "Real-time elastography for the diagnosis of prostate cancer: evaluation of elastographic moving images," *Jpn J Clin Oncol*, vol. 39, pp. 394-8, 2009.

[9] N. Miyanaga, H. Akaza, M. Yamakawa, T. Oikawa, N. Sekido, S. Hinotsu, K. Kawai, T. Shimazui, and T. Shiina, "Tissue elasticity imaging for diagnosis of prostate cancer: a preliminary report," *Int J Urol*, vol. 13, pp. 1514-8, 2006.

[10] L. Pallwein, M. Mitterberger, P. Struve, G. Pinggera, W. Horninger, G. Bartsch, F. Aigner, A. Lorenz, F. Pedross, and F. Frauscher, "Real-time elastography for

detecting prostate cancer: preliminary experience," *BJU Int*, vol. 100, pp. 42-6, 2007.

[11] R. Seip, "Noninvasive estimation of tissue temperature response to heating fields using diagnostic ultrasound," *IEEE Trans Biomedical Engineering*, vol. 42, pp. 828-839, 1995.

[12] J. Shah, S. R. Aglyamov, K. Sokolov, T. E. Milner, and S. Y. Emelianov, "Ultrasound imaging to monitor photothermal therapy - feasibility study," *Opt Express*, vol. 16, pp. 3776-85, 2008.

[13] J. Shah, S. Park, S. Aglyamov, T. Larson, L. Ma, K. Sokolov, K. Johnston, T. Milner, and S. Y. Emelianov, "Photoacoustic imaging and temperature measurement for photothermal cancer therapy," *J Biomed Opt*, vol. 13, pp. 034024, 2008.

[14] W. Teh, "The role of ultrasound in breast cancer screening. A consensus statement by the european group for breast cancer screening," *European Journal of Cancer*, vol. 34, pp. 449-450, 1998.

[15] T. Varghese, J. A. Zagzebski, Q. Chen, U. Techavipoo, G. Frank, C. Johnson, A. Wright, and F. T. Lee, Jr., "Ultrasound monitoring of temperature change during radiofrequency ablation: preliminary in-vivo results," *Ultrasound Med Biol*, vol. 28, pp. 321-9, 2002.

[16] Q. L. Zhu, Y. X. Jiang, J. B. Liu, H. Liu, Q. Sun, Q. Dai, and X. Chen, "Real-time ultrasound elastography: its potential role in assessment of breast lesions," *Ultrasound Med Biol*, vol. 34, pp. 1232-8, 2008.

[17] D. A. Christensen, *Ultrasonic bioinstrumentation*. New York:: Wiley, 1988.

[18] R. Mucci, B. Beranek, I. Newman, and M. A. Cambridge, "A comparison of efficient beamforming algorithms," *IEEE Transactions on Acoustics, Speech and Signal Processing*, vol. 32, pp. 548-558, 1984.

[19] J. H. Chang, J. T. Yen, and K. K. Shung, "High-speed digital scan converter for high-frequency ultrasound sector scanners," *Ultrasonics*, vol. 48, pp. 444-52, 2008.

[20] J. A. Jensen, *Imaging of Complex Media with coustic and Seismic Waves: Ultrasound imaging and its modeling*: Springer Verlag, 2002.

[21] "http://en.wikipedia.org/wiki/Ultrasonic_sensor."

[22] M. M. Doyley, J. C. Bamber, F. Fuechsel, and N. L. Bush, "A freehand elastographic imaging approach for clinical breast imaging: system development and performance evaluation," *Ultrasound Med Biol,* vol. 27, pp. 1347-57, 2001.

[23] Y.C Fung, *Biomechanics: Mechanical properties of living tissues*. New York: Springer-Verlag, 1981.

[24] R. M. Lerner, S. R. Huang, and K. J. Parker, ""Sonoelasticity" images derived from ultrasound signals in mechanically vibrated tissues," *Ultrasound Med Biol*, vol. 16, pp. 231-9, 1990.

[25] Y. Yamakoshi, J. Sato, and T. Sato, "Ultrasonic imaging of internal vibration of soft tissue under forced vibration," *IEEE Trans Ultrason Ferroelectr Freq Control*, vol. 37, pp. 45-53, 1990.

[26] J. Ophir, I. Cespedes, H. Ponnekanti, Y. Yazdi, and X. Li, "Elastography: a quantitative method for imaging the elasticity of biological tissues," *Ultrason Imaging*, vol. 13, pp. 111-34, 1991.

[27] A. P. Sarvazyan, O. V. Rudenko, S. D. Swanson, J. B. Fowlkes, and S. Y. Emelianov, "Shear wave elasticity imaging: a new ultrasonic technology of medical diagnostics," *Ultrasound Med Biol*, vol. 24, pp. 1419-35, 1998.

[28] K. R. Nightingale, M. L. Palmeri, R. W. Nightingale, and G. E. Trahey, "On the feasibility of remote palpation using acoustic radiation force," *J Acoust Soc Am*, vol. 110, pp. 625-34, 2001.

[29] R. Q. Erkamp, S. Y. Emelianov, A. R. Skovoroda, and M. O'Donnell, "Nonlinear elasticity imaging: theory and phantom study," *IEEE Trans Ultrason Ferroelectr Freq Control*, vol. 51, pp. 532-9, 2004.

[30] M. O'Donell, A. R. Skovoroda, B. M. Shapo, and S. Y. Emelianov, "Internal displacement and strain imaging using ultrasonic speckle tracking," *IEEE Trans Ultrason Ferroelectr Freq Control*, vol. 41, pp. 314-325, 1994.

[31] J. Ophir, S. K. Alam, B. Garra, F. Kallel, E. Konofagou, T. Krouskop, and T. Varghese, "Elastography: ultrasonic estimation and imaging of the elastic properties of tissues," *Proc Inst Mech Eng H*, vol. 213, pp. 203-33, 1999.

[32] J. Jiang and T. J. Hall, "A parallelizable real-time motion tracking algorithm with applications to ultrasonic strain imaging," *Phys Med Biol*, vol. 52, pp. 3773-90, 2007.

[33] I. Cespedes, Y. Huang, J. Ophir, and S. Spratt, "Methods for estimation of subsample time delays of digitized echo signals," *Ultrason Imaging*, vol. 17, pp. 142-71, 1995.

[34] E. Konofagou and J. Ophir, "A new elastographic method for estimation and imaging of lateral displacements, lateral strains, corrected axial strains and Poisson's ratios in tissues," *Ultrasound Med Biol*, vol. 24, pp. 1183-99, 1998.

[35] M. A. Lubinski, S. Y. Emelianov, and M. O'Donnell, "Speckle tracking methods for ultrasonic elasticity imaging using short-time correlation," *IEEE Trans Ultrason Ferroelectr Freq Control*, vol. 46, pp. 82-96, 1999.

[36] M. A. Lubinski, S. Y. Emelianov, and M. O'Donnell, "Adaptive strain estimation using retrospective processing [medical US elasticity imaging]," *IEEE Trans Ultrason Ferroelectr Freq Control*, vol. 46, pp. 97-107, 1999.

[37] A. Pesavento, C. Perrey, M. Krueger, and H. Ermert, "A time-efficient and accurate strain estimation concept for ultrasonic elastography using iterative phase zero estimation," *IEEE Trans Ultrason Ferroelectr Freq Control*, vol. 46, pp. 1057-67, 1999.

[38] F. Viola and W. F. Walker, "A spline-based algorithm for continuous time-delay estimation using sampled data," *IEEE Trans Ultrason Ferroelectr Freq Control*, vol. 52, pp. 80-93, 2005.

[39] R. Zahiri-Azar and S. E. Salcudean, "Motion estimation in ultrasound images using time domain cross correlation with prior estimates," *IEEE Trans Biomed Eng*, vol. 53, pp. 1990-2000, 2006.

[40] X. Chen, M. J. Zohdy, S. Y. Emelianov, and M. O'Donell, "Lateral speckle tracking using synthetic lateral phase," *IEEE Trans Ultrason Ferroelectr Freq Control*, vol. 51, pp. 540-50, 2004.

[41] A.A. Oraevsky and A.A. Karabutov, *Optoacoustic tomography*, 2003.

[42] L.V. Wang, *Photoacoustic imaging and spectroscopy*, 2009.

[43] L. V. Wang and H. I. Wu, *Biomedical optics - Principles and imaging*: Wiley, 2007.

[44] C. Li and L. V. Wang, "Photoacoustic tomography and sensing in biomedicine," *Phys Med Biol*, vol. 54, pp. R59-97, 2009.

[45] S.A. Prahl, "Optical properties spectra compiled by Scott Prahl," *Available from:* *http://omlc.ogi.edu/spectra/*.

[46] R. Shukla, V. Bansal, M. Chaudhary, A. Basu, R. R. Bhonde, and M. Sastry, "Biocompatibility of gold nanoparticles and their endocytotic fate inside the cellular compartment: a microscopic overview," *Langmuir*, vol. 21, pp. 10644-54, 2005.

[47] S. Mallidi, B. Wang, M. Mehrmohammadi, M. Qu, Y.-S. Chen, P. Joshi, S. Kim, K.A. Homan, A.B. Karpiouk, R.W. Smalling, K. Sokolov, and S.Y. Emelianov, "Ultrasound-based imaging of nanoparticles: from molecular and cellular imaging to therapy guidance," *Proceedings of the 2009 IEEE Ultrasonics Symposium*, pp. 27-36 2009.

[48] J. C. Bamber and C. R. Hill, "Ultrasonic attenuation and propagation speed in mammalian tissues as a function of temperature," *Ultrasound Med Biol*, vol. 5, pp. 149-57, 1979.

[49] F.A. Duck, "Physical properties of tissue," *Academic*, 1990.

[50] I.K. Kikoin, *Handbook of chemistry and physics*, 54th ed: CRC Press, 1974.

[51] X. Huang, I. H. El-Sayed, W. Qian, and M. A. El-Sayed, "Cancer cell imaging and photothermal therapy in the near-infrared region by using gold nanorods," *J Am Chem Soc*, vol. 128, pp. 2115-20, 2006.

[52] L. R. Hirsch, R. J. Stafford, J. A. Bankson, S. R. Sershen, B. Rivera, R. E. Price, J. D. Hazle, N. J. Halas, and J. L. West, "Nanoshell-mediated near-infrared thermal therapy of tumors under magnetic resonance guidance," *Proc Natl Acad Sci U S A*, vol. 100, pp. 13549-54, 2003.

[53] C. Loo, A. Lin, L. Hirsch, M. H. Lee, J. Barton, N. Halas, J. West, and R. Drezek, "Nanoshell-enabled photonics-based imaging and therapy of cancer," *Technol Cancer Res Treat*, vol. 3, pp. 33-40, 2004.

[54] W. R. Chen, R. L. Adams, S. Heaton, D. T. Dickey, K. E. Bartels, and R. E. Nordquist, "Chromophore-enhanced laser-tumor tissue photothermal interaction using an 808-nm diode laser," *Cancer Lett*, vol. 88, pp. 15-9, 1995.

SECTION 1: *ULTRASOUND IMAGE RECONSTRUCTION*

In this section, the improved intravascular ultrasound (IVUS) image reconstruction algorithm was developed. Even though the scope of this section is not perfectly related to the cancer research, the same idea and concept is applicable to the general ultrasound imaging method. The enhanced ultrasound image quality is obviously beneficial to diagnose cancer.

Chapter 2: *Display Pixel-based Synthetic Aperture Focusing Method for Intravascular Ultrasound Imaging*

The results of this study have been published on *Proceedings of IEEE Engineering in Medicine and Biology Conference* in 2009.

ABSTRACT

An intravascular ultrasound image reconstruction technique that combines synthetic aperture focusing and display pixel-based focusing methods is presented. Although the synthetic aperture focusing method can improve intravascular ultrasound image quality, the final displayed images are usually blurry in the angular direction due to the limitations of the digital scan converter. The display pixel-based focusing method can eliminate blurring effects caused by the digital scan converter. Therefore, the image quality can be further improved by applying the display pixel-based focusing method to the synthetic aperture focusing method, especially for intravascular ultrasound images. The experimental studies were performed to evaluate display pixel-based synthetic aperture focusing method. The computational complexity of the display pixel-based synthetic aperture focusing method was discussed in comparison with that of the synthetic aperture focusing method.

2.1 INTRODUCTION

Intravascular ultrasound (IVUS) imaging, capable of direct assessment of morphological properties of coronary arteries, is widely used in clinics to diagnose coronary atherosclerotic disease [1-7]. However, the IVUS image quality is reduced, compared to conventional array-based ultrasound images, because of technical limitations of IVUS catheters and geometric problems of IVUS images.

In array-based intravascular catheter systems, size and power constraints permit only one element (or limited set of elements) to be activated at a time. Therefore, the synthetic aperture focusing (SAF) method was introduced to produce focused ultrasound beams in IVUS imaging [8]. As a result, the SAF method can enhance the angular resolution of IVUS images. The superposition of each element data, collected at a different time but considered with appropriate delays, allows two-way focused beams in IVUS imaging. However, since imaging points reconstructed using the SAF method are defined in polar coordinates (r, θ), the digital scan converter (DSC) is needed to display IVUS images on the screen in Cartesian coordinates (x, y). The DSC can cause blurring effects that degrade the angular resolution of final IVUS images. These blurring effects can be reduced by increasing the number of scan-lines within the frame. However, more efficient and cost effective methods are required to eliminate the distortion due to the DSC, especially for IVUS imaging.

Hwang and Song proposed the display pixel-based focusing (DPBF) method to solve DSC problems in conventional ultrasound imaging [9]. In this technique, ultrasound waves are directly focused at display pixels on the monitor. Therefore, the DSC was no longer required.

In this chapter, I applied the DPBF method to the SAF method for the purpose of improving the IVUS image quality. In order to efficiently implement the DPBF method in IVUS imaging, a phase rotation beamforming (PRB) method was used. Since only one element (or limited set of elements) can be activated at a time in array-based intravascular catheter systems, only one pair (or limited set of pairs) of demodulation circuits is required for the PRB method. Also, the PRB method uses complex baseband signals so it can directly generate envelope data on display pixels without any other post-processing. The phantom experiments were performed to evaluate the spatial resolution and contrast of IVUS images obtained by using display pixel-based synthetic aperture focusing (DPBSAF) method. To conclude, I discussed the computational complexity of the DPBSAF method.

2.2 INTRAVASCULAR ULTRASOUND IMAGE RECONSTRUCTION

2.2.1 Synthetic Aperture Focusing

A transmit-receive scheme for IVUS synthetic aperture imaging, using a 64-element array catheter and a 14-element effective aperture, was originally proposed by O’Donnell and Thomas [8]. By using a total of 896 (i.e., 64 × 14) different transmit-receive data sets, fully focused (i.e., two-way focused) ultrasound beams can be generated. Those beams are placed in polar coordinates (r, θ). Therefore, the DSC has to be performed to display IVUS images on the screen in Cartesian coordinates (x, y).

2.2.2 Digital Scan Converter

Bilinear interpolation is commonly used in the DSC [10]. Linear interpolation is consecutively performed in radial, then angular direction. The reconstructed pixel value, *P*, is pictorially shown in Figure 2.1, and can be calculated by

$$P = \frac{\alpha \times I_2 + \beta \times I_1}{\alpha + \beta}, \tag{2.1}$$

$$I_1 = \frac{d_2 \times s_1 + d_1 \times s_2}{d_1 + d_2}, \quad I_2 = \frac{d_2 \times s_3 + d_1 \times s_4}{d_1 + d_2}, \tag{2.2}$$

where α and β are angular differences between *P* and neighboring scan-lines, and d_1 and d_2 are radial differences between *P* and neighboring samples on scan-lines.

As shown in Figure 2.1, four neighboring data formats are used in order to estimate *P* value. This procedure can cause image distortions like blurring effects on converted images.

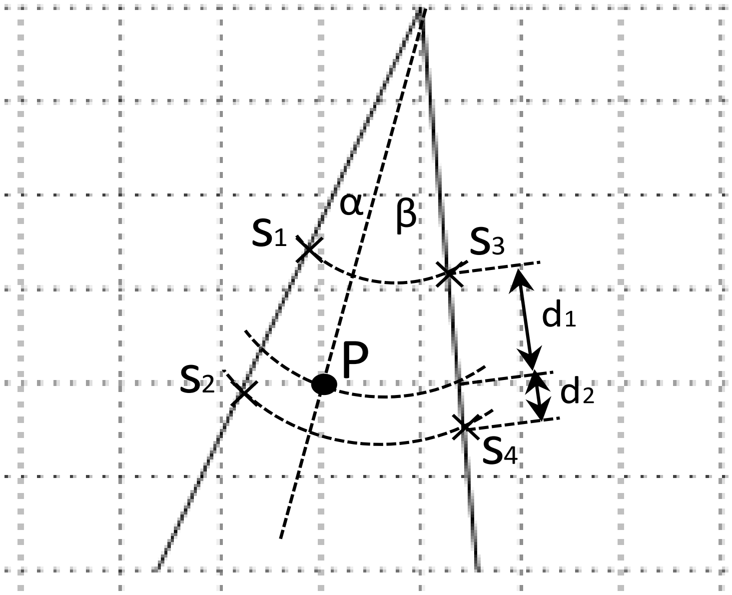

Figure 2.1: Graphical representation of bilinear interpolation in the DSC.

2.2.3 Display Pixel-based Focusing

In IVUS imaging, the performance of the DSC depends on the number of scan lines. If there are enough scan-lines per one frame, high quality of IVUS images can be displayed on the screen. However, non-uniform sampled data in Cartesian coordinates (x, y) are inefficient. While data are oversampled in the region close to the catheter, there are insufficient data points in the region far from the catheter as shown in Figure 2.2.

The display pixel-based focusing (DPBF) method, proposed by Hwang and Song [9], can solve the problem of mismatches, in IVUS images, between the focused data positions and the display pixel positions by directly focusing beams on display pixels. However, in this case, certain length of virtual scan-lines that crosses each display pixels are needed for the envelope value of the display pixel.

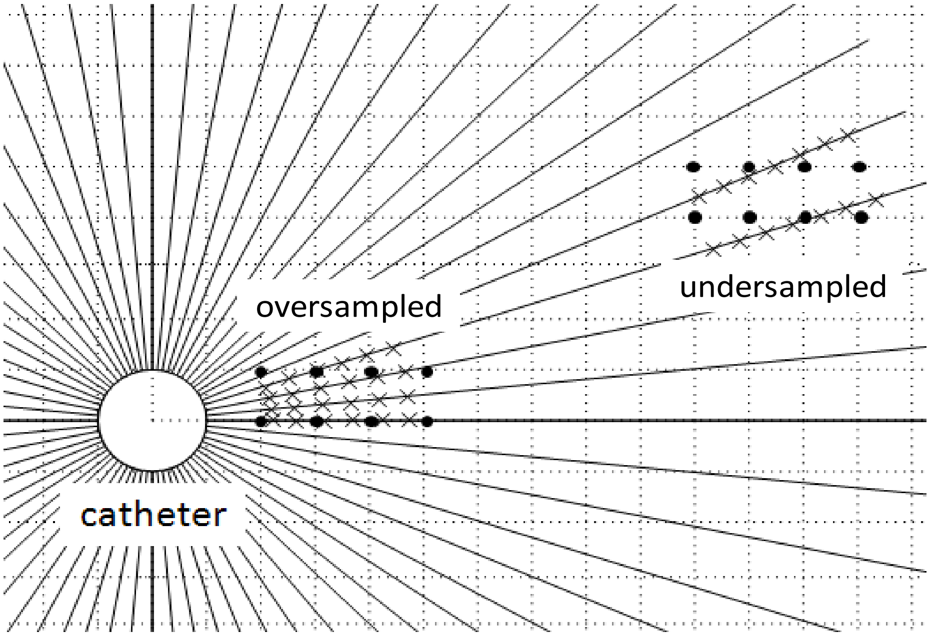

Figure 2.2: Illustration of IVUS image reconstruction. Crosses represent focused data on scan-lines. Circles represent display pixels on the screen.

2.2.4 Phase Rotation Beamforming

In order to avoid additional signal processing (i.e., envelope detection of focused beams) during the DPBF, a baseband beamforming method was used in this study. Phase rotation beamforming (PRB) method is one of the baseband beamforming techniques based on the frequency domain approach [11]. The applications of the PRB method are restricted to narrowband signals because only center frequency component can be correctly delayed and focused. However, the performance of the PRB method has been proven high enough for broadband applications because of low sensitivity of phase delay errors in ultrasound signals [12]. Since the PRB method is a baseband approach, envelope data on each display pixel can be directly acquired after the beamforming if the DPBF method is used.

In addition, the PRB method requires high hardware complexity in array-based systems, because each array element has to be connected to different demodulation circuits due to the simultaneous data collection using several elements. However, in the case of IVUS systems, only one element (or limited set of elements) can be activated at a time so the PRB method can be implemented using only one demodulation circuit (or limited set of demodulation circuits). Therefore, the PRB method for IVUS synthetic aperture imaging does not increase hardware complexity compared to other time domain approaches [11].

2.3 MATERIALS AND METHODS

To investigate the quality of IVUS images obtained using the display pixel-based synthetic aperture focusing (DPBSAF) method and conventional synthetic aperture focusing (SAF) method, experimental studies were performed. The first set of experiments was conducted using point targets to examine the blurring effects caused by the DSC. Three 250-µm diameter nylon strings, representing point targets, were placed at different distances from the catheter. The second set of experiments was performed using polyvinyl alcohol (PVA) phantom and a rabbit artery. The phantom was produced using 8% of PVA solution and 0.4% of 15-µm silica particles. The rabbit artery was used to verify that the DPBSAF method improves the IVUS image quality in real tissues.

In order to collect the single element transmit-receive data sets, an EagleEye, 20 MHz, array-based catheter (Volcano Corporation, CA, USA) was used. This 1.17-mm diameter catheter has 64 acoustic elements.

2.4 RESULTS AND DISCUSSION

2.4.1 Point Spread Function and Contrast-to-Noise Ratio

From the point target experiment, the point spread function (PSF) and contrast-to-noise ratio (CNR) were analyzed. To evaluate the spatial resolution of IUVS images, the PSF was analyzed. The CNR was calculated to quantitatively evaluate the blurring effects caused by the DSC. The CNR was obtained as follows.

$$CNR = 20 \cdot \log_{10}\left(\frac{2(\varepsilon_1 - \varepsilon_2)^2}{\sigma_{\varepsilon_1}^2 + \sigma_{\varepsilon_2}^2}\right), \tag{2.3}$$

where ε_1 and ε_2 represent the means, and $\sigma_{\varepsilon_1}^2$ and $\sigma_{\varepsilon_2}^2$ denote the signal variances within the region inside and outside the point target, respectively.

From images shown in Figure 2.3, the improvement of image quality is evident. Point targets in the image, obtained using the DPBSAF method, are sharper than those obtained only using the SAF method. As expected, the blurring effects were removed in the DPBSAF image. The PSF in Figure 2.4 shows that the increase in number of scan-lines from 64 to 256 beams for the SAF method causes narrower beam width. However, it is not as significant as the DPBSAF method. The CNRs of each image of point targets are 98.3 dB for the SAF method with 64 beams, 99.5 dB for the SAF method with 256 beams, and 100.3 dB for the DPBSAF method. Since the background noise of an IVUS image is usually caused by the blurring effects of the DSC, the DPBSAF method can decrease noise and increase the CNR. The improvement of IVUS images using the DPBSAF method, in terms of both spatial resolution and CNR, is clearly shown in the experimental results of the phantom and the rabbit artery (Figure 2.5 and Figure 2.6).

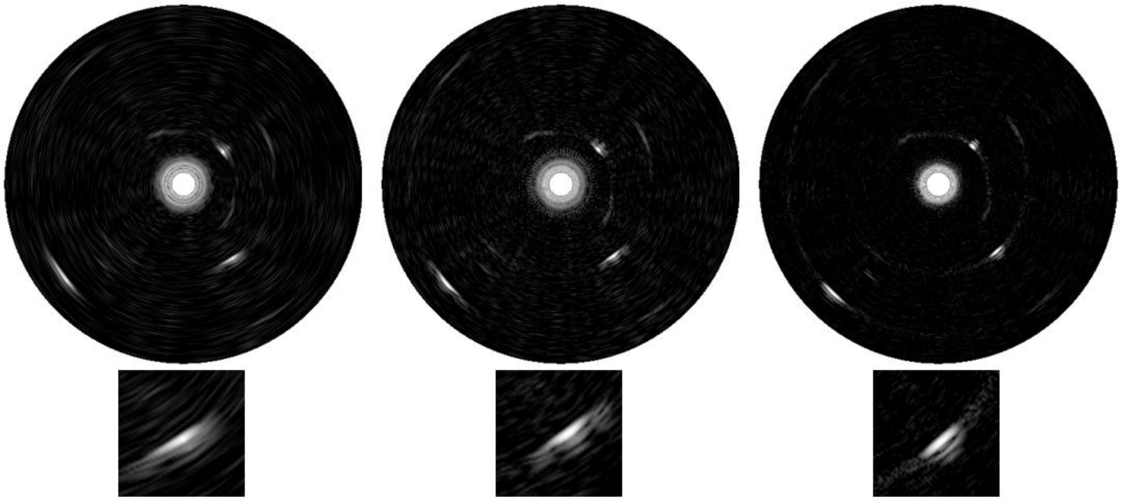

(a) (b) (c)

Figure 2.3: IVUS images of point targets obtained using the SAF method with (a) 64 beams and (b) 256 beams, then converted into 512 by 512 pixels, and (c) using the DPBSAF method with 512 by 512 pixels. The dynamic range of all images is 40 dB. The second row images are zoomed-in point targets positioned at 4.5-mm apart from the center of a catheter. Clearly, the image obtained using the DPBSAF method has better angular resolution compared to images obtained using the SAF method.

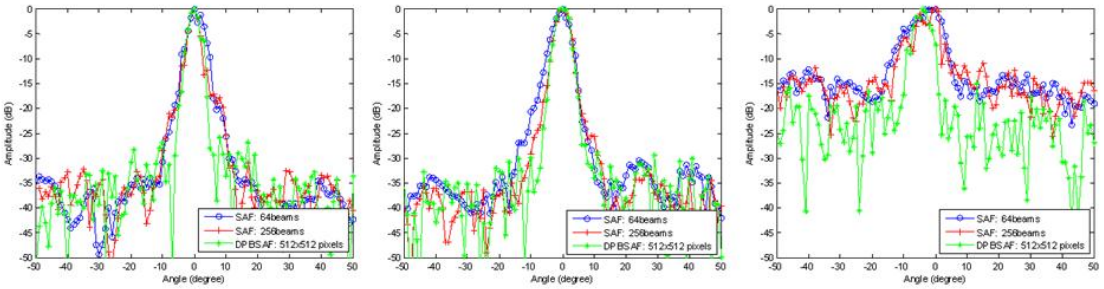

(a) (b) (c)

Figure 2.4: Angular profile of the point spread function at (a) 2.6, (b) 4.5, and (c) 7.9mm apart from the center of a catheter. In each graph, the DPBSAF method compares with the SAF method. At all positions, the DPBSAF method has better performance, especially for the farther position from the catheter.

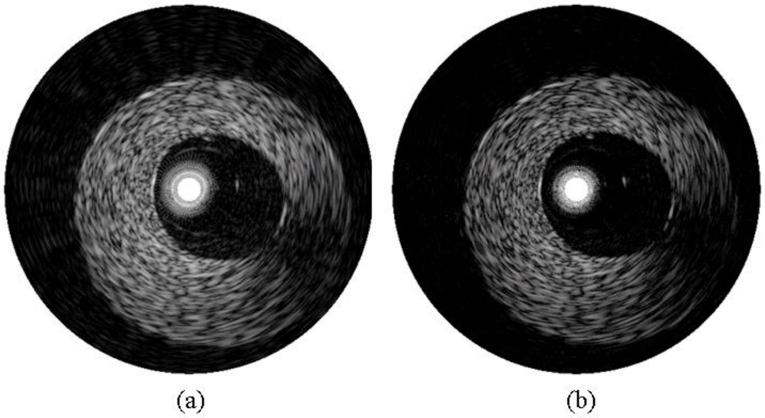
(a) (b)

Figure 2.5: PVA phantom images obtained using (a) the SAF method with 256 beams, and (b) the DPBSAF method with 300 by 300 pixels. All images are shown using 40 dB display dynamic range.

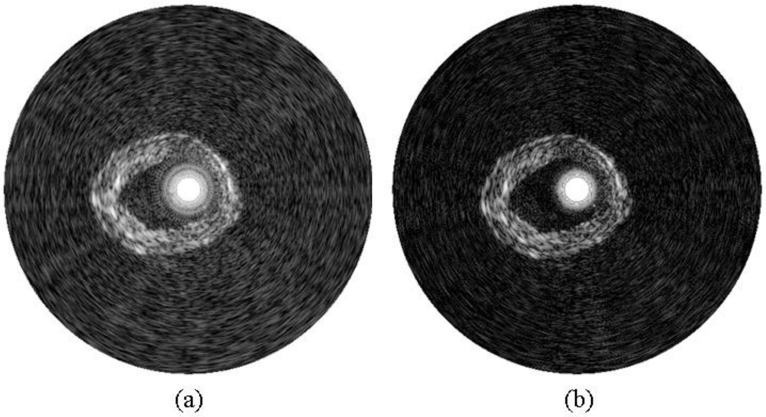
(a) (b)

Figure 2.6: Rabbit artery images obtained using (a) the SAF method with 256 beams, and (b) the DPBSAF method with 300 by 300 pixels. All images are shown using 40 dB display dynamic range.

2.4.2 Computational Complexity

The computational complexity of the DPBSAF method was compared with that of the SAF method by counting the number of multiplications per unit time (MPU). In the case of the DPBSAF method, only beamforming computational load was considered while the SAF method took account of not only beamforming but also DSC computational load. Imaging conditions are shown in Table 2.1.

Table 2.1: IVUS imaging conditions

Effective transmit channels	14
Effective receive channels	14
The number of beams	N
The number of samples per beam	256 (for 10mm)
Display pixels	n × n

To generate one focused beam, the SAF method requires 14 × 14 different data sets based on effective transmit and receive aperture sizes. The PRB method requires four multiplications to adjust delays for the channel data because of the complex value multiplication. Also, the DSC requires nine multiplications per one pixel. Based on all of those, computational complexity was compared between the SAF method and the DPBSAF method in Fig. 2.7. The DPBSAF method with 300 by 300 pixels is comparable to the SAF method with 256 beams in terms of computational complexity.

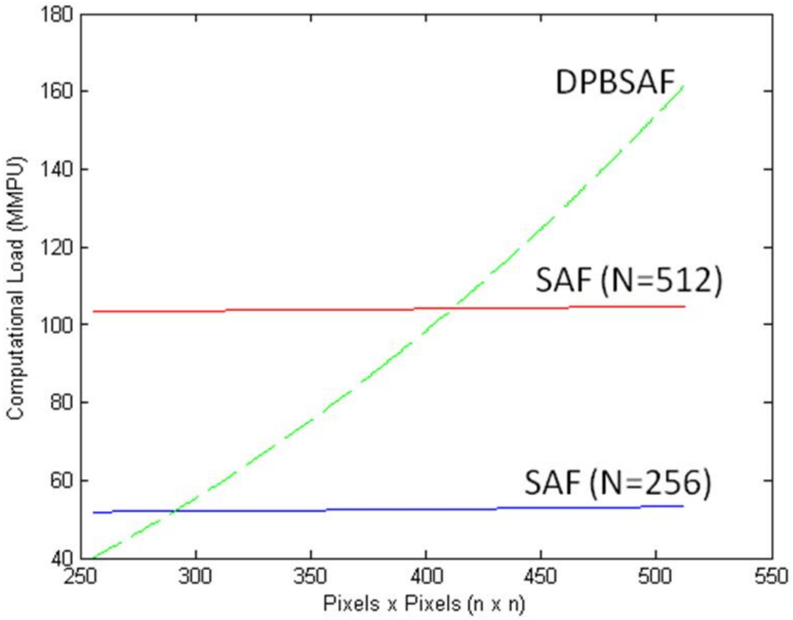

Figure 2.7: MPUs for the SAF with 256 and 512 beams, and the DPBSAF method.

2.5 CONCLUSION

In IVUS imaging, the SAF method has played an important role to increase the image quality. However, the DSC degraded IVUS images because of its geometrical problem. The combined method of the SAF and the DPBF methods further improves the IVUS image quality. In addition, the computational complexity of the DPBSAF method can be comparable to the SAF technique.

REFERENCES

[1] S. B. Feinstein, "Contrast ultrasound imaging of the carotid artery vasa vasorum and atherosclerotic plaque neovascularization," *J Am Coll Cardiol*, vol. 48, pp. 236-43, 2006.

[2] P. H. Davis, J. D. Dawson, W. A. Riley, and R. M. Lauer, "Carotid Intimal-Medial Thickness Is Related to Cardiovascular Risk Factors Measured From Childhood Through Middle Age: The Muscatine Study," *Circulation*, vol. 104, pp. 2815-2819, 2001.

[3] S. E. Nissen and P. Yock, "Intravascular ultrasound: novel pathophysiological insights and current clinical applications," *Circulation*, vol. 103, pp. 604-16, 2001.

[4] A. Nair, J. D. Klingensmith, and D. G. Vince, "Real-time plaque characterization and visualization with spectral analysis of intravascular ultrasound data," *Stud Health Technol Inform*, vol. 113, pp. 300-20, 2005.

[5] A. Nair, B. D. Kuban, E. M. Tuzcu, P. Schoenhagen, S. E. Nissen, and D. G. Vince, "Coronary plaque classification with intravascular ultrasound radiofrequency data analysis," *Circulation*, vol. 106, pp. 2200-6, 2002.

[6] A. Konig, M. P. Margolis, R. Virmani, D. Holmes, and V. Klauss, "Technology insight: in vivo coronary plaque classification by intravascular ultrasonography radiofrequency analysis," *Nat Clin Pract Cardiovasc Med*, vol. 5, pp. 219-29, 2008.

[7] A. Katouzian, S. Sathyanarayana, B. Baseri, E. E. Konofagou, and S. G. Carlier, "Challenges in atherosclerotic plaque characterization with intravascular ultrasound (IVUS): from data collection to classification," *IEEE Trans Inf Technol Biomed*, vol. 12, pp. 315-27, 2008.

[8] M. O'Donnell and L. J. Thomas, "Efficient synthetic aperture imaging from a circular aperture with possible application to catheter-based imaging," *IEEE Trans Ultrason Ferroelectr Freq Control*, vol. 39, pp. 366-80, 1992.

[9] J. S. Hwang and T. K. Song, "A study of the display pixel-based focusing method in ultrasound imaging," *Ultrason Imaging*, vol. 23, pp. 1-18, 2001.

[10] J. H. Chang, J. T. Yen, and K. K. Shung, "High-speed digital scan converter for high-frequency ultrasound sector scanners," *Ultrasonics*, vol. 48, pp. 444-52, 2008.

[11] R. Mucci, B. Beranek, I. Newman, and M. A. Cambridge, "A comparison of efficient beamforming algorithms," *IEEE Transactions on Acoustics, Speech and Signal Processing*, vol. 32, pp. 548-558, 1984.

[12] F. K. Schneider, Y. M. Yoo, A. Agarwal, L. M. Koh, and Y. Kim, "New demodulation filter in digital phase rotation beamforming," *Ultrasonics*, vol. 44, pp. 265-71, 2006.

SECTION 2: *CANCER DETECTION USING ULTRASOUND ELASTICITY IMAGING*

In this section the improved ultrasound elasticity imaging algorithm was developed, and the developed algorithm was used for prostate cancer detection. Chapter 3 presents the enhanced sub-pixel displacement estimation algorithm for ultrasound elasticity imaging. Then, chapter 4 presents clinical study on evaluating the feasibility of using ultrasound elasticity imaging for prostate cancer detection.

Chapter 3: *An Autocorrelation-based Method for Improvement of Sub-pixel Displacement Estimation in Ultrasound Elasticity Imaging*

The results of this study have been published on *IEEE Transactions on Ultrasonics, Ferroelectrics and Frequency Control* in 2011. Some parts of results have also been presented at *the International Conference on Ultrasonic Measurement and Imaging of Tissue Elasticity* in 2008.

ABSTRACT

In ultrasound strain and elasticity imaging, an accurate and cost-effective sub-pixel displacement estimator is required because strain/elasticity imaging quality relies on the displacement SNR, which can often be higher if more computational resources are provided. In this paper, I introduce an autocorrelation-based method to cost-effectively improve sub-pixel displacement estimation quality. To quantitatively evaluate the performance of the autocorrelation method, simulated and tissue-mimicking phantom experiments were performed. The computational cost of the autocorrelation method is also discussed. The results of this study suggest the autocorrelation method can be used for a real-time elasticity imaging system.

3.1 INTRODUCTION

Ultrasound strain imaging has emerged as a tool for a wide range of biomedical applications. For high quality strain images, an accurate motion tracking method is required because strain tensor maps (i.e., spatial derivatives of displacements) and elasticity images (i.e., processed strain images removing the influence of mechanical boundary conditions [1]) are greatly dependent on the quality of displacement vector estimates. Computational costs must also be considered to assess the feasibility of implementing the technique in a real-time system.

The nature of sampled signals has raised the importance of sub-pixel displacement estimations which often dominate the signal-to-noise ratio (SNR) of displacement vectors. Many approaches to estimate sub-pixel displacements in ultrasound strain imaging have already been developed and reported [2-8]. The most straightforward approach to achieve sub-pixel precision is to interpolate the sampled signal and then to estimate displacements in terms of interpolated integer pixels [3]. In this case, however, computational costs are significantly increased by the interpolation factor and sub-pixel precision may not be enough. A spline-based algorithm [7] can be used to solve these problems but the method is still computationally expensive.

Another approach to estimate sub-pixel displacements is to interpolate pattern matching functions such as the normalized cross-correlation (NCC), sum of squared differences (SSD), and sum of absolute differences (SAD) [2, 4-6]. Using the linear phase property of the NCC function, the best pattern matching position (i.e., displacement) between two radiofrequency (RF) signals with sub-pixel precision can be obtained [4, 5]. However, to utilize phase information, the complex NCC function must be computed, and therefore, computational costs increase compared to curve-fit methods of pattern matching functions such as either parabola or cosine fit with either NCC, SSD, or SAD.

In these methods, bias error degrades displacement SNR [2]. Furthermore, for lateral displacement estimation, interpolating sparsely sampled lateral data was suggested to improve displacement SNR [8], and synthetic lateral phase was introduced to utilize the phase zero-crossing method in the lateral direction as well [6].

In this chapter, I introduce an autocorrelation-based speckle tracking error removal method to improve the performance of sub-pixel displacement estimation without significantly increasing the computational burden. The main goal is to remove sub-pixel estimation errors caused purely by curve-fitting interpolation (e.g., parabola, cosine, etc.). In this method, referred to as autocorrelation, the error can be estimated using the displacement between two identical frames. The autocorrelation method was quantitatively evaluated in strain imaging experiments using both simulated and tissue-mimicking phantom data.

3.2 APPROACH

Although I demonstrate the autocorrelation method on only parabolic interpolation of the NCC function, all other techniques based on curve-fitting of pattern matching functions would have the same source of estimation errors and can be improved by the autocorrelation method.

In one dimensional (1-D) parabolic interpolation, the sample corresponding to the peak of the NCC function and two samples neighboring the peak are used to determine the position of the peak with sub-pixel precision. The sub-pixel displacement, δ, obtained using 1-D parabolic interpolation is

$$\delta = \frac{R(l_{\max}-1) - R(l_{\max}+1)}{2\left(R(l_{\max}-1) - 2R(l_{\max}) + R(l_{\max}+1)\right)}, \tag{3.1}$$

where R(l) represents the correlation coefficient at correlation lag l, and lmax is the correlation lag where the correlation coefficient is the maximum.

Since the parabolic fit is not necessarily correct for a continuous NCC function, error is introduced [2]. This error depends not only on the sampling rate, but also on the details of the correlation function at a particular position. On average, the shape of the NCC function is determined by the point spread function (PSF) of the imaging system. At an individual pixel, however, the details of the scatterer distribution in that pixel modulate this average shape. The easiest way to reduce errors is to increase the data sampling rate so that the influence of parabolic interpolation errors can be minimized. However, increased data sampling rates lead to significant increases in computational cost.

Since sub-pixel displacement estimation using parabolic interpolation is imperfect, estimated displacements between identical frames are non-zero although there shouldn't be any motion. It can be assumed the non-zero displacements obtained using autocorrelation (i.e., correlation between identical frames) are sub-pixel displacement estimation errors related to the intrinsic curve-fit method and speckle statistics. Therefore, displacement estimation errors can be effectively removed by subtracting autocorrelation-based displacements from the displacements obtained using cross-correlation of two neighboring ultrasound frames captured during tissue deformation. Figure 3.1(a) illustrates a block diagram of the autocorrelation-based method. Using the same displacement estimator, the displacement between two neighboring frames (i.e., cross-correlation between reference and displaced frames) and the same frame (i.e., autocorrelation of the reference frame) are computed simultaneously. From the autocorrelation results, error patterns related to the intrinsic curve-fit method and speckle statistics are obtained. Then, by subtracting autocorrelation-based displacements from those obtained using cross-correlation, displacement errors produced by inaccurate curve-fit interpolation during sub-pixel displacement estimation are largely eliminated.

Although in this study only the reference frame was used for the autocorrelation, it is easily expanded to include both reference and displaced frames (Figure 3.1(b)).

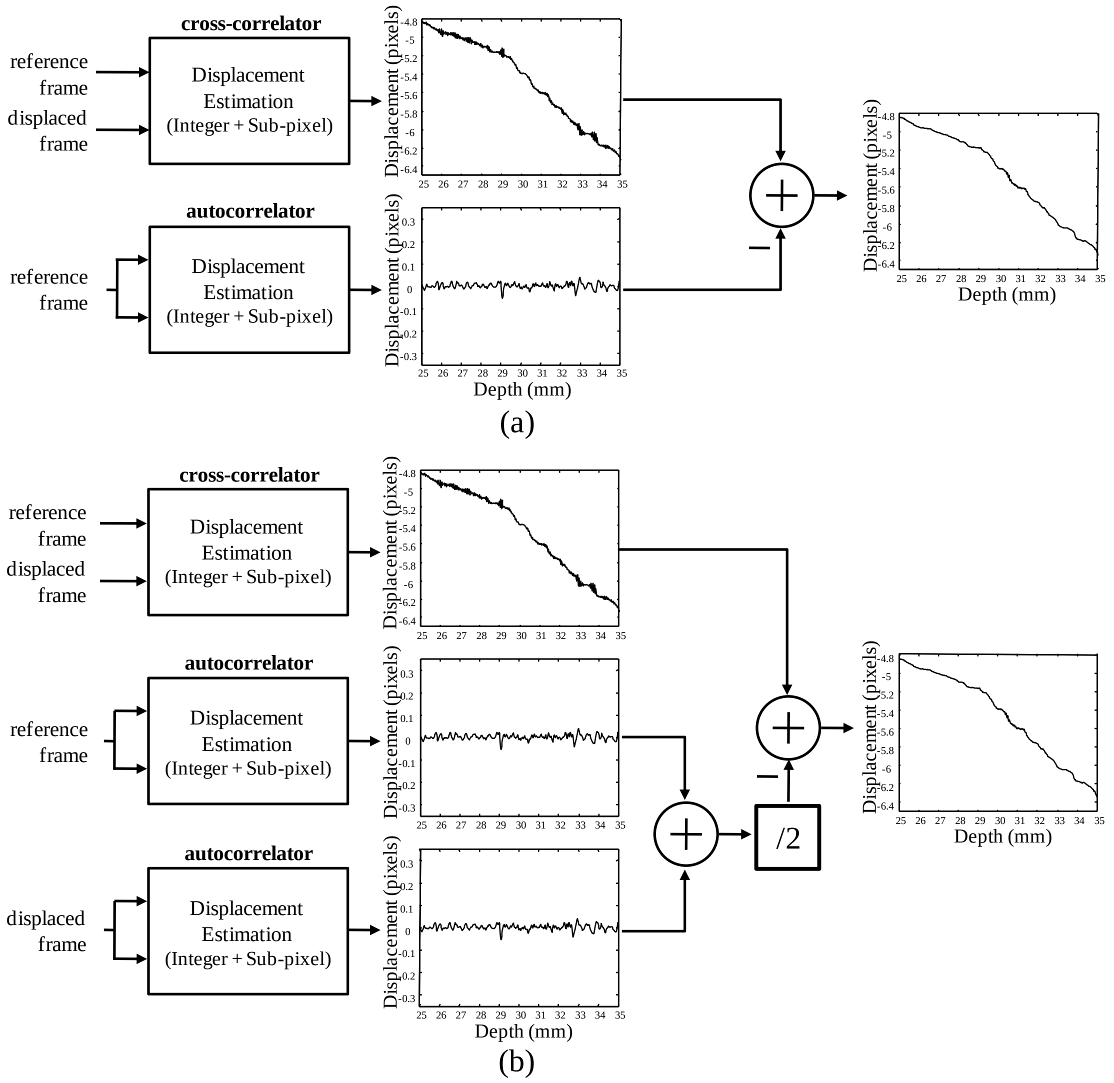

Figure 3.1: Block diagram of the autocorrelation-based method for improved sub-pixel displacement estimation. The autocorrelation output denotes displacement estimation errors related to the intrinsic method and speckle statistics. Clearly, outputs of the autocorrelation-based method do not have high frequency noise caused by sub-pixel estimation errors. The autocorrelation approach based on (a) reference frame and (b) both reference and displaced frames.

3.3 MATERIALS AND METHODS

3.3.1 Simulated Phantom

A phantom with a single, hard inclusion embedded into a homogenous medium was simulated. The 10-mm diameter circular inclusion had 50 times more randomly distributed scatterers compared to the background medium for contrast in ultrasound images. For contrast in elasticity images, the inclusion was twice as hard as the background material. To model the displacement and deformation of the phantom, a two-dimensional (2-D) analytical solution for an incompressible, uniformly deformed body with cylindrical inclusion was used [1]. Ultrasound modeling was based on far-field approximated linear acoustic wave propagation. Each element of the transducer (128-element linear array operating at 5 MHz) was assumed to be a point source and a detector with the directivity of a 300-μm wide acoustic radiator. The spatial impulse response of the transducer was modeled as a three-cycle sinusoid with a Hanning-weighted envelope corresponding to a 60% factional bandwidth. The backscattered ultrasound signal was captured using a 40 MHz sampling frequency [9].

3.3.2 Tissue-mimicking Phantom and Data Acquisition

Fabrication of the tissue-mimicking phantom closely followed the procedure described elsewhere [10]. Briefly, the background of the 40-mm by 50-mm by 60-mm cube shaped phantom was made out of 8% polyvinyl alcohol (PVA) solution and 1% 40-μm silica particles acting as ultrasound scatterers. For the inclusion, 10% PVA and 2% silica were mixed to fabricate the hyperechoic inclusion approximately 2.5 times harder than the background. The diameter of the cylindrical inclusion was 10-mm. During fabrication, the inclusion was positioned in the middle of the 50-mm by 60-mm region such that the circular cross-section of the inclusion was imaged.

RF data (128 beams, 2592 samples) were recorded using a Sonic RP ultrasound system (Ultrasonix Medical Corporation, Vancouver, BC, Canada) with 64 transmit channels and 32 receive channels for each ultrasound beam or scanline. A 128 element, 0.3048 mm pitch linear array transducer (L14-5/38, Prosonic Corporation, Korea) with a 5 MHz center frequency and 60% fractional bandwidth was used. Surface deformations up to 2.7% axial strain were applied in 0.3% increments using the surface of the transducer array itself. The RF data sampling frequency was 40 MHz.

3.3.3 Processing Algorithm and Signal-to-Noise Ratio

To track in-plane motion between two frames, a 2-D region was searched using a 2-D kernel. The kernel size was 0.64-mm (33 samples at 40 MHz) axially and 0.91-mm (3 out of 128 scanlines) laterally. For integer-pixel displacement estimations, the NCC was calculated. Then, sub-pixel displacements were estimated using parabolic interpolation of the NCC function in both axial and lateral directions, separately. To evaluate the effects of the developed autocorrelation-based method only, no post processing such as spatial filtering was applied. For the axial displacement, a phase-based sub-pixel displacement estimation method, called phase zero-crossing [4], was used to compare with the autocorrelation method. For the lateral displacement, linear interpolation (2, 4, and 8 folds) of lateral samples was performed and displacement estimation followed. The kernel size was kept the same at 0.91-mm laterally (i.e., 6 out of 256, 12 out of 512, and 24 out of 1024 scanlines).

Several regions of interest (ROIs) were used to compute the SNRs of axial and lateral displacements, as shown in Figure 3.2. Three vertically spread ROIs were used to analyze axial displacements, and three horizontally spread ROIs were used to analyze lateral displacements. The SNR was computed using the following equation

$$SNR = 20 \cdot \log_{10}\left(\frac{\sum_{ROI} ref(x,y)/N}{\sqrt{\left[\sum_{ROI} \left(ref(x,y) - est(x,y) \right)^2 \right] / N}} \right), \tag{3.2}$$

where ref(x,y) and est(x,y) are reference displacement and estimated displacement at the (x,y) position. In this equation, x and y are lateral and axial coordinates, respectively, where the axis of the ultrasound beam is directed along the y axis (Figure 3.2). In the tissue-mimicking phantom study, the linear-fit within a 2-mm window of estimated displacement obtained by the phase zero-crossing method was used for the axial reference displacement. For the lateral reference displacement, the linear-fit within a 5-mm window of estimated displacement obtained by the parabolic interpolation method using 1024 interpolated scan lines. The noise is defined as the difference between reference and estimated displacements.

Five different data sets for each applied strain were used to calculate SNR statistics. For 0.3% applied strain, for example, the displacements between frames 1 and 2, 2 and 3, 3 and 4, 4 and 5, and 5 and 6 were analyzed.

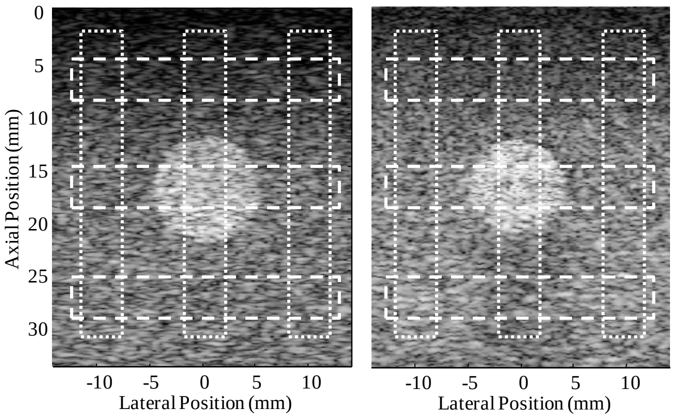

(a) (b)

Figure 3.2: Ultrasound images of (a) simulated phantom and (b) the tissue mimicking phantom. Regions of interest (ROIs) for axial and lateral displacements are outlined by dotted and dashed lines, respectively.

3.3.4 Computational Complexity

In correlation-based speckle tracking, the computational load is dominated by computation of the NCC function. The normalized computational cost, CNCC, for the normalized cross-correlation method is

$$C_{NCC} = \left[(K_A \times K_L) \times 3\right] \times (S_A \times S_L), \tag{3.3}$$

where K_A is the axial kernel size, K_L is the lateral kernel size, S_A is the axial search range, and S_L is the lateral search range. Here I consider only the number of multiplications because multiplications dominate computational complexity. The computational cost for a complex normalized cross-correlation is four times more expensive than C_{NCC} because of complex multiplications.

In contrast, to obtain either axial or lateral sub-pixel displacement estimation errors, the autocorrelation-based method requires only two more correlation coefficients, which are either R(-1,0) and R(1,0) or R(0,-1) and R(0,1) where R(x,y) represents the correlation coefficient at axial lag x and lateral lag y. Therefore, the normalized computational cost of the autocorrelation-based method can be derived as

$$\begin{aligned} C_{AC} &= C_{NCC} + \left[(K_A \times K_L) \times 3\right] \times 2 \\ &= \left[(K_A \times K_L) \times 3\right] \times (S_A \times S_L + 2) \end{aligned}. \tag{3.4}$$

Note that I consider only one direction (i.e., either axial or lateral direction) for computing the computational cost of the autocorrelation method.

3.4 RESULTS AND DISCUSSION

3.4.1 Axial Displacements

As expected, the SNR of the axial displacement for the autocorrelation method (i.e., parabolic interpolation of NCC function minus parabolic interpolation of autocorrelation function) is higher than that for the conventional cross-correlation method (i.e., parabolic interpolation of NCC function) for all deformation levels (Figure 3.3(a) for simulated and Figure 3.3(b) for tissue-mimicking phantom). This improvement was more pronounced at low deformation – this is expected since sub-pixel interpolation error is nearly the same for all deformations while the displacement is small for low deformation. In other words, sub-pixel displacement estimation errors play a more significant role for low deformations and, consequently, the autocorrelation method has greater impact.

The SNR of the autocorrelation method, however, is still lower than that of the phase-based approach. It is because the phase of the matching function (i.e., normalized complex cross correlation) can be modeled as a nearly perfect linear function while the magnitude of the matching function (i.e., normalized cross correlation) is not perfectly matched with a parabolic function. Although the autocorrelation method could not exceed the limit of the parabolic fit, and therefore, could not reach the SNR of the phase-based method, its additional computational cost is only about 22% of the conventional curve-fitting method. Furthermore, about 77% less computational load is required to implement the autocorrelation method compared to the phase zero-crossing method (Figure 3.3(c)).

For the phase zero-crossing method, some tradeoff between SNR and computational cost must be considered. Since computational cost is highly dependent on the search range (i.e., number of samples in the search window), skipping samples in the search window can decrease computational cost while the decrease of SNR by skipping samples is relatively small because of the strength of the linear fit to phase.

3.4.2 Lateral Displacements

Since lateral samples are more sparse than axial samples, the sub-pixel displacement estimation is critically important to the quality of lateral displacement estimation vectors. By applying the autocorrelation-based method, lateral displacement estimation errors were dramatically decreased. For 0.3% surface applied deformation of both simulated and tissue-mimicking phantoms, the autocorrelation-based method increases lateral displacement SNR by more than 12 dB compared to the conventional cross-correlation method (Figure 3.3(d) and Figure 3.3(e), respectively). The performance of the autocorrelation method for lateral displacements is nearly the same for the simulated phantom and even better for the tissue-mimicking phantom compared to the conventional method using 8-fold interpolated data (i.e., 1024 scanlines). The conventional method using 8-fold interpolated data requires about 64 times more computational resources, keeping the same size of kernel and search range, than original 128 scanline data (Figure 3.3(f)).

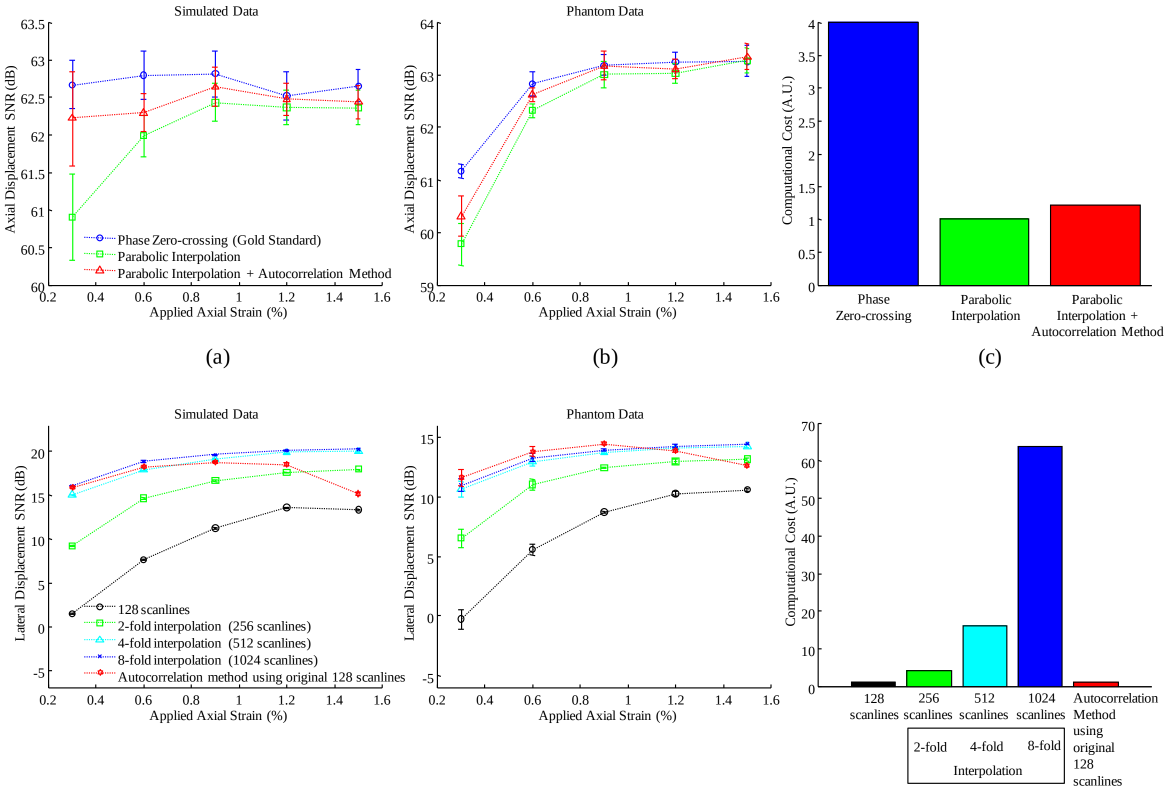

(a) (b) (c)

(d) (e) (f)

Figure 3.3: Axial and lateral displacement SNR for 0.3% to 1.5% axial deformations in 0.3% increments. (a) and (d) are for axial and lateral displacement SNR from the simulated phantom while (b) and (e) are from the tissue-mimicking phantom. (c) and (f) indicate computational cost comparisons for axial and lateral displacement estimators, respectively.

3.5 CONCLUSION

The results of this study suggest the autocorrelation-based method can be used for cost-effective real-time strain imaging. In particular, the autocorrelation method can significantly help in lateral displacement estimation.

REFERENCES

[1] A. R. Skovoroda, S. Y. Emelianov, and M. O'Donnell, "Tissue elasticity reconstruction based on ultrasonic displacementand strain images," IEEE

Transactions on Ultrasonics, Ferroelectrics and Frequency Control, vol. 42, pp. 747-765, 1995.

[2] I. Cespedes, Y. Huang, J. Ophir, and S. Spratt, "Methods for estimation of subsample time delays of digitized echo signals," Ultrason Imaging, vol. 17, pp. 142-71, 1995.

[3] E. Konofagou and J. Ophir, "A new elastographic method for estimation and imaging of lateral displacements, lateral strains, corrected axial strains and Poisson's ratios in tissues," Ultrasound Med Biol, vol. 24, pp. 1183-99, 1998.

[4] M. A. Lubinski, S. Y. Emelianov, and M. O'Donnell, "Speckle tracking methods for ultrasonic elasticity imaging using short-time correlation," IEEE Trans Ultrason Ferroelectr Freq Control, vol. 46, pp. 82-96, 1999.

[5] A. Pesavento, C. Perrey, M. Krueger, and H. Ermert, "A time-efficient and accurate strain estimation concept for ultrasonic elastography using iterative phase zero estimation," IEEE Trans Ultrason Ferroelectr Freq Control, vol. 46, pp. 1057-67, 1999.

[6] X. Chen, M. J. Zohdy, S. Y. Emelianov, and M. O'Donnell, "Lateral speckle tracking using synthetic lateral phase," IEEE Trans Ultrason Ferroelectr Freq Control, vol. 51, pp. 540-50, 2004.

[7] F. Viola and W. F. Walker, "A spline-based algorithm for continuous time-delay estimation using sampled data," IEEE Trans Ultrason Ferroelectr Freq Control, vol. 52, pp. 80-93, 2005.

[8] J. Luo and E. E. Konofagou, "Effects of various parameters on lateral displacement estimation in ultrasound elastography," Ultrasound Med Biol, vol. 35, pp. 1352-66, 2009.

[9] S. Park, S. R. Aglyamov, W. G. Scott, and S. Y. Emelianov, "Strain imaging using conventional and ultrafast ultrasound imaging: numerical analysis," IEEE Trans Ultrason Ferroelectr Freq Control, vol. 54, pp. 987-95, 2007.

[10] S. Park, S. R. Aglyamov, and S. Y. Emelianov, "Elasticity imaging using conventional and high-frame rate ultrasound imaging: experimental study," IEEE Trans Ultrason Ferroelectr Freq Control, vol. 54, pp. 2246-56, 2007.

Chapter 4: *Ultrasound Elasticity Imaging for Prostate Cancer Detection: Initial Clinical Study*

The results of this study have been presented at *Central Texas Clinical Research Forum* in 2009.

ABSTRACT

Ultrasound elasticity imaging for prostate cancer detection has been evaluated. 13 patients scheduled for prostatectomy surgery were participated in this study. Each patient was examined by ultrasound elasticity imaging before the surgery. Two sets of images obtained from convex and linear array transducers for transversal and sagittal planes of prostate were compared. After the surgery, the excised prostate was again examined by ultrasound elasticity imaging for the *ex-vivo* trial. All the elasticity imaging results were then compared with pathological analysis. The results of this study suggested that ultrasound elasticity imaging is a promising tool for prostate cancer detection. However, several concerns of this imaging technique need to be considered for better diagnosis of prostate.

4.1 INTRODUCTION

Prostate cancer is the second leading cause of men deaths caused by cancers in the United States [1]. Early detection of prostate cancer is essential to provide definitive treatment and improve patient survival. However, current screening and diagnostic tools for prostate cancer, such as Digital Rectal Examination (DRE), Trans-Rectal Ultrasound (TRUS), Prostate Specific Antigen test (PSA), and sextant biopsy, have limitations in terms of sensitivity and specificity. According to recent reports, the sensitivity and specificity of DRE are 37% and 91%, respectively [2]. TRUS sensitivity is higher (80%) than DRE, but specificity is low (37%) [3]. While PSA testing is the most widespread form of prostate cancer screening, its specificity of 63.1% and low sensitivity of 34.9% calls for more effective method [4]. Although sextant biopsy had very good specificity (100%), its sensitivity is 60% [5]. Therefore, it is required to have an assessment tool with high sensitivity and specificity in order to properly screen and diagnose prostate cancer at an early stage.

Ultrasound elasticity imaging can be utilized for cancer detection because this technique is capable of remotely mapping the elastic properties of tissue. The pathological changes in biological tissue are correlated with changes in tissue stiffness [6]. The standard medical practice of soft tissue palpation is based on qualitative assessment of tissue stiffness. Ultrasound elasticity imaging relies on applying a small compressive force to the tissue, and analysis of the ultrasound images before and after compression to estimate the internal strains. In clinical practice, tissue is deformed with an ultrasound probe while continuously imaging using the same transducer. Tissue motion is captured in real-time by recording consecutive frames of backscattered ultrasound signals. Internal motions and deformations in tissue between successive frames are measured using speckle tracking techniques. The necessary components of the displacement vector and strain tensor are measured, and then used to determine local elastic properties of tissue.

Although there were several clinical trials of using ultrasound elasticity imaging for prostate cancer detection [7-10], limitations and problems of this technique for the prostate were not well established. In addition, all the clinical trials for prostate cancer detection have used convex (or phased) endorectal array transducers which can image transversal planes of patients. In this study, I used both convex and linear array transducers for transversal and sagittal planes of prostate, respectively. The goal of this initial clinical study was not only to evaluate the feasibility of using ultrasound elasticity imaging for prostate cancer detection, but also to evaluate elasticity imaging performance for prostate between transversal and sagittal planes. Some limitations and problems of this technique for prostate cancer detection are addressed.

4.2 MATERIALS AND METHODS

4.2.1 Patients

13 patients undergoing prostatectomy surgery at the University of Texas M.D. Anderson Cancer Center participated in this study. The *in-vivo* elasticity imaging results were correlated with both *ex-vivo* elasticity imaging results and the pathological analysis of excised prostate obtained after the surgery. Among 13 patients, first 4 patients' data were used for training the physician who performed ultrasound elasticity exams. It was needed because that the physician's skills of compressing prostates determine the quality of elasticity images. After optimizing the imaging system based on the physician's technique to compress prostates using the transducer, 9 patients' data were used for analyzing the results of this study.

4.2.2 Data Acquisition and Elasticity Imaging Algorithm

Prior to prostatectomy, TRUS examination was performed using a Sonic RP ultrasound system (Ultrasonix Medical Corporation, Vancouver, BC, Canada) equipped with an endorectal transducer. On the transducer, two different array elements were installed: convex array for transversal plane and linear array for sagittal plane. During TRUS, about 5% deformation was applied to the prostate gland for ultrasound elasticity imaging. Ultrasound data were collected in real-time (*in-vivo*), and processed in off-line to make elasticity images. To examine the whole region of the prostate, 8 cross sections of prostate (3 transversal and 5 sagittal planes) were collected. The three transversal planes were apex, middle, and the base. The five sagittal planes were right far lateral, right, middle, left, and the left far lateral as shown in Figure 4.1.

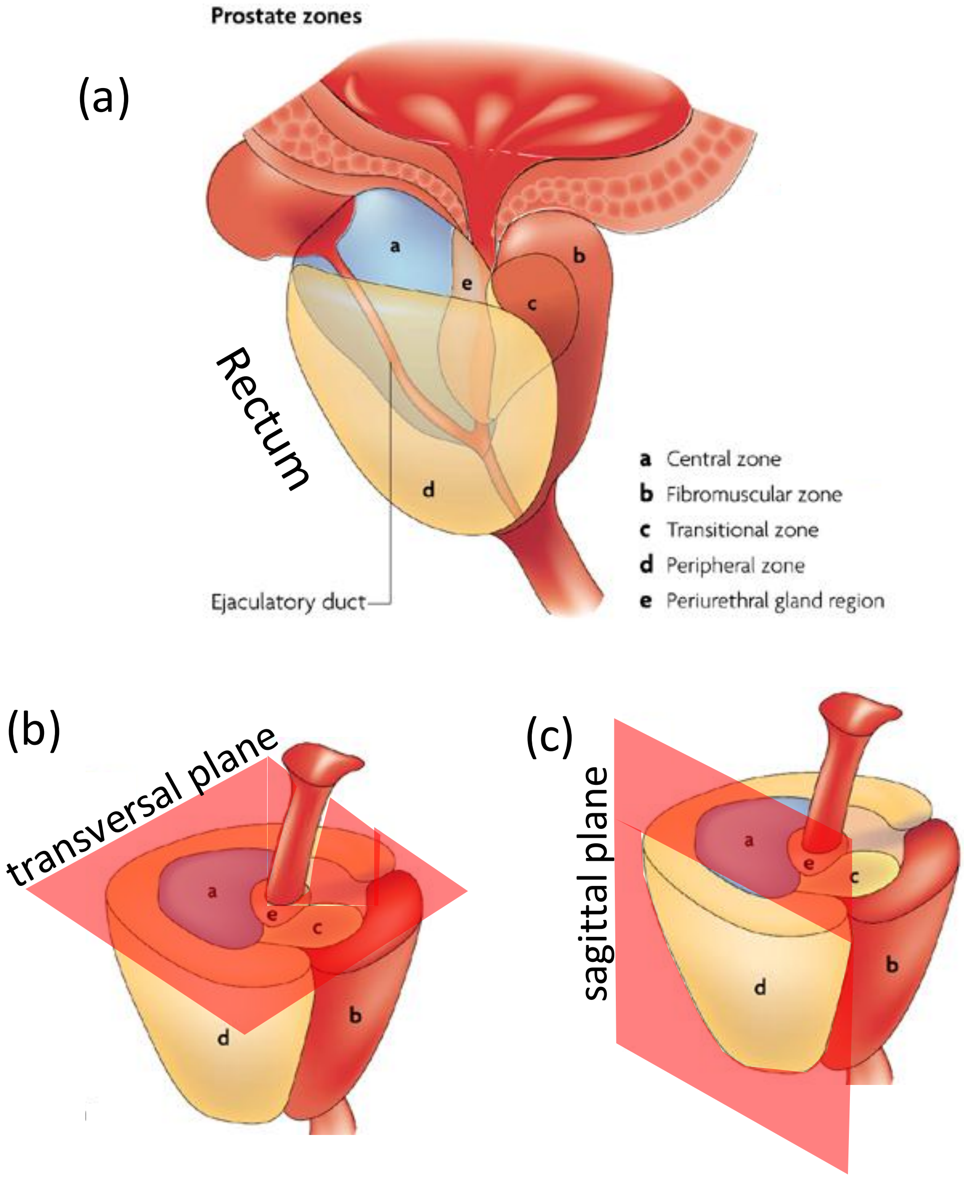

Figure 4.1: (a) Prostate anatomy and zones, (b) transversal plane of prostate, and (c) sagittal plane of prostate (Adapted from Nature Review Cancer)

After the surgery, the excised prostate was examined one more to compare the *ex-vivo* results with *in-vivo* results. Figure 4.2 shows the *ex-vivo* elasticity imaging examination using custom-made rubber holder for the excised prostate.

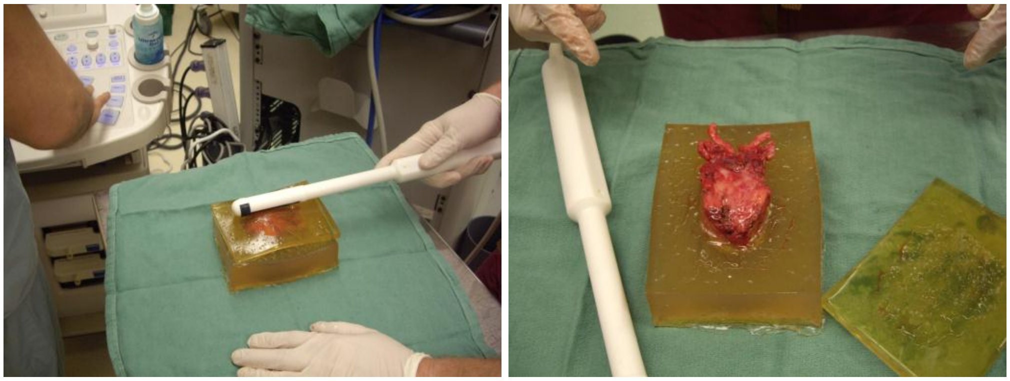

Figure 4.2: ex-vivo elasticity imaging examination

The elasticity imaging algorithm used for this study was presented in Chapter 3. Briefly, normalized cross-correlation was used for integer-level displacement estimation, and parabolic interpolation was used for sub-pixel level displacement estimation. In order to enhance the displacement estimation performance, the autocorrelation-based sub-pixel level displacement estimation method developed in Chapter 3 was utilized [11]. Using the same displacement estimator, the displacement between two neighboring frames (i.e., cross-correlation between reference and displaced frames) and the same frame (i.e., autocorrelation of the reference frame) are computed simultaneously. From the autocorrelation results, error patterns related to the intrinsic curve-fit method (i.e., parabolic interpolation) and speckle statistics are obtained. Then, by subtracting autocorrelation-based displacements from those obtained using cross-correlation, displacement errors produced by inaccurate curve-fit interpolation during sub-pixel displacement estimation are largely eliminated.

4.3 RESULTS AND DISCUSSION

4.3.1 Comparison between *In-vivo* and *Ex-vivo* Results

As expected, *in-vivo* and *ex-vivo* ultrasound elasticity imaging results were highly correlated. Figure 4.3 shows one example of *in-vivo* and *ex-vivo* comparison. The imaging plane of this example was right sagittal, which is placed between right far lateral and middle of prostate in sagittal planes. Thus, the right peripheral zone of the prostate was appeared as low strain, meaning hard region. Since cancerous tissue in prostate is usually harder than the normal tissue, it is suspected that there are prostate cancer foci in the right peripheral zone. This elasticity imaging analysis was then confirmed with pathological analysis of the excised prostate shown in Figure 4.4.

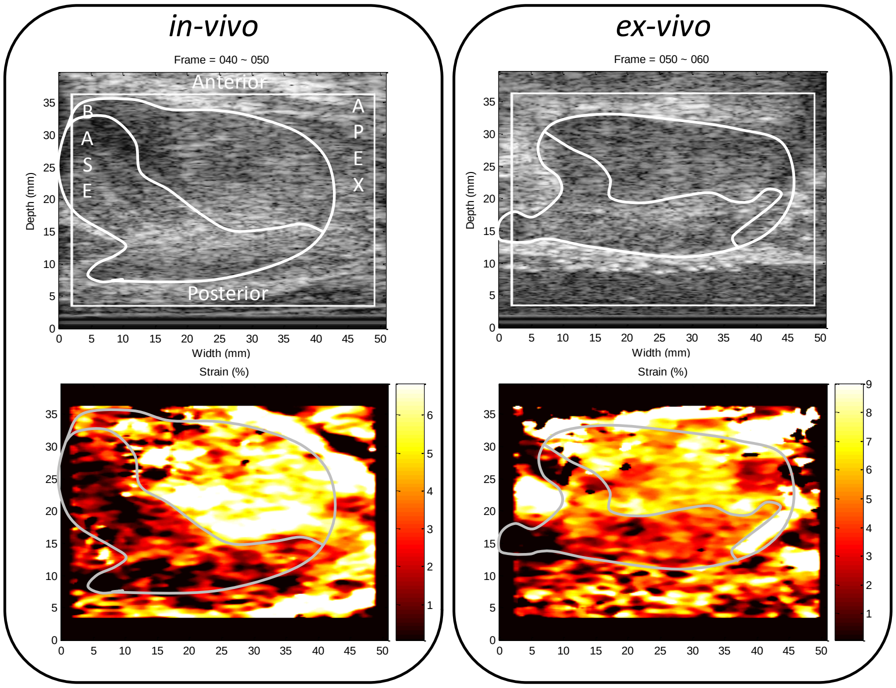

(a) (b)

Figure 4.3: Prostate ultrasound and elasticity images of (a) *in-vivo* and (b) *ex-vivo* examination (case #5). Outlines on images are manually drawn based on ultrasound and elasticity imaging results.

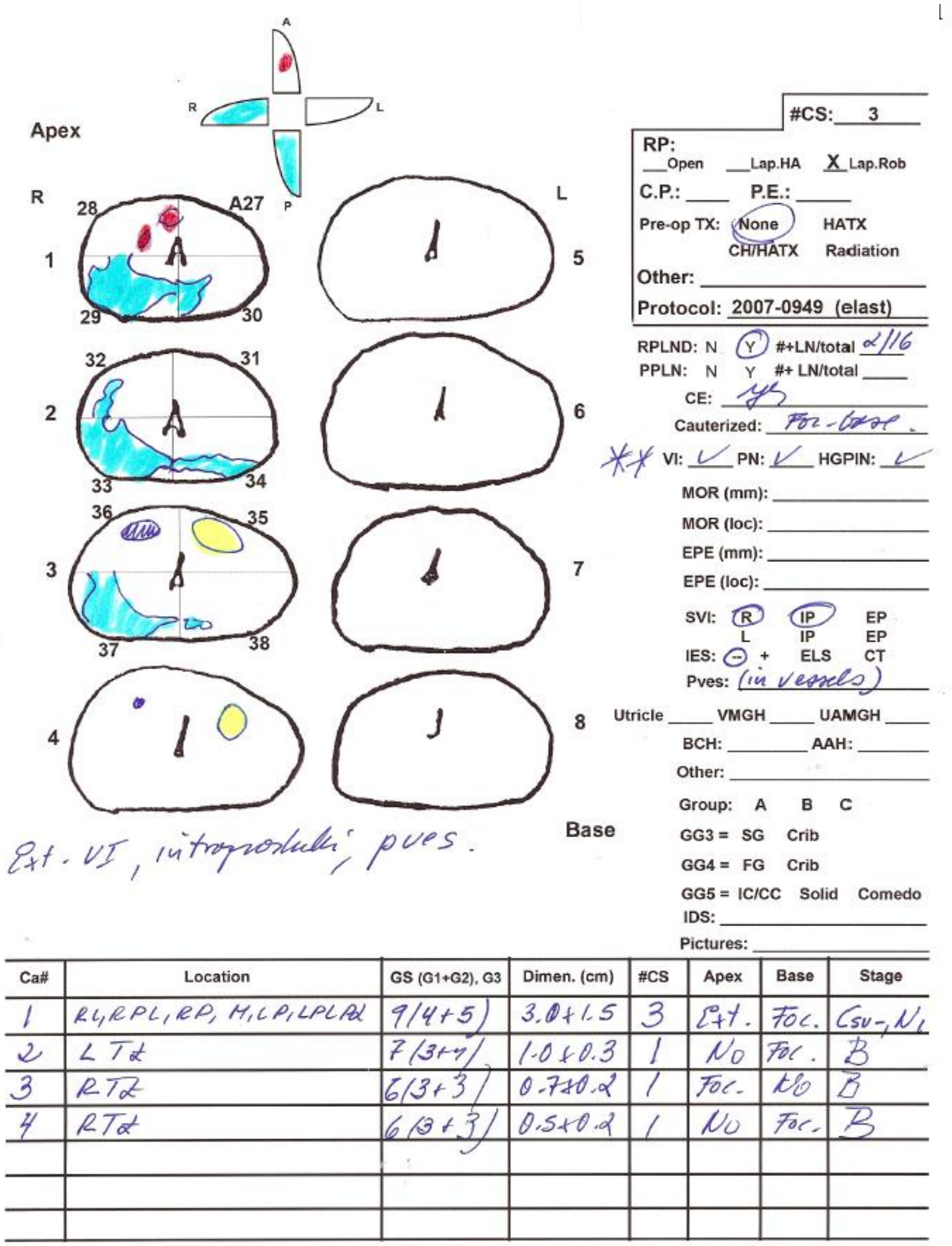

#CS: 3

RP:
___Open ___Lap.HA X Lap.Rob

C.P.: ____ P.E.: _____

Pre-op TX: [✓ None] HATX CH/HATX Radiation

Other: ____________

Protocol: 2007-0949 (elast)

RPLND: N [✓ Y] #+LN/total 2/16

PPLN: N Y #+ LN/total _____

CE: yes

Cauterized: Foc-base.

** VI: ✓ PN: ✓ HGPIN: ✓

MOR (mm): ____________

MOR (loc): ____________

EPE (mm): ____________

EPE (loc): ____________

SVI: [✓ R] [✓ IP] EP
L IP EP

IES: [✓ --] + ELS CT

Pves: (in vessels)

Utricle _____ VMGH _____ UAMGH _____

BCH: ________ AAH: ________

Other: ____________

Group: A B C

GG3 = SG Crib

GG4 = FG Crib

GG5 = IC/CC Solid Comedo

IDS: ____________

Pictures: ____________

Ext. VI, intraprostatic; pves.

Ca#	Location	GS (G1+G2), G3	Dimen. (cm)	#CS	Apex	Base	Stage
1	RL, RPL, RP, M, LP, LPLAL	9(4+5)	3.0×1.5	3	Ext.	Foc.	Csv-, N
2	LTZ	7(3+4)	1.0×0.3	1	No	Foc.	B
3	RTZ	6(3+3)	0.7×0.2	1	Foc.	No	B
4	RTZ	6(3+3)	0.5×0.2	1	No	Foc.	B

Figure 4.4: pathological analysis of the excised prostate (case #5).

From the pathological analysis, it was confirmed that the right peripheral zone had cancer focus at the base of the prostate and extended cancerous tissue up to the apex. The size of this cancer was 3.0 by 1.5 cm which was also observed by ultrasound elasticity imaging. In sum, *in-vivo*, *ex-vivo*, and pathological analysis have a good correlation, meaning that ultrasound elasticity imaging can detect prostate cancer.

4.3.2 Transversal Plane vs. Sagittal Plane

Ultrasound elasticity images of transversal planes were obtained by convex array transducer while images of sagittal planes were collected by linear array transducer. Figure 4.5 shows two examples of ultrasound elasticity examinations *in-vivo* using both convex and linear array transducers. Since the pathological analysis of the prostate was performed for only transversal planes, I marked red boxes on the pathological analysis chart which are corresponding to imaging cross-sections. In these two cases, good correlations between both transversal and sagittal elasticity images and pathological analysis were observed. Especially, urethra was appeared as very soft region as expected in both transversal and sagittal plane images.

In case #8, cancer focus at the left peripheral zone was clearly shown in the transversal elasticity image. Also, another cancer focus in the transitional zone at the apex was detected in sagittal elasticity image. Urethra position was also clearly shown.

In case #11, two big cancer foci at the left and right peripheral zone were detected by ultrasound transversal elasticity imaging. In the same transversal image, urethra was also shown as soft region. Another cancer focus in the transitional zone at the base was also detected by both ultrasound elasticity imaging and pathological analysis.

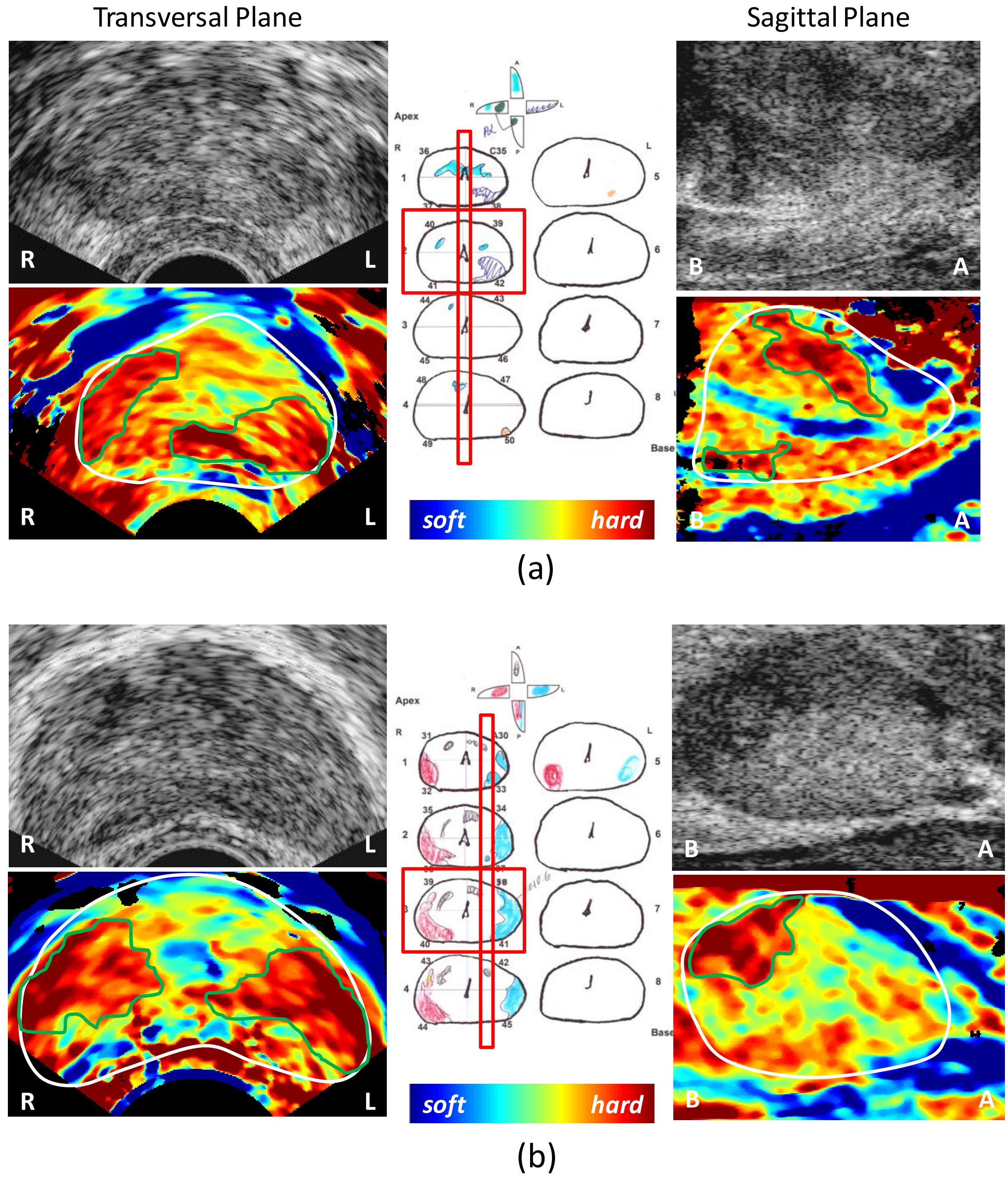

Figure 4.5: Ultrasound and elasticity images of transversal and sagittal planes obtained from (a) case #8 and (b) case #11. Pathological analysis is also shown here to compare it with elasticity imaging results.

4.3.3 Non-uniform Stress Field by Convex Array Transducer

Since ultrasound elasticity imaging relies on speckle motion induced by a transducer itself, it is important to uniformly compress tissue by the transducer. Then, an uniform stress field can be expected. Under a uniform stress field, strain can be directly related to the tissue stiffness.

Figure 4.6 shows one example of prostate imaging using the convex array transducer. In this case, the footprint of transducer is much smaller than the imaging plane (i.e., convex scan). Therefore, the pressure applied through the transducer can be easily directed to the center of the imaging plane. This effect can result in the non-uniform stress field, and therefore both side of prostate where less pressure is applied tend to be appeared as stiff region although it’s not. Therefore, it is required to access elasticity imaging results obtained by convex array transducers.

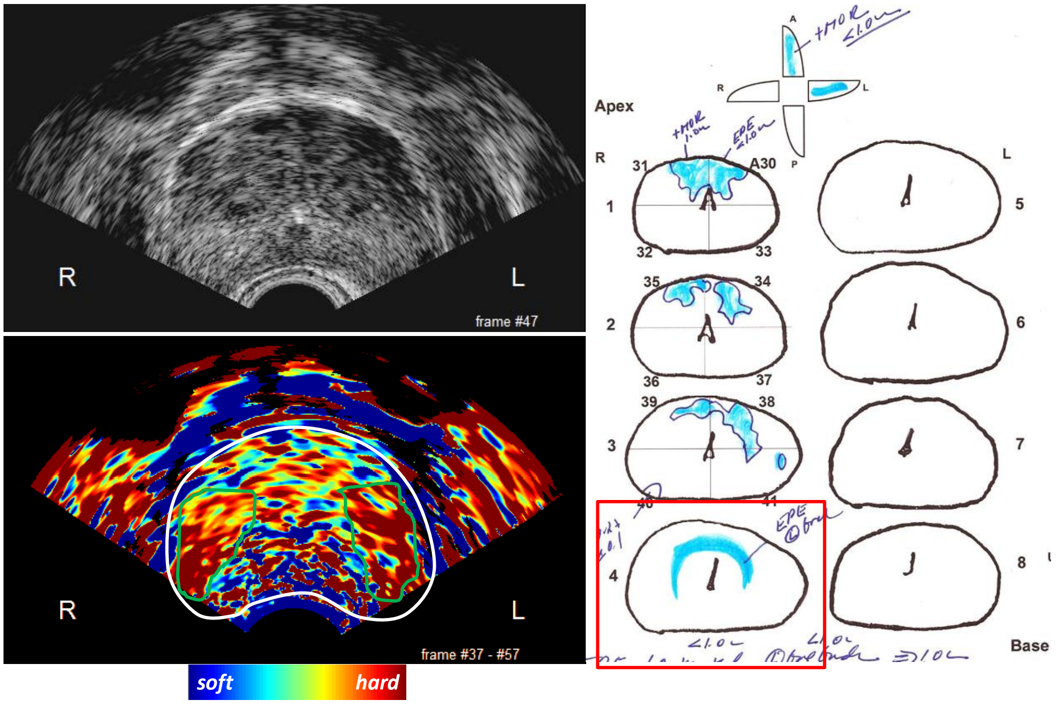

Figure 4.6: Example of strain image induced non-uniform stress field (case #9).

4.3.4 Lateral Motion by Convex Array Transducer

Since ultrasound elasticity imaging for the prostate application uses axial compression induced by the transducer, lateral motion needs to be minimized during the elasticity imaging examination. However, when convex array transducer was used, the prostate tends to move laterally because of small footprint of the transducer as well as loose connection between the prostate and connective tissue. Figure 4.7 shows one example of elasticity images when lateral motion was induced. Because of the unwanted lateral motion, left side of the prostate is appeared as harder region than left side.

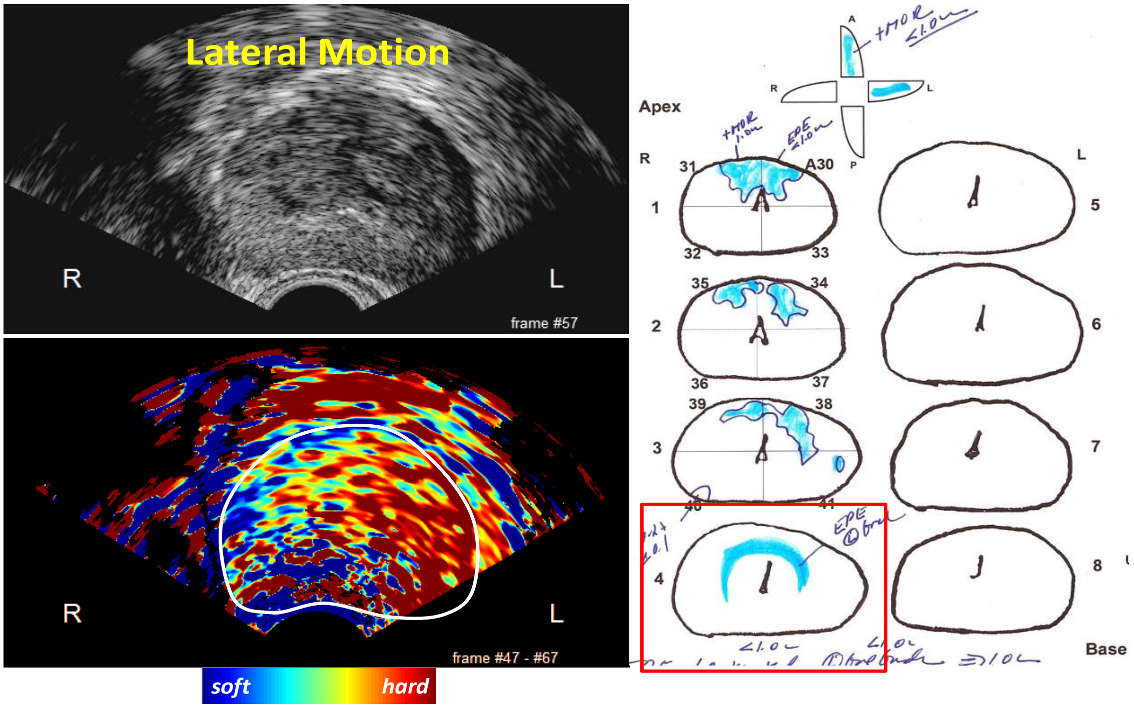

Figure 4.7: Example of strain image when lateral motion is induced (case #9).

4.4 CONCLUSION

The results of the study showed that ultrasound elasticity imaging can detect prostate cancer in both transversal and sagittal plane images. However, when the convex array transducer (i.e., transversal plane images) is used, more attention is required in order to produce uniform stress field to the prostate and not to make the prostate move laterally.

REFERENCES

[1] American Cancer Society, "Cancer Facts & Figures 2011," 2011.

[2] F. H. Schroder, P. van der Maas, P. Beemsterboer, A. B. Kruger, R. Hoedemaeker, J. Rietbergen, and R. Kranse, "Evaluation of the digital rectal examination as a screening test for prostate cancer. Rotterdam section of the European Randomized Study of Screening for Prostate Cancer," *J Natl Cancer Inst*, vol. 90, pp. 1817-23, 1998.

[3] R.Marco, S. Vincenzo, R. Marco, C. Paolo, M. Francesco, P. Alessandra, B. Roberto, C. Renzo, D.P. Luigi, F. Massimo, and R. Patrizio, "Role of prostate fossa ultrasonography in the diagnosis of local recurrence after radical prostatectomy in case of PSA failure," *Associazione ricerche in urologia*, vol. 74, pp. 304-308, 2002.

[4] S. Parpart, A. Rudis, A. Schreck, N. Dewan, and P. Warren, "Sensitivity and Specificity in Prostate Cancer Screening Methods and Strategies," *J. of Young Investigators*, vol. 16, 2007.

[5] M. K. Terris, "Sensitivity and specificity of sextant biopsies in the detection of prostate cancer: preliminary report," *Urology*, vol. 54, pp. 486-9, 1999.

[6] Y.C Fung, *Biomechanics: Mechanical properties of living tissues*. New York: Springer-Verlag, 1981.

[7] M. Tsutsumi, T. Miyagawa, T. Matsumura, N. Kawazoe, S. Ishikawa, T. Shimokama, T. Shiina, N. Miyanaga, and H. Akaza, "The impact of real-time tissue elasticity imaging (elastography) on the detection of prostate cancer: clinicopathological analysis," *Int J Clin Oncol*, vol. 12, pp. 250-5, 2007.

[8] L. Pallwein, M. Mitterberger, P. Struve, G. Pinggera, W. Horninger, G. Bartsch, F. Aigner, A. Lorenz, F. Pedross, and F. Frauscher, "Real-time elastography for

detecting prostate cancer: preliminary experience," *BJU Int*, vol. 100, pp. 42-6, 2007.

[9] G. Salomon, J. Kollerman, I. Thederan, F. K. Chun, L. Budaus, T. Schlomm, H. Isbarn, H. Heinzer, H. Huland, and M. Graefen, "Evaluation of prostate cancer detection with ultrasound real-time elastography: a comparison with step section pathological analysis after radical prostatectomy," *Eur Urol*, vol. 54, pp. 1354-62, 2008.

[10] T. Miyagawa, M. Tsutsumi, T. Matsumura, N. Kawazoe, S. Ishikawa, T. Shimokama, N. Miyanaga, and H. Akaza, "Real-time elastography for the diagnosis of prostate cancer: evaluation of elastographic moving images," *Jpn J Clin Oncol*, vol. 39, pp. 394-8, 2009.

[11] S. Kim, S. R. Aglyamov, S. Park, M. O'Donnell, and S. Y. Emelianov, "An autocorrelation-based method for improvement of sub-pixel displacement estimation in ultrasound strain imaging," *IEEE Trans Ultrason Ferroelectr Freq Control*, vol. 58, pp. 838-43.

SECTION 3: *PHOTOTHERMAL CANCER THERAPY GUIDED BY ULTRASOUND AND PHOTOACOUSTIC IMAGING*

In this section the improved spectroscopic photoacoustic imaging algorithm was developed, and the developed algorithm was used for *in-vivo* demonstration of photoacoustic image-guided photothermal therapy. Chapter 5 presents the enhanced spectroscopic photoacoustic imaging and its use for monitoring nanoparticle delivery before photothermal therapy. Chapter 6 presents all procedure of photothermal therapy guided by photoacoustic imaging.

Chapter 5: *In vivo Three-dimensional Spectroscopic Photoacoustic Imaging for Monitoring Nanoparticle Delivery*

The results of this study were published on *Biomedical Optics Express* in 2011.

ABSTRACT

In vivo monitoring of nanoparticle delivery is essential to better understand cellular and molecular interactions of nanoparticles with cells and to better plan nanoparticle-mediated photothermal therapy. I developed a three-dimensional ultrasound and photoacoustic (PA) imaging system and a spectroscopic PA imaging algorithm to identify and quantify the presence of nanoparticles and other tissue constituencies. Using the developed system and approach, three-dimensional imaging of a live mouse with tumor was performed before and after intravenous injection of gold nanorods. The developed spectroscopic PA imaging algorithm estimated distribution of nanoparticle as well as oxygen saturation of blood. Moreover, silver staining of excised tumor tissue confirmed nanoparticle deposition, and showed good correlation with spectroscopic PA images. The results of this study suggest that three-dimensional ultrasound-guided spectroscopic PA imaging can monitor nanoparticle delivery *in vivo*.

5.1. INTRODUCTION

Gold nanoparticles have been considered attractive contrast agents for photoacoustic molecular imaging [1-4], as well as therapeutic agents for photothermal therapy [5-7], because of high optical absorption properties, superior biocompatibility [8] and capability of molecular specific targeting of the cells. Monitoring of nanoparticle delivery is essential to better understand fundamental molecular pathways inside organisms and to better plan nanoparticle-mediated photothermal cancer therapy [9, 10]. The photoacoustic (PA) imaging technique can detect nanoparticles (NPs) based on 2 ways: quantitative changes of PA signals between pre- and post-injection of NPs and spectroscopic methods.

Single-wavelength PA imaging has been used to detect contrast agents in live mice based on changes of PA signal intensity [2, 11]. Unfortunately, analysis of PA signal at only one wavelength is prone to error because the increase of PA intensity can be caused not only by the deposition of contrast agents, but also by physiological changes (i.e., tumor growth, angiogenesis, etc.). Moreover, when longitudinal PA imaging is performed, the repeatability of the imaging experiments can be another problem because PA signals are linearly dependent with local laser fluence, which will be changed by tumor growth and re-positioning of the animal between imaging sessions. Multi-wavelength PA imaging (i.e., spectroscopic PA imaging) can be a solution to overcome the problems of single-wavelength PA imaging.

The spectroscopic PA imaging technique mainly relies on a tissue-dependent optical absorption spectrum. It can, therefore, distinguish different types of tissue such as oxyhemoglobin, deoxyhemoglobin, and lipid [12, 13]. Spectroscopic PA imaging has also been used to detect NPs based on PA spectrum and NP absorption spectrum [1, 14, 15]. However, in order to utilize spectroscopic PA imaging for *in vivo* detection of NPs, a more robust imaging algorithm needs to be developed.

In this chapter, I present an *in vivo* spectroscopic PA imaging algorithm as well as a three-dimensional (3-D) ultrasound (US) and PA imaging system. The developed system and algorithm were used for the detection of polyethylene glycol (PEG)-coated (PEGylated) gold nanorods injected into the tail vein of a mouse bearing a subcutaneous tumor. The results of spectroscopic PA imaging before (i.e., control) and 31 hours after the NP injection showed that the developed system and algorithm can detect NPs *in vivo*. Moreover, silver staining of the excised tumor tissue confirmed the NP deposition, and showed good correlation with spectroscopic PA imaging results.

5.2. MATERIALS AND METHODS

5.2.1 Nanoparticles

PEGylated gold nanorods (PEG-Au NRs) were synthesized for this study. First, cetyltrimethylammonium bromide (CTAB)-stabilized gold nanorods were prepared with a seed-mediated growth method [16]. Then the CTAB was replaced by mPEG-thiol through ligand exchange. The prepared PEG-Au NRs were characterized by ultraviolet-visible (UV-Vis) spectroscopy and transmission electron microscopy (TEM). The absorbance spectrum of PEG-Au NRs measured by UV-Vis spectroscopy is shown in Figure 5.1, and compared with the absorption spectra of deoxyhemoglobin (Hb) and oxyhemoglobin (HbO2) reported in literature [17]. The wavelength of PEG-Au NRs' peak absorbance was about 790 nm, and the size of PEG-Au NRs, derived from the TEM image as shown in Figure 5.1, was about 40 nm by 10 nm.

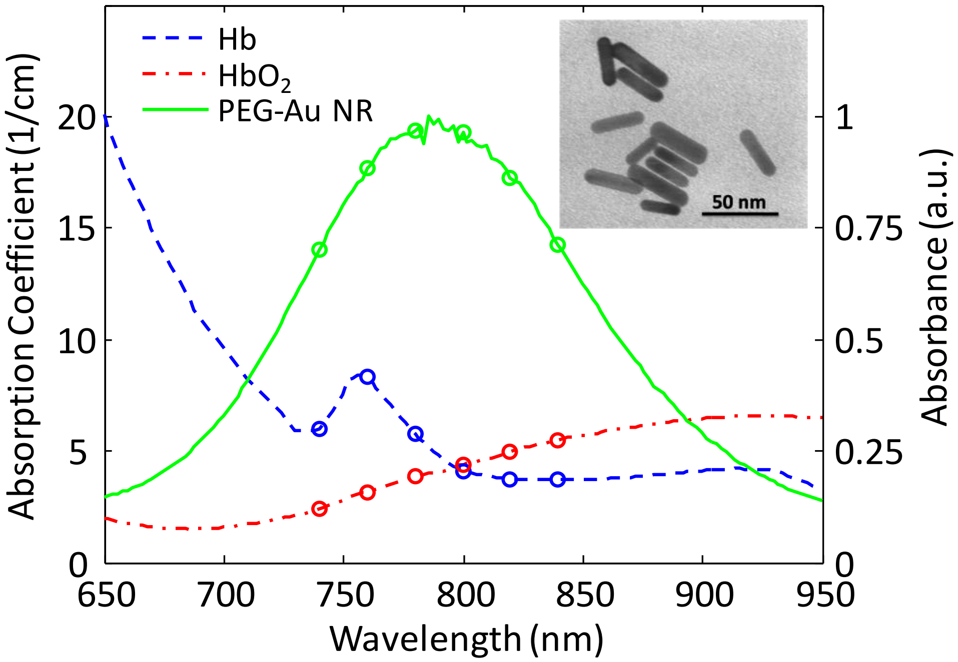

Figure 5.1: The absorption spectra of deoxyhemoglobin (Hb, blue dashed line) and oxyhemoglobin (HbO2, red dash-dotted line) [17] compared to the absorbance spectrum of the PEGylated gold nanorod (PEG-Au NR, green solid line) measured by UV-Vis spectroscopy. Dots on each line correspond to wavelengths used for spectroscopic photoacoustic imaging. The transmission electron microscopy (TEM) image of PEG-Au NRs is also shown.

5.2.2 Mouse bearing a subcutaneous tumor

A 3-month old immunodeficient nude mouse (Nu/Nu) weighing about 18 g was used for this study. Human cancer cells (A431 cell line) were subcutaneously injected on the right flank of the mouse. The injected cells were grown for 20 days resulting in a tumor size of about 10 mm in diameter. Then two imaging sessions were performed: before (control experiment) and 31 hours after NP injection. A NP solution of 200 µL was injected intravenously via a tail vein. The amount of gold in the 200 µL NP solution was 400 µg. During imaging sessions, the mouse was anesthetized with a combination of isoflurane (0.5 ~ 2.0%) and oxygen (0.5 L/min). After the second imaging session, the mouse was euthanized by carbon dioxide (CO2) asphyxiation, and the tumor was excised for histological analysis (i.e., silver staining). All these procedures were performed under the animal protocol approved by Institutional Animal Care and Use Committee (IACUC) at The University of Texas at Austin.

5.2.3 *In vivo* imaging system

A 3-D US and PA imaging system developed for in vivo mouse imaging is shown in Figure 5.2. A tunable laser system consisting an optical parametric oscillator (OPO) (PremiScan, Spectra-Physics) pumped by Q-switch Nd:YAG laser (Quanta-Ray PRO-Series, Spectra-Physics) was capable of producing 7 ns pulses at 10 Hz pulse repetition frequency. The overall spectral range of the system was from 400 to 2300 nm wavelength. For this study, I used 6 wavelengths ranging from 740 to 840 nm with an increment of 20 nm (i.e., 740, 760, 780, 800, 820, and 840 nm). The diameter of round-shaped Gaussian laser beams was consistently 12 mm for all wavelengths, and the maximum laser fluence for all wavelengths was 25 mJ/cm^2 satisfying an American National Standards Institute (ANSI) limit (i.e., ~30 mJ/cm^2) [18]. The pulse-to-pulse laser energy was monitored and recorded using a laser power meter (Nova II, OPHIR) – the power meter readings were then used to compensate for laser energy variation during off-line PA image reconstruction.

A water tank was used for acoustic coupling between the linear array transducer and the skin of the mouse and for maintaining the body temperature of anesthetized mouse. Water temperature was kept at 37°C during experiments using a water circulation system (Isotemp 3013H, Fisher). In order to keep both a transducer-cable connection and the mouse head above water, I constructed an imaging platform to diagonally secure the mouse. The imaging platform was connected to a 1-D motorized system (BiSlide, VELMEX) to scan the mouse for 3-D imaging.

Two systems – SonixRP by Ultrasonix, Inc., and WP32 by WinProbe, Inc., were used for US and PA imaging, respectively. The SonixRP system was chosen for US imaging because of its ability to quickly capture high quality US images with multiple focal zones, while the WP32 system allowed simultaneous access to 32 channel data needed for fast PA imaging. Both systems were interfaced with the same linear array transducer (L12/128 by Vermon, 128 elements, 9 MHz center frequency, 5.8 MHz bandwidth) to collect either pulse-echo US or PA signals. For one 2-D US image, 128 beams of radiofrequency (RF) signals (i.e., beamformed US data) were collected using 64 transmit- and 32 receive-channels, requiring acquisition time of about 0.025 seconds. In PA imaging mode, 4 laser pulses were required for one full data set of 128 RF signals (i.e., pre-beamformed PA signals). Moreover, to enhance signal-to-noise ratio (SNR), 32 PA pre-beamformed RF signals were averaged requiring 128 laser pulses for one PA image. The acquisition time for one frame of PA image was 12.8 seconds. The PA image reconstruction (or, in other words, beamforming) was performed off-line.

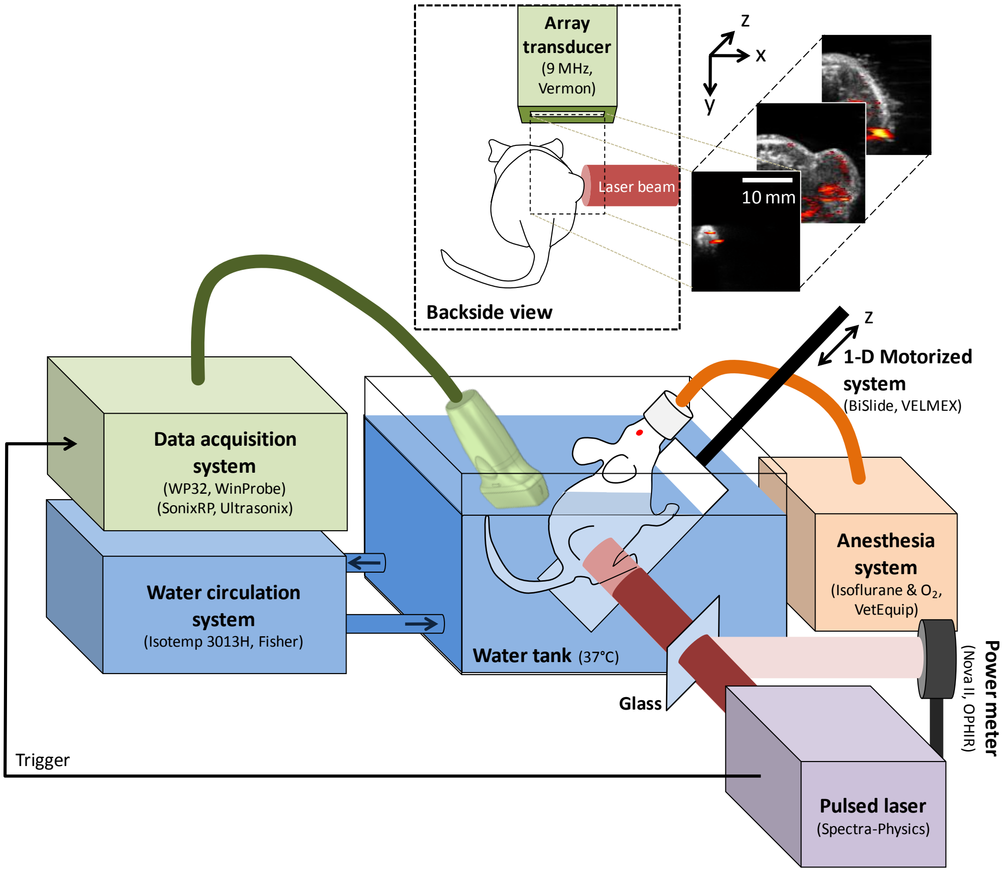

Figure 5.2: Schematic diagram of the developed *in vivo* three-dimensional ultrasound and photoacoustic imaging system.

5.2.4 Spectroscopic photoacoustic imaging

Photoacoustic imaging

The collected PA signal was first filtered using a 128th order finite impulse response (FIR) bandpass filter. The cutoff frequency of the filter was determined based on the measured bandwidth of the transducer (9 MHz center frequency and 5.6 MHz bandwidth). Then the 32 bandpass filtered PA signals from each element were averaged in order to enhance SNR. The PA images were reconstructed using a delay-and-sum beamforming [19]. Specifically, the 128 PA signals were used to generate 96 scanlines or beams (i.e., beamformed data) covering a 96-element aperture positioned in the middle of the array. A Hamming window was applied for aperture apodization during the beamforming. This suppressed side-lobes of the PA beam, and therefore to enhance contrast-to-noise ratio (CNR) while widening a main lobe, and thus slightly degrading lateral spatial resolution. The PA beamformed RF data were down-converted by taking the absolute values of Hilbert transform of RF data. The PA images were then displayed using a linear scale.

Depth- and wavelength-dependent fluence compensation of photoacoustic signal

Assuming both stress and thermal confinements are satisfied, the PA maximum pressure, p_0, at the pressure source can be expressed as follows [20]

$$p_0(\lambda,\mathbf{r}) = \Gamma(\mathbf{r})\mu_a(\lambda,\mathbf{r})F(\lambda,\mathbf{r}), \tag{5.1}$$

where Γ is the local ($\mathbf{r}$) Grüneisen parameter, μ_a is wavelength (λ) dependent local ($\mathbf{r}$) optical absorption coefficient, and F is wavelength-dependent local laser fluence. Both the optical absorption coefficient and the Grüneisen parameter are tissue-dependent. The Grüneisen parameter is defined by the volume expansion coefficient (β), the speed of sound (v_s) and the heat capacity at constant pressure (C_p)

$$\Gamma = \frac{\beta v_s^2}{C_p}. \tag{5.2}$$

The distribution of the laser fluence depends on optical properties of the tissue and laser light delivery system (e.g., beam profile, incident laser fluence, etc.).

In this study, wavelength-dependent local fluence was estimated using the approach presented in Figure 5.3 (steps 1-3). First, the imaged tissue was segmented by tissue type. Specifically, skin and background tissue were identified and skin thickness was determined from US images (Figure 5.3, step 1). Then, using Beer's law, the fluence was estimated using a simple 2-D skin-tissue two-layer model (Figure 5.3, step 2)

$$F(\lambda,\mathbf{r}) = F_0(\lambda)e^{-\mu_{eff}(\lambda,\mathbf{r})|\mathbf{r}|}, \tag{5.3}$$

where $F_0(\lambda)$ is wavelength-dependent incident fluence measured by a laser power meter during experiments, $|\mathbf{r}|$ is the distance between skin and position, $\mathbf{r}$, within the tissue, and $\mu_{eff}(\lambda,\mathbf{r})$ is both wavelength- and tissue-dependent effective attenuation coefficient defined as

$$\mu_{eff} = \sqrt{3\mu_a(\mu_a + \mu_s^{'})}, \tag{5.4}$$

where μ_a and $\mu_s^{'}$ are absorption and transport scattering coefficients, respectively. The optical properties of mouse skin and tumor were obtained from literature [21]. Finally, PA signal was compensated using the derived fluence map (Figure 5.3, step 3). Note that the analysis described by steps 1-3 was performed for every optical wavelength resulting in wavelength- and depth-dependent fluence compensation of PA signal.

Spectral analysis

Assuming there are three major optical absorbers in a body (i.e., oxyhemoglobin (HbO_2), deoxyhemoglobin (Hb), and nanoparticle (NP)), the absorption coefficient of localized mouse tissue can be defined by the sum of absorption coefficients for HbO_2, Hb, and NP in the region. Note that the absorption coefficient (μ_a) is the product of the molar absorption coefficient (ε) and the molar concentration (C) of the absorber. Therefore, the wavelength-dependent local absorption coefficient (i.e., $\mu_a(\lambda,\mathbf{r})$) can be described as

$$\mu_a(\lambda,\mathbf{r}) = C_{HbO_2}(\mathbf{r})\varepsilon_{HbO_2}(\lambda) + C_{Hb}(\mathbf{r})\varepsilon_{Hb}(\lambda) + C_{NP}(\mathbf{r})\varepsilon_{NP}(\lambda), \tag{5.5}$$

where C_{HbO2}, C_{Hb}, and C_{NP} are the molar concentrations [M] of HbO_2, Hb, and NP, respectively, and ε_{HbO2}, ε_{Hb}, and ε_{NP} are the molar absorption coefficients [$cm^{-1}M^{-1}$] of HbO_2, Hb, and NP, respectively. Given depth- and wavelength-dependent fluence compensation, the measured local PA spectrum ($p_0(\lambda,\mathbf{r})$) can be directly related to the local absorption spectrum ($\mu_a(\lambda,\mathbf{r})$) (see Eq. (1)). Linear least squares (LLS) method can resolve the concentrations of multiple absorbers, and therefore distinguish tissue components [12]. Moreover, the resolved HbO_2 and Hb concentrations can be used for estimating oxygen saturation in blood. However, the LLS method often predicts negative concentrations due to imperfect fluence compensations, noise in the measurements, contribution to PA signals from other optical absorbers, etc. Because a negative concentration has no physical meaning, it negates the calculated concentrations of the other absorbers at that location.

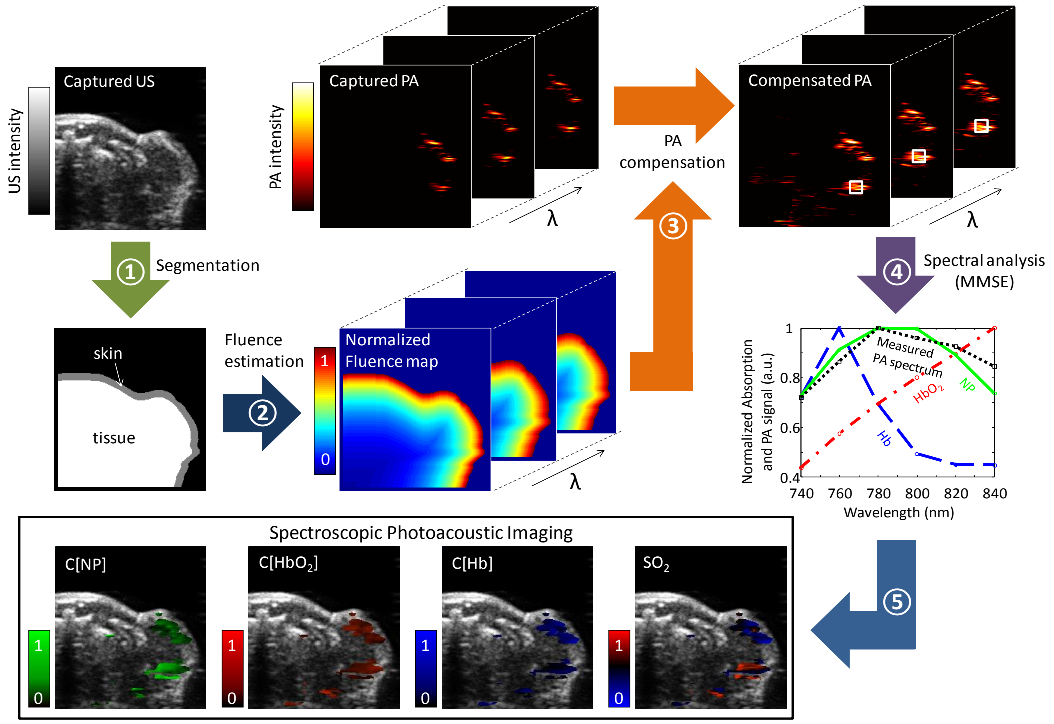

Figure 5.3: Schematic diagram of the developed spectroscopic photoacoustic imaging algorithm.

To overcome the problems of the LLS method for *in vivo* deep penetration imaging, I have developed a robust, less noise-sensitive PA spectral analysis algorithm that minimizes the mean square error while maintaining positive concentrations for each absorber (Figure 5.3, step 4). Each molar absorption spectrum ($\varepsilon(\lambda)$) of HbO_2, Hb, and NP within the used wavelength range ($\lambda_1 < \lambda < \lambda_2$) was first normalized as

$$\varepsilon^*(\lambda) = \frac{\varepsilon(\lambda)}{\max\left[\varepsilon(\lambda)\right]_{\lambda_1<\lambda<\lambda_2}}. \tag{5.6}$$

Then the local absorption spectrum ($\mu'_a(\lambda,\mathbf{r})$) can be described as

$$\mu'_a(\lambda,\mathbf{r}) = C[HbO_2](\mathbf{r})\varepsilon^*_{HbO_2}(\lambda) + C[Hb](\mathbf{r})\varepsilon^*_{Hb}(\lambda) + C[NP](\mathbf{r})\varepsilon^*_{NP}(\lambda), \tag{5.7}$$

where $C[HbO_2]$, C[Hb], and C[NP] are the contribution levels of the HbO_2, Hb, and NP absorption spectra. By varying $C[HbO_2]$, C[Hb], and C[NP] from 0 to 1, and setting the sum of them to one (i.e., $0 < C[HbO_2], C[Hb], C[NP] < 1$ and $C[HbO_2]+C[Hb]+C[NP] = 1$), the local absorption spectrum of all possible combinations of HbO_2, Hb, and NP contributions at a position **r** can be reconstructed into $\mu'_a(\lambda,\mathbf{r})$. Then $\mu'_a(\lambda,\mathbf{r})$ is normalized in order to compare it with the normalized local PA spectrum (i.e., $p_0^*(\lambda,\mathbf{r})$) in a mean square error (MSE) sense:

$$MSE = E\left[\left(p_0^*(\lambda,\mathbf{r}) - \mu_a'^*(\lambda,\mathbf{r})\right)^2\right]. \tag{5.8}$$

Note that local PA intensity was defined by averaging PA signals inside a kernel (500 μm axially, 500 μm laterally, and 500 μm elevationally). The kernel size was selected to be larger than axial and lateral spatial resolutions of PA images. The values of $C[HbO_2]$, C[Hb], and C[NP] in Eq. (5.7) were numerically determined by minimizing the mean square error (MSE) of Eq. (5.8). Then minimum mean square errors (MMSEs) were used for reliability of the results.

The main difference between the MMSE method and the LLS method is that I allow constraints to be placed on the solution. However, the solutions from each approach are the same if the solution of the LLS method already satisfies the constraints. In addition, the MMSE method is numerical approach, and thus computationally intensive while the LLS method has an analytical solution, and benefits from fast computation. Therefore, I used the numerical method only if the solution of the LLS analysis has negative values. By combining both approaches, I achieved the development of a fast, and less noise-sensitive spectroscopic PA imaging algorithm.

In this study, the MMSE of 0.005 was used for the threshold of the results. This is quite a strong constraint for reasonable analysis. The contribution levels of HbO_2, Hb, and NP (i.e., C[HbO_2], C[Hb], and C[NP]) were then used for visualizing the distributions of each. In order to estimate oxygen saturation (SO_2) of blood, the following equation was used

$$SO_2 = \frac{C_{HbO_2}}{C_{HbO_2} + C_{Hb}} = \frac{C[HbO_2]}{C[HbO_2] + nC[Hb]}, \tag{5.9}$$

where n is the scaling factor defined as

$$n = \frac{\max\left[\varepsilon_{HbO_2}(\lambda)\right]_{\lambda_1<\lambda<\lambda_2}}{\max\left[\varepsilon_{Hb}(\lambda)\right]_{\lambda_1<\lambda<\lambda_2}}. \tag{5.10}$$

Note that ε^*_{HbO2} to ε^*_{Hb} ratio is no longer the same as ε_{HbO2} to ε_{Hb} ratio (see Eq. (5.6)), and therefore a scaling factor needs to be considered to calculate the molar concentrations.

Figure 5.3 summarizes the developed spectroscopic PA imaging algorithm consisting of depth- and wavelength-dependent fluence compensation and spectral analysis of PA signal.

5.2.5 Histological analysis (silver staining)

To confirm the result of spectroscopic PA imaging, especially concentration of NPs (C[NP]) after the injection, the mouse was euthanized and tumor was excised right after the second imaging session (i.e., 31 hours after NP injection) for histological analysis. The excised tumor was carefully marked for location and orientation of spectroscopic PA imaging planes. A total of 4 evenly distributed histological slides were made, and silver stained to identify depositions of gold NPs. Since silver staining has enhanced contrast to gold in bright-field microscopic images, I used silver staining slides to visualize the distribution of gold NPs in the tumor. The corresponding 2-D images of NPs in tissue (C[NP]) were compared with silver stained tissue slides.

5.3. RESULTS

Comparison of linear least square (LLS) and minimum mean square error (MMSE) methods is presented in Figure 5.4. The US image (Figure 5.4(a)) was used to generate a 2-D skin-tissue two-layer structure for the laser fluence compensation. As an example, the compensated PA image at 800 nm is shown in Figure 5.4(b). Since the LLS method generates negative concentration values (Figure 5.4(c)), some areas with strong PA signal are not mapped with optical absorbers (Figure 5.4(d)). By applying the developed MMSE method, however, NP concentration can be reliably reconstructed (Figure 5.4(e)). White arrows in Figure 5.4(e) indicate locations and concentrations of NPs missed by LLS method, but recovered by MMSE method. Therefore, the developed spectroscopic PA imaging algorithm based on MMSE analysis can reconstruct the concentrations of optical absorbers in the region where LLS method fails due to negative concentration of photoabsorbers.

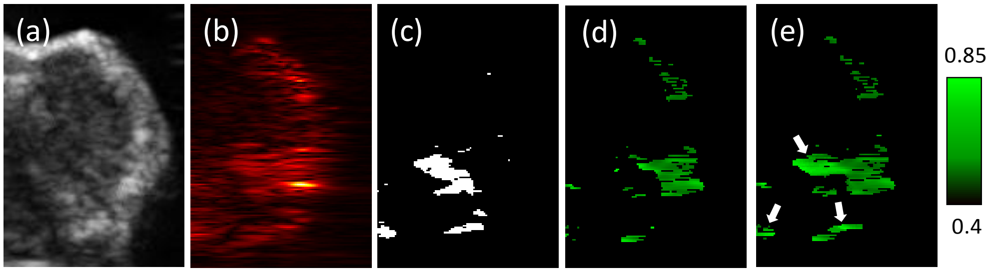

Figure 5.4: Comparison between linear least square (LLS) and minimum mean square error (MMSE) methods. Ultrasound image (a) was used for the skin-tissue segmentation. The fluence compensated photoacoustic image (b) at 800 nm is shown as a reference. Spectral analysis based on LLS method can produce negative concentrations (c) of optical absorbers due to imperfect fluence compensations, noisy measurements, etc. The regions producing a negative NP concentration by LLS method get removed from the NP image. (d). However, the developed MMSE method can reliably reconstruct spatial distribution and concentration of NP – white arrows in panel (e) indicate locations where NP concentrations were recovered using MMSE method.

The spectral analysis based on MMSE method was applied to identify presence and concentration of major photoabsorbers in mouse tumor *in vivo*. The 3-D US images show mouse tumor morphology (i.e., tumor size and location) as well as overall outline of the mouse body. Tumor growth during the 31 hours between the two imaging sessions was recognizable in the 3-D US images presented in Figure 5.5(a) and Figure 5.5(g).

Single-wavelength PA images obtained at 800 nm (Figure 5.5(b) and Figure 5.5(h)) show optical absorption contrasts in the mouse body. Since I compensated PA signals based on local fluence changes estimated from a 2-D skin-tissue two-layer model, the color intensity on the images is proportional to the optical absorption of tissue (assuming that Grüneisen parameters of tissues are the same, see Eq. (1)). Within the tumor region, the PA signal distribution before and after the NP injection is significantly different. The increased PA signal generation is most likely due to NP deposition in the tumor. However, such a conclusion must be verified because PA signal increase could also be due to tumor growth and angiogenesis over 31 hours, or slight changes in the US and PA system setup and positioning of the mouse.

The spectroscopic PA imaging analysis shows the Hb, HbO_2, and NP contributions to the PA signal. As expected, significant increase of NP concentration in the tissue was observed by comparing the C[NP] images before and after NP injection (Figure 5.5(f) and Figure 5.5(l), respectively). Clearly, plenty of NPs injected through tail vein accumulate at the tumor region. Moreover, Hb concentration is shown in tail vein area (Figure 5.5(k)) which indirectly proves the validity of the developed spectroscopic PA image reconstruction algorithm. In addition, using Eq. (9) and estimates of C[Hb] and C[HbO_2], oxygen saturation (SO_2) of the blood can also be calculated (Figure 5.5(c) and Figure 5.5(i)).

Four cross-sections of tumor, indicated by dotted lines in the photograph of the mouse (Figure 5.6(a)), were analyzed for correlation between PA-derived images and histological slides. Overall, the distribution of NPs in C[NP] images (Figure 5.6(b)) and silver stain in histological slides (Figure 5.6(c)) is well correlated. For example, the first and second cross-sections of the tumor have much fewer NPs than cross-sections 3 and 4 – both C[NP] images and silver stained slides indicate the same trend. The enlarged regions of silver stained slides (Figure 5.6(d) and Figure 5.6(e)) clearly show NP accumulation at the tumor.

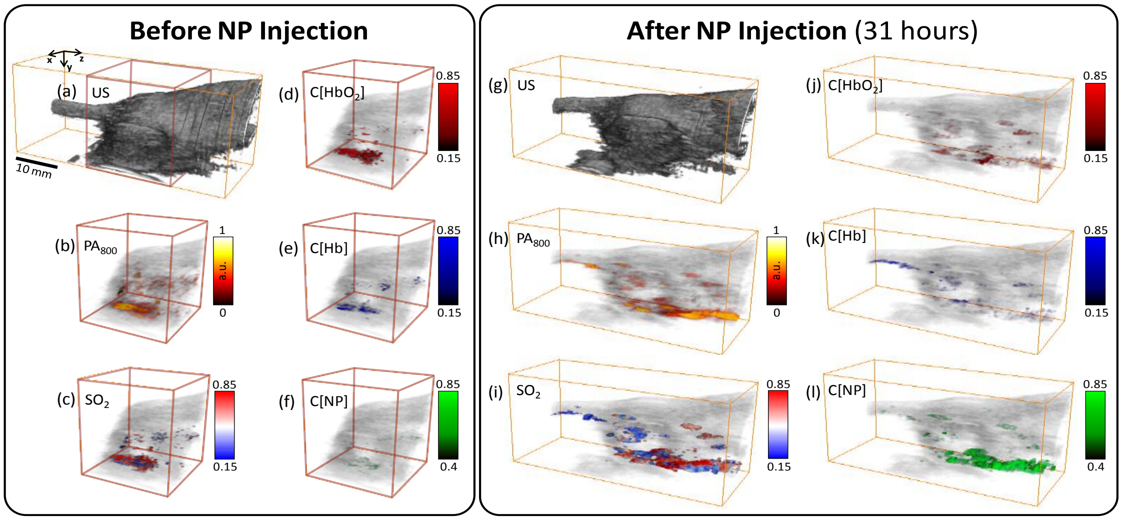

Figure 5.5: Three-dimensional ultrasound images (panels a,g), photoacoustic images (panels b,h), and PA-derived oxygen saturation images (SO_2, panels c,i), and images of oxyhemoglobin ($C[HbO_2]$, panels d,j), deoxyhemoglobin (C[Hb], panels e,k), and nanoparticle (C[NP], panels f,l) concentration before and 31 hours after tail vein injection of PEGylated gold nanorods into tumor bearing mouse. PA and PA-derived images are shown with ultrasound images in the background. Oxygen saturation was calculated using the concentrations of oxyhemoglobin and deoxyhemoglobin. Furthermore, anatomical features of the tumor (i.e., tumor size and location) are better shown in rotating 3-D images: ultrasound (panel g), 3-D photoacoustics (panel h), oxygen saturation (panel i), and nanoparticle concentration (panel l).

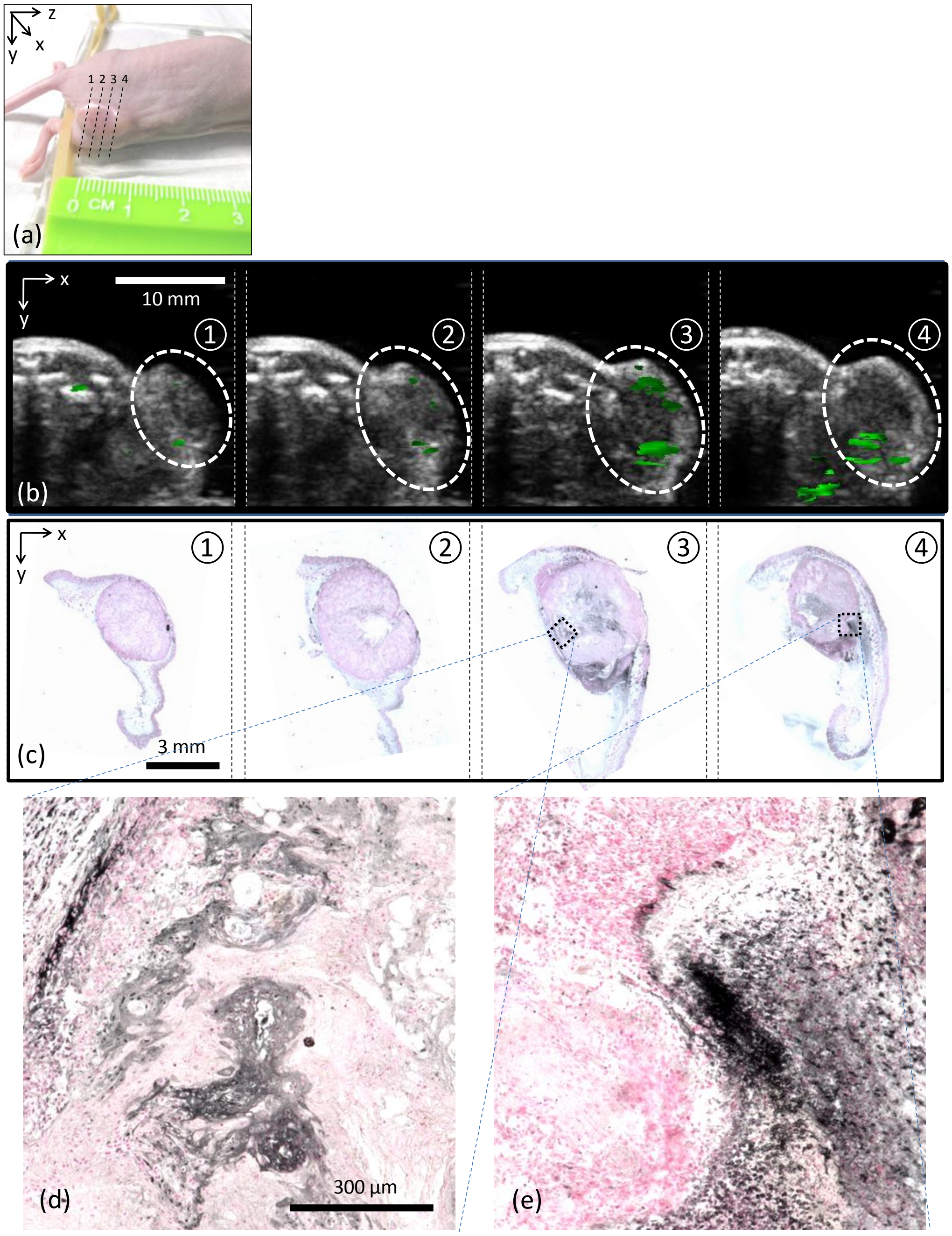

Figure 5.6: (a) Photograph of the mouse with dotted lines indicating the approximate location of imaging planes and corresponding histological slides. (b) PA-derived maps of NP concentration displayed over the ultrasound images of the tumor. (c) Silver stained tissue slides where gray to black colors indicate presence of NPs. The enlarged areas of silver stained slides are shown in panels (d) and (e).

5.4. DISCUSSION

Spectroscopic PA imaging algorithm incorporating depth- and wavelength-dependent fluence compensation and hybrid LLS/MMSE analysis (Figure. 5.3) was developed and demonstrated using 3-D US and PA *in vivo* imaging (Figure. 5.2) of tumor bearing mouse injected with PEGylated gold nanorods (Figure. 5.1). The results of spectroscopic PA imaging were verified using silver staining of the excised tumor tissue.

Before NP injection, spectroscopic PA imaging should detect no NPs. However, very small concentrations of NPs in a few locations were observed in image before the injection of NPs (Figure 5.5(f)). Several factors may have an influence here. For example, it was assumed that PA signal is due to three types of optical absorbers: HbO_2, Hb, and NPs. However, other absorbers may also be present resulting in some false positive. Noise in the measurements (or low signal-to-noise ratio of PA signal) can also result in incorrect analysis of optical absorbers contributing to PA signal. In addition, imperfect fluence compensations can cause spectral mismatch between the compared and reconstructed spectra.

The depth- and wavelength-dependent fluence compensation of PA signal can be further improved. In this work, I could not fully compensate wavelength-dependent local fluence changes due to the lack of information about optical properties of mouse tumor at different wavelengths. For more accurate fluence-dependent PA compensation, optical properties of various tissues at different wavelengths, measured independently and summarized to a look-up table, may be used. In addition, more sophisticated models, such as a 2-D or even a 3-D multi-layer model with incident beam specifications (e.g., beam diameter and intensity profile, incident angle, etc), can improve local fluence estimation using a Monte Carlo simulation [22, 23].

The developed spectroscopic PA imaging system and algorithms can identify NP delivery *in vivo.* The NPs that I used in the current studies were not specifically targeted to cancer cells. Therefore, the main mechanism of delivery was the enhanced permeability and retention (EPR) effect. However, the approach presented here can be applied to monitor the delivery of NPs and the temporal and spatial interactions of molecular specific targeted NP with tissue [24, 25].

5.5. CONCLUSION

I have developed a more robust and less noise-sensitive spectroscopic PA imaging algorithm based on minimum mean square error (MMSE). The 3-D US and PA imaging system and developed algorithm were used for monitoring the delivery and accumulation of PEGylated gold nanorods which were intravenously injected into the mouse bearing a subcutaneous tumor. After the injection, spatial distribution of NPs within the tumor was successfully imaged using the US and PA imaging system and MMSE algorithm. Furthermore, NPs were reliably distinguished from the blood. Moreover, silver staining of tissue slices confirmed deposition of NPs in the tumor. Good correlation of NP distribution between histological slides and spectroscopic PA images was also demonstrated. The results of this study suggest that spectroscopic PA imaging can be used for monitoring the delivery and spatial distribution of plasmonic NPs *in vivo*.

REFERENCES

[1] S. Mallidi, T. Larson, J. Tam, P. P. Joshi, A. Karpiouk, K. Sokolov, and S. Emelianov, "Multiwavelength photoacoustic imaging and plasmon resonance coupling of gold nanoparticles for selective detection of cancer," Nano Lett 9, 2825-2831 (2009).

[2] P. C. Li, C. R. Wang, D. B. Shieh, C. W. Wei, C. K. Liao, C. Poe, S. Jhan, A. A. Ding, and Y. N. Wu, "In vivo photoacoustic molecular imaging with simultaneous multiple selective targeting using antibody-conjugated gold nanorods," Opt Express 16, 18605-18615 (2008).

[3] C. L. Bayer, Y. S. Chen, S. Kim, S. Mallidi, K. Sokolov, and S. Emelianov, "Multiplex photoacoustic molecular imaging using targeted silica-coated gold nanorods," Biomed Opt Express 2, 1828-1835 (2011).

[4] K. Homan, S. Kim, Y. S. Chen, B. Wang, S. Mallidi, and S. Emelianov, "Prospects of molecular photoacoustic imaging at 1064 nm wavelength," Opt Lett 35, 2663-2665 (2010).

[5] X. Huang, P. K. Jain, I. H. El-Sayed, and M. A. El-Sayed, "Plasmonic photothermal therapy (PPTT) using gold nanoparticles," Lasers Med Sci 23, 217-228 (2008).

[6] Y. S. Chen, W. Frey, S. Kim, K. Homan, P. Kruizinga, K. Sokolov, and S. Emelianov, "Enhanced thermal stability of silica-coated gold nanorods for photoacoustic imaging and image-guided therapy," Opt Express 18, 8867-8878 (2010).

[7] Y. S. Chen, W. Frey, S. Kim, P. Kruizinga, K. Homan, and S. Emelianov, "Silica-coated gold nanorods as photoacoustic signal nanoamplifiers," Nano Lett 11, 348-354 (2011).

[8] R. Shukla, V. Bansal, M. Chaudhary, A. Basu, R. R. Bhonde, and M. Sastry, "Biocompatibility of gold nanoparticles and their endocytotic fate inside the cellular compartment: a microscopic overview," Langmuir 21, 10644-10654 (2005).

[9] S. Kim, Y.-S. Chen, G. P. Luke, M. Mehrmohammadi, J. R. Cook, and S. Y. Emelianov, "Ultrasound and photoacoustic image-guided photothermal therapy using silica-coated gold nanorods: in-vivo study," in Proceedings of IEEE Conference on Ultrasonics, Ferroelectrics and Frequency Control, 233-236 (2010).

[10] J. Shah, S. Park, S. Aglyamov, T. Larson, L. Ma, K. Sokolov, K. Johnston, T. Milner, and S. Y. Emelianov, "Photoacoustic imaging and temperature measurement for photothermal cancer therapy," J Biomed Opt 13, 034024 (2008).

[11] X. Yang, S. E. Skrabalak, Z. Y. Li, Y. Xia, and L. V. Wang, "Photoacoustic tomography of a rat cerebral cortex in vivo with au nanocages as an optical contrast agent," Nano Lett 7, 3798-3802 (2007).

[12] M.-L. Li, J.-T. Oh, X. Xie, G. Ku, W. Wang, C. Li, G. Lungu, G. Stoica, and L. V. Wang, "Simultaneous molecular and hypoxia imaging of brain tumors in vivo using spectroscopic photoacoustic tomography," Proceedings of the IEEE 96, 481-489 (2008).

[13] B. Wang, J. L. Su, J. Amirian, S. H. Litovsky, R. Smalling, and S. Emelianov, "Detection of lipid in atherosclerotic vessels using ultrasound-guided spectroscopic intravascular photoacoustic imaging," Opt Express 18, 4889-4897 (2010).

[14] K. H. Song, C. Kim, K. Maslov, and L. V. Wang, "Noninvasive in vivo spectroscopic nanorod-contrast photoacoustic mapping of sentinel lymph nodes," Eur J Radiol 70, 227-231 (2009).

[15] W. J. Akers, C. Kim, M. Berezin, K. Guo, R. Fuhrhop, G. M. Lanza, G. M. Fischer, E. Daltrozzo, A. Zumbusch, X. Cai, L. V. Wang, and S. Achilefu, "Noninvasive photoacoustic and fluorescence sentinel lymph node identification using dye-loaded perfluorocarbon nanoparticles," ACS Nano 5, 173-182 (2011).

[16] B. Nikoobakht and M. A. El-Sayed, "Preparation and growth mechanism of gold nanorods (NRs) using seed-mediated growth method," Chem. Mater 15, 1957-1962 (2003).

[17] S. A. Prahl, "Optical properties spectra compiled by Scott Prahl," (retrieved 2009) http://omlc.ogi.edu/spectra/.

[18] A. N. S. Institute, "American National Standard for the Safe Use of Lasers " ANSI Z136.1-2000, New York (2000).

[19] R. A. Mucci, "A comparison of efficient beamforming algorithms," IEEE Trans. Acoust. Speech. Signal Proc. 32, 548-558 (1984).

[20] A. A. Oraevsky, S. L. Jacques, and F. K. Tittel, "Measurement of tissue optical properties by time-resolved detection of laser-induced transient stress," Appl Opt 36, 402-415 (1997).

[21] W.-F. Cheong, S. A. Prahl, and A. J. Welch, "A review of the optical properties of biological tissues," IEEE Quantum Electronics 26, 2166-2185 (1993), updated by W.-F. Cheong, further additions by L.V. Wang and S.L. Jacques, http://omlc.ogi.edu/pubs/pdf/cheong90a.pdf

[22] L. Wang, S. L. Jacques, and L. Zheng, "MCML--Monte Carlo modeling of light transport in multi-layered tissues," Comput Methods Programs Biomed 47, 131-146 (1995).

[23] L. Wang, S. L. Jacques, and L. Zheng, "CONV--convolution for responses to a finite diameter photon beam incident on multi-layered tissues," Comput Methods Programs Biomed 54, 141-150 (1997).

[24] S. Mallidi, T. Larson, J. Aaron, K. Sokolov, and S. Emelianov, "Molecular specific optoacoustic imaging with plasmonic nanoparticles," Opt Express 15, 6583-6588 (2007).

[25] B. Wang, E. Yantsen, T. Larson, A. B. Karpiouk, S. Sethuraman, J. L. Su, K. Sokolov, and S. Y. Emelianov, "Plasmonic intravascular photoacoustic imaging for detection of macrophages in atherosclerotic plaques," Nano Lett 9, 2212-2217 (2009).

Chapter 6: *Ultrasound and Photoacoustic Image-guided Photothermal Therapy using Silica-coated Gold Nanorods: In-vivo Study*

The results of this study have been published on *Proceedings of IEEE International Ultrasonnics Symposium* in 2010, and will be submitted for the journal publication.

ABSTRACT

In nanoparticle mediated photothermal therapy, confirmation of nanoparticle delivery/deposition in a tumor before therapy and temperature monitoring during therapy are needed to optimize therapeutic outcomes. In this chapter, I demonstrate that ultrasound and photoacoustic imaging techniques can plan and guide photothermal cancer therapy, using an *in-vivo* mouse model of subcutaneous cancer intravenously administrated with silica-coated gold nanorods.

6.1 INTRODUCTION

Photothermal therapy is a non-invasive or minimally invasive cancer treatment method that utilizes light energy to produce heat energy to induce cancer cell death [1]. Metallic, such as gold or silver, nanoparticles have been shown to effectively enhance photothermal therapy because of their high optical absorption. Absorption peaks in the desired optical spectral range can be controlled with geometry or composition of nanoparticles. In addition, nanoparticles can be bio-conjugated to target to cancer cells. For nanoparticle mediated photothermal therapy, nanoparticles are introduced to tumors by intravenous injection. The nanoparticles are circulated through the blood stream, and delivered to the tumor site by several mechanisms, such as the enhanced permeability and retention (EPR) effect and specific targeting to the cancer cells based on cell proliferation or angiogenesis [2]. After the nanoparticles have accumulated in the tumor, a continuous wave (CW) laser (with wavelength matched to the absorption peak of the injected nanoparticles) is used for thermal therapy. However, to optimize therapeutic outcomes (i.e. maximize cancer tissue damage and minimize healthy tissue damage), the nanoparticle delivery and distribution need to be confirmed before therapy, and temperature must be monitored during therapy.

Spectroscopic photoacoustic imaging can be used to differentiate nanoparticles from biological tissue components such as oxygenated and deoxygenated hemoglobin [3]. This technique is based on the unique wavelength-dependent optical absorption properties of each tissue component. Since the photoacoustic signal amplitude can be correlated with the highly tissue-dependent optical absorption coefficient, it is possible to analyze the distribution of tissue components. Therefore, spectroscopic photoacoustic imaging can be used for the confirmation of nanoparticle deposition in the tumor before therapy.

Photoacoustic-based thermal imaging can be used to estimate temperature distribution during photothermal therapy [4]. Because photoacoustic pressure is the function of temperature, it is possible to correlate photoacoustic signal amplitude changes with temperature changes. This non-invasive and real-time two-dimensional (2-D) temperature distribution imaging method can provide enough information to optimize therapeutic outcomes.

In this chapter, I demonstrate ultrasound and photoacoustic image-guided photothermal therapy using an *in-vivo* mouse model of cancer. Spectroscopic photoacoustic imaging was used to monitor nanoparticle delivery. Then, photoacoustic-based thermal imaging was used to monitor temperature during therapy.

6.2 MATERIALS AND METHODS

6.2.1 *In-vivo* Mouse Model of Cancer

A three month old immunodeficient nude mouse (Nu/Nu) was used for this study. A431 human cancer cells were inoculated in the right flank of the mouse. The injected cells were grown for 20 days to lead to a tumor size of about 10 mm in diameter.

6.2.2 Silica-coated Gold Nanorods

Silica-coated gold nanorods were used due to their enhanced thermal stability [5] and enhanced photoacoustic signal response [6]. The silica-coated gold nanorods were produced from CTAB-stabilized gold nanorods by exchanging CTAB with the biocompatible mPEG-thiol, and then using the mPEG polymer as a silane coupling agent for silica coating. The absorption peak of the nanorods was about 800 nm. The injected volume of nanoparticle solution was 200 μL, and the injected mass of gold was 0.4 mg. The nanoparticles were intravenously injected to the mouse through the tail vein.

6.2.3 Mouse Imaging Setup and Data Acquisition

The three dimensional (3-D) ultrasound and photoacoustic imaging setup for *in-vivo* mouse experiment is shown in Figure 6.1. An OPO tunable laser (Spectra-Physics, USA) produced 5 ns pulsed laser in wavelength range of 400 to 2300 nm operated at 10 Hz. For this study, I used 8 wavelengths ranging from 740 to 840 nm in 20 nm increments. The average laser fluence at the surface of mouse skin was approximately 16 mJ/cm^2 satisfying American National Standard Institute (ANSI) limit (~30 mJ/cm^2 for the wavelengths I applied). The pulsed laser was delivered to the tumor through an optical window attached to one side of a water tank. The water tank was used to couple the acoustic waves between the array transducer (LA12/128, Vermon, France) and the mouse, and to regulate the mouse body temperature. Water temperature was kept at 37°C during the experiment with a water circulation system (Isotemp 3013H, Fisher). In order to keep both the transducer-cable connection and the head of the mouse above the water, a mouse bed tilted to 45° was made. The bed was connected to 1-D motorized system (National Instruments, USA) to scan a 3-D volume of the mouse. A Sonix RP ultrasound system (Ultrasonix Medical Corporation, Canada) was used to collect ultrasound radiofrequency (RF) beamformed data, sampled at 40 MHz. A WP32 system (Winprobe Corporation, USA) was used to collect 32 parallel photoacoustic RF channel data. 32 frames of the collected photoacoustic channel data were averaged to enhance signal-to-noise ratio (SNR). For photothermal therapy, a CW laser (Power Technology Inc., 808 nm, 1 W) was used.

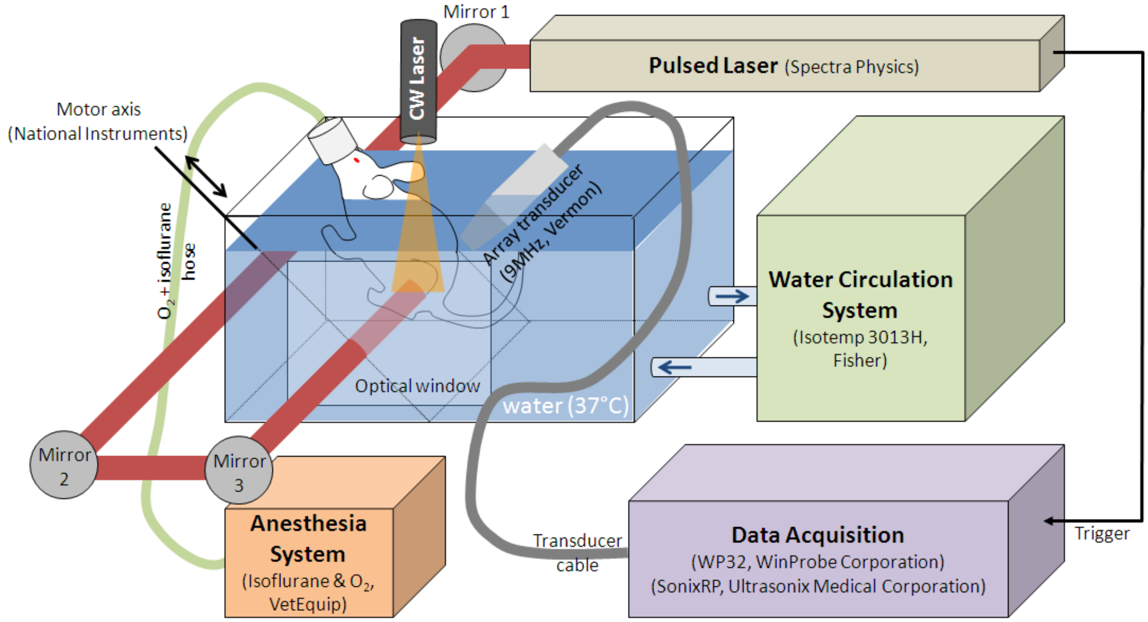

Figure 6.1: Block diagram of mouse imaging setup

6.2.4 Spectroscopic Photoacoustic Imaging

Assuming both the stress and the thermal confinements are satisfied, the photoacoustic maximum pressure, p_0, at the pressure source can be expressed by:

$$p_0 = \Gamma \mu_a F \, , \tag{6.1}$$

$$\Gamma = \frac{\beta v_s^2}{C_p} \, , \tag{6.2}$$

where Γ is Grüneisen parameter, μ_a is the absorption coefficient of the medium, and F is the laser fluence. The Grüneisen parameter, Γ, is defined by the volume expansion coefficient, β, the speed of sound, v_s, and the heat capacity at constant pressure, C_p.

By keeping temperature constant, the Grüneisen parameter at the same position (i.e., same type of tissue) can be assumed as a constant value. In addition, by compensating for the fluence at different wavelengths, multi-wavelength photoacoustic pressures can be correlated with the optical absorption coefficient of the various types of tissue as well as the injected nanoparticles.

Since there are three major components (i.e., oxygenated hemoglobin, deoxygenated hemoglobin, and nanoparticles) which dominantly absorb the light energy (i.e., produce photoacoustic signal) in the wavelength range of 740 to 840 nm, the following spectrum was compared with the photoacoustic spectrum in a 500 µm by 500 µm by 500 µm volume.

$$\mu_a = C_{HbO_2}\mu_{HbO_2} + C_{Hb}\mu_{Hb} + C_{NP}\mu_{NP} \, , \tag{6.3}$$

where μ_{HbO2}, μ_{Hb}, and μ_{NP} are the normalized absorption spectra of oxygenated and deoxygenated hemoglobin, and nanoparticles. C_{HbO2}, C_{Hb}, and C_{NP} are the relative concentrations of oxygenated and deoxygenated hemoglobin, and nanoparticles within the volume, and the total relative concentration was 1 (i.e., $C_{HbO2}+C_{Hb}+C_{NP}=1$). C_{HbO2}, C_{Hb}, and C_{NP} were determined by minimizing the mean square error of Equation (6.2).

The minimum mean square error (MMSE) of 0.01 (i.e., 1% of maximum possible error) was used for the threshold of displaying each components.

6.2.5 Photoacoustic-based Thermal Imaging

Photoacoustic imaging can be used to monitor the temperature distribution in tissues noninvasively. Photoacoustic signal intensity is directly dependent on the dimensionless Grüneisen coefficient. The volume expansion coefficient and the speed of sound are both temperature dependent and linearly proportional to the temperature for water-based and fatty tissues between 10 and 55°C [7, 8] Therefore, the amplitude of photoacoustic signal can be used to estimate tissue temperature. The temperature rise, ΔT, can be estimated by

$$\Delta T = a\frac{\Delta P}{P} = a\frac{\Delta\Gamma}{\Gamma}, \tag{6.4}$$

where a is the tissue-dependent constant that can be experimentally determined, ΔP is the pressure rise when the temperature rises by ΔT, and $\Delta\Gamma$ is the corresponding change in the Grüneisen parameter.

6.3 RESULTS AND DISCUSSION

6.3.1 Monitoring of Nanoparticle Delivery Before Therapy

The mouse was imaged at two different time points: before the injection (as a control) and after the injection (63 hours after the nanoparticle injection). The 3-D ultrasound image shows anatomical information of the tumor (i.e., location and size). The obtained photoacoustic images before nanoparticle injection show intrinsic optical absorption contrast which is mainly produced by blood. However, the photoacoustics image obtained after administrating nanoparticles have signals from not only blood, but also nanoparticles. A single-wavelength photoacoustic image cannot differentiate nanoparticles from blood. However, the outcome of spectroscopic photoacoustic imaging clearly shows separated oxygenated and deoxygenated blood, and nanoparticles which are color-coded with red, blue, and yellow, respectively. All three components were displayed from 50% to 100% of relative concentration (Figure 6.2).

Since spectroscopic photoacoustic imaging is based on spectral analysis of photoacoustic signals, the mouse position in relative to the imaging setup can be varied from one time point to the other. Moreover, this technique resolved no nanoparticle deposition at the tumor before the injection. The control experiment result indirectly shows this technique can be reliably used for monitoring nanoparticle delivery. The non-invasiveness of this technique will provide answers of many research questions related to nanoparticle delivery, such as comparison of delivery efficacy between non-targeted (i.e., PEGylated) and targeted (i.e., bio-conjugated) nanoparticles.

6.3.2 Monitoring of Temperature Rise During Therapy

At 63 hours after nanoparticle injection, photothermal therapy was performed for 5 minutes using CW laser wavelength of 808 nm. During therapy, photoacoustic signals at pulsed laser wavelength of 800 nm were collected at every 30 seconds. White arrows in Figure 6.3 indicate the direction of CW laser irradiation. The CW laser beam spot size on the skin of mouse was 0.8 mm in diameter. Based on Equation (6.3), a temperature distribution was estimated. The tissue-dependent constant, a, was 4.6667 which was experimentally acquired from porcine muscle tissue [4]

A maximum temperature rise of 19°C during therapy was observed by photoacoustic-based thermal imaging. During the first 2.5 minutes, mouse tumor temperature gradually increased, and then the temperature was relatively constant until the CW laser was turned off (i.e., 5 minutes). Since the mouse body temperature was precisely controlled by water circulation system, it was assumed that the initial temperature in the tumor was 37°C. During therapy, the temperature was increased to 56°C which was enough temperature to thermally damage the cancer cells. Moreover, the region of increasing temperature was well correlated with the region of nanoparticle accumulation (Figure 6.4). This result shows that nanoparticles are the heat source, not the tissue. Therefore, nanoparticles are crucial factor for efficient and effective photothermal therapy.

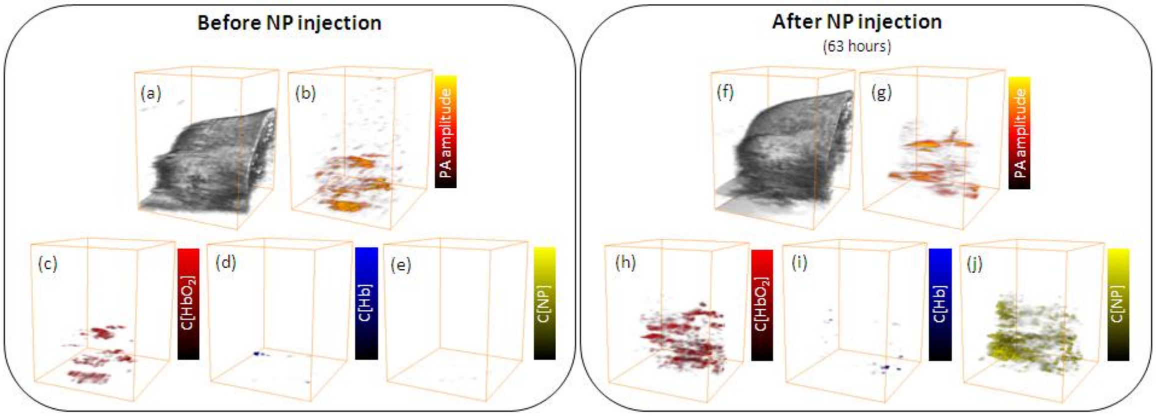

Figure 6.2: 3-D ultrasound, photoacoustic, and spectroscopic photoacoustic images of before nanoparticle injection (a~e), and after the injection (f~j). (a) and (f) (ultrasound images) show tumor size and location. (b) and (g) are photoacoustic images obtained at wavelength of 800 nm. (c) and (h), (d) and (i), and (e) and (j) show oxygenated hemoglobin, deoxygenated hemoglobin, and nanoparticle distributions, respectively. Color bars for spectroscopic photoacoustic images (red, blue, and yellow) represent 50% to 100% of relative concentrations of oxygenated hemoglobin, deoxygenated hemoglobin, and nanoparticles, respectively. The field of view (FOV) for each volume is 22.4 mm (width) by 25.8 mm (depth) by 20.0 mm (length).

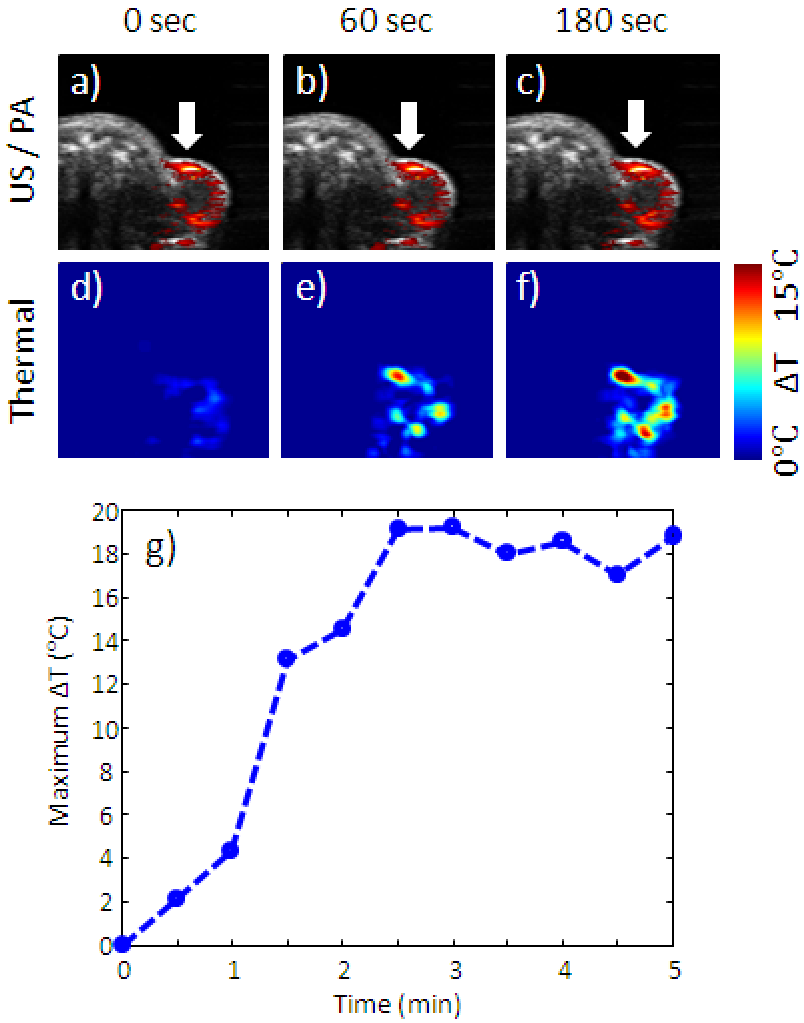

Figure 6.3: Combined ultrasound and photoacoustic images, and photoacoustic-based thermal images are shown in (a~c) and (d~f), respectively. The white arrow represents the direction of CW laser irradiation (808 nm, 1 W). (d) Photothermal therapy of 5 minutes result in maximum temperature rise of about 19°C in the tumor.

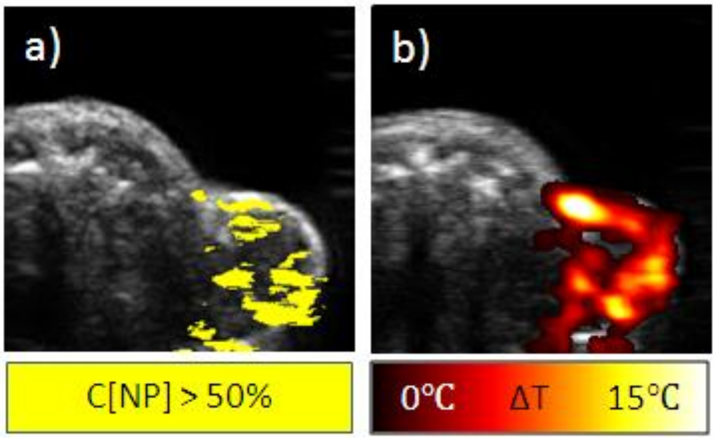

Figure 6.4: (a) Nanoparticle distribution obtained from spectroscopic photoacoustic imaging and (b) temperature distribution after 3 minutes of therapy obtained from photoacoustic-based thermal imaging. Both nanoparticle and temperature distribution are closely related to each other.

6.4 CONCLUSION

Ultrasound and photoacoustic imaging techniques such as 3-D ultrasound imaging, 3-D spectroscopic photoacoustic imaging, and 2-D photoacoustic-based thermal imaging can be used for photothermal cancer therapy. 3-D ultrasound imaging provides much better anatomical information (i.e., spatial position and size of the tumor) when compared to 2-D conventional ultrasound images. 3-D spectroscopic photoacoustic imaging gives much better functional information, such as blood and nanoparticle distributions in 3-D when compared to 2-D spectroscopic photoacoustic imaging or 3-D single-wavelength photoacoustic imaging. 2-D photoacoustic-based thermal imaging offers temperature distribution during therapy. All these imaging techniques were developed and optimized for the mouse imaging, and used to demonstrate image-guided photothermal therapy using an *in-vivo* mouse model of cancer. Silica-coated gold nanorods were used due for their thermal stability and enhanced photoacoustic response.

Although I did not have any histological analysis of the tumor yet, several indicators from the results of this study show that spectroscopic photoacoustic imaging can be used for monitoring of nanoparticle delivery, and nanoparticle delivery is very important factor in photothermal therapy. The control experiment (before-injection imaging) does not show any nanoparticle deposition (Figure 6.2-e) while after-injection imaging shows plenty of nanoparticle deposition in the tumor (Figure 6.2-j). Also, very similar distribution between nanoparticles and temperature (Figure 6.4) gives us more motivation of using bio-conjugated nanoparticles for molecular specific therapy.

REFERENCES

[1] X. Huang, I. H. El-Sayed, W. Qian, and M. A. El-Sayed, "Cancer cell imaging and photothermal therapy in the near-infrared region by using gold nanorods," J Am Chem Soc, vol. 128, pp. 2115-20, 2006.

[2] J. D. Byrne, T. Betancourt, and L. Brannon-Peppas, "Active targeting schemes for nanoparticle systems in cancer therapeutics," Adv Drug Deliv Rev, vol. 60, pp. 1615-26, 2008.

[3] C. Kim, E. C. Cho, J. Chen, K. H. Song, L. Au, C. Favazza, Q. Zhang, C. M. Cobley, F. Gao, Y. Xia, and L. V. Wang, "In vivo molecular photoacoustic tomography of melanomas targeted by bioconjugated gold nanocages," ACS Nano, vol. 4, pp. 4559-64.

[4] J. Shah, S. Park, S. Aglyamov, T. Larson, L. Ma, K. Sokolov, K. Johnston, T. Milner, and S. Y. Emelianov, "Photoacoustic imaging and temperature measurement for photothermal cancer therapy," J Biomed Opt, vol. 13, pp. 034024, 2008.

[5] Y. S. Chen, W. Frey, S. Kim, K. Homan, P. Kruizinga, K. Sokolov, and S. Emelianov, "Enhanced thermal stability of silica-coated gold nanorods for photoacoustic imaging and image-guided therapy," Opt Express, vol. 18, pp. 8867-78.

[6] Y.-S. Chen, P. Kruizinga, P. P. Joshi, S. Kim, K. Homan, K. Sokolov, W. Frey, and S. Emelianov, "On stability of molecular therapeutic agents for noninvasive photoacoustic and ultrasound image-guided photothermal therapy," Proc. SPIE, pp. 7564, 2010.

[7] F. A. Duck, "Physical properties of tissue," Academic, 1990.

[8] J. C. Bamber and C. R. Hill, "Ultrasonic attenuation and propagation speed in mammalian tissues as a function of temperature," Ultrasound Med Biol, vol. 5, pp. 149-57, 1979.

Chapter 7: *Conclusions and Future Work*

7.1 SUMMARY

Ultrasound and photoacoustic imaging techniques were investigated and further developed to detect cancer and to guide photothermal cancer therapy. Before really focusing on cancer-related studies (i.e., cancer detection and therapy guidance), ultrasound image reconstruction methods were investigated and a new ultrasound beamforming method which combines synthetic aperture focusing [1] and display pixel-based focusing [2] techniques was developed. Although the specific application for the developed method in this dissertation was intravascular ultrasound (IVUS) imaging, the same concept and idea can be applied to any general ultrasound and photoacoustic imaging in which the same improvement of image qualities is expected (Chapter 2). The improved image qualities are essential for any applications using ultrasound and photoacoustic imaging. Therefore, better cancer detection using ultrasound elasticity imaging and better photothermal cancer therapy guidance using ultrasound and photoacoustic imaging are expected by using the developed beamforming technique.

The main research topics (i.e., cancer detection and therapy guidance) were presented in Chapter 3 to 6. Chapter 3 and 4 were about cancer detection using ultrasound elasticity imaging, and Chapter 5 and 6 were about photothermal cancer therapy guided by ultrasound and photoacoustic imaging.

In ultrasound elasticity imaging, first of all, displacement estimation algorithms were investigated and then the new estimation method for both enhanced sub-pixel displacement estimation performance and lowered computational complexity was developed (Chapter 3). The main idea of the developed method is to use autocorrelation output for compensating cross-correlation output. The autocorrelation output is supposed to be zero, however it is not because of sub-pixel estimator's error related with ultrasound speckle statistics. Therefore, overall displacement estimation results can be more accurate by subtracting autocorrelation output from cross-correlation output. Moreover, the developed algorithm was able to be implemented in only one FPGA (field programmable gate array) since it lowered computational costs compared to other estimation methods which generate almost the same quality of outputs. As a result, the WP64 system (Winprobe Corporation, FL, USA) has implemented the developed algorithm in a Xilinx FPGA (XC4VSX55). The developed algorithm was also utilized to evaluate ultrasound elasticity imaging for prostate cancer detection (Chapter 4). This initial clinical study was performed at the University of Texas M.D. Anderson Cancer Center in Houston. Total 13 patients who had prostate cancer underwent prostatectomy surgery. Before the surgery, elasticity imaging exams were performed and analyzed. Then the results of elasticity imaging were compared with pathological analysis. The results of this study suggested that elasticity imaging can be a promising tool for prostate cancer detection since high correlation between elasticity imaging and pathological analysis was found.

Once cancer is diagnosed, photothermal therapy can be performed to thermally treat cancer. In order to maximize photothermal therapeutic outcomes, nanoparticles can be utilized because of their high optical absorption properties. The nanoparticles can generate more heat energy caused by continuous laser than biological tissue. In this photothermal therapy procedure, nanoparticle delivery needs to be monitored to confirm the nanoparticle deposition at the tumor before therapy. During therapy, temperature changes also need to be monitored to optimize therapeutic results (i.e., maximize cancer tissue damage and minimize normal tissue damage).

Spectroscopic photoacoustic imaging can detect nanoparticles in tissue using optical absorption spectra of each component such as oxy-blood, deoxy-blood, and nanoparticles. The improved spectroscopic photoacoustic imaging algorithm was developed (Chapter 5) to robustly utilize this technique in *in-vivo* situations (i.e., blood environment and complex tissue structure). The developed algorithm was utilized for *in-vivo* nanoparticle delivery experiment using PEGylated gold nanorods. Spectroscopic images were compared with silver staining histological slides to confirm the nanoparticle deposition. The results of this study showed that spectroscopic photoacoustic imaging can provide a spatial distribution of nanoparticles at the tumor as well as to detect them *in-vivo*.

Chapter 6 demonstrated whole procedure of photothermal therapy guided by ultrasound and photoacoustic imaging techniques using an *in-vivo* mouse. In this study, silica-coated gold nanorods were used for enhanced thermal stability and thus better therapeutic outcomes. It is because that the optical absorption peak of nanoparticles can be shifted due to heat. However, silica coating can protect nanoparticles from changing their shape, and therefore no shift on absorption spectra during continuous laser irradiation (i.e., photothermal therapy) can be achieved. Spectroscopic photoacoustic imaging obtained by the developed algorithm clearly showed nanoparticle deposition at the tumor 63 hours after the nanoparticle injection. In addition to this, photoacoustic-based thermal imaging was performed to estimate temperature distribution at the tumor during therapy. Up to about 19°C temperature increase during 5 minutes photothermal therapy was observed. The results of this study showed that ultrasound and photoacoustic imaging can assist photothermal cancer therapy by monitoring nanoparticle delivery and temperature changes.

7.2 PHYSIOLOGICAL MOTION IN ULTRASOUND-BASED THERMAL IMAGING

Ultrasound imaging can be used for estimating temperature changes based on thermally induced speckle motion. Since an ultrasound imaging system reconstructs ultrasound images based on the fixed speed of sound, speckles in ultrasound images can be moved up or down if temperature is changed because the speed of sound is the function of temperature. Water-based tissue has speckle-up motion as temperature increases while fat-based tissue has speckle-down motion as temperature increases [3].

Since this technique is highly sensitive to physiological motion such as respiratory motion and cardiac cycles, it is highly recommended to gate those physiological motions when the temperature changes are measured. Figure 7.1 shows preliminary results of ultrasound-based temperature estimation. The mouse had a subcutaneous cancer in which nanoparticles were accumulated. A continuous wave laser was irradiated to the tumor for 5 minutes. Green color represents low correlation coefficient area where the estimated temperature is ignored. Respiratory cycle was used to synchronize the imaging system so that no breathing motion between two consecutive frames was expected. During 5-minute photothermal therapy, up to 25°C temperature increase was observed by the ultrasound-based thermal imaging technique.

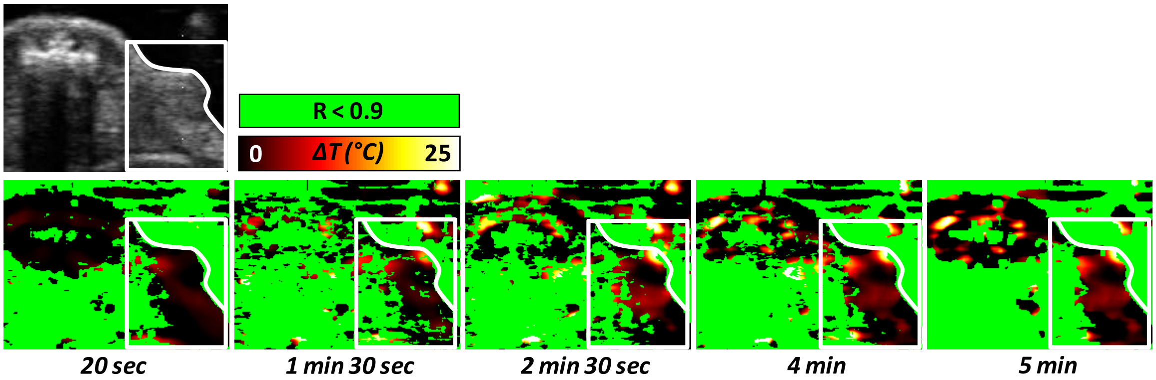

Figure 7.1: Temperature estimation by ultrasound-based thermal imaging.

7.3 OPTICAL ABSORPTION SPECTRA SEPARATION IN SPECTROSCOPIC PHOTOACOUSTIC IMAGING

Spectroscopic photoacoustic imaging relies on optical absorption spectra of each component. In order to have reasonable spectroscopic photoacoustic imaging results, well separated optical absorption spectra of each component is required. Figure 7.2 shows spectroscopic photoacoustic imaging results where oxygenated hemoglobin, deoxygenated hemoglobin, and nanoparticles were resolved. In this study, macrophage cells loaded with nanospheres, of which absorption peak was around 530 nm, was injected. A tumor bearing nude mouse was imaged using 7 wavelengths (i.e., 720, 740, 760, 780, 800, 820, and 840 nm). In the optical window I used, oxy and deoxy blood had a good separation in absorption spectra. The intraclass correlation (ICC) coefficient of -0.801 quantitatively confirmed two absorbers were well separated in their absorption spectra as shown in Figure 7.3. However, the nanoparticles injected to the mouse had very similar absorption spectrum with deoxygenated hemoglobin where the ICC coefficient was 0.781, meaning good agreement between two components. Therefore, it was difficult to separate nanoparticles from deoxygenated hemoglobin by using the spectroscopic photoacoustic imaging technique. As a result, similar distributions between deoxygenated hemoglobin and nanoparticles were observed for all time points (i.e., meaningless results of nanoparticle distribution).

In order to overcome this problem, both optical window for spectroscopic photoacoustic imaging and absorption peak of nanoparticles should be optimized. In chapter 5 and 6, the same optical window and the same imaging system were utilized, but nanoparticles were well detected by using this imaging technique. It was because of nanoparticles absorption peak of around 800 nm (i.e., nanorods). In this case, all three major optical absorber (i.e., oxygenated hemoglobin, deoxygenated hemoglobin, and nanoparticles) in the optical window had well-separated absorption spectra, and therefore the spectroscopic photoacoustic imaging technique can detect nanoparticles from blood.

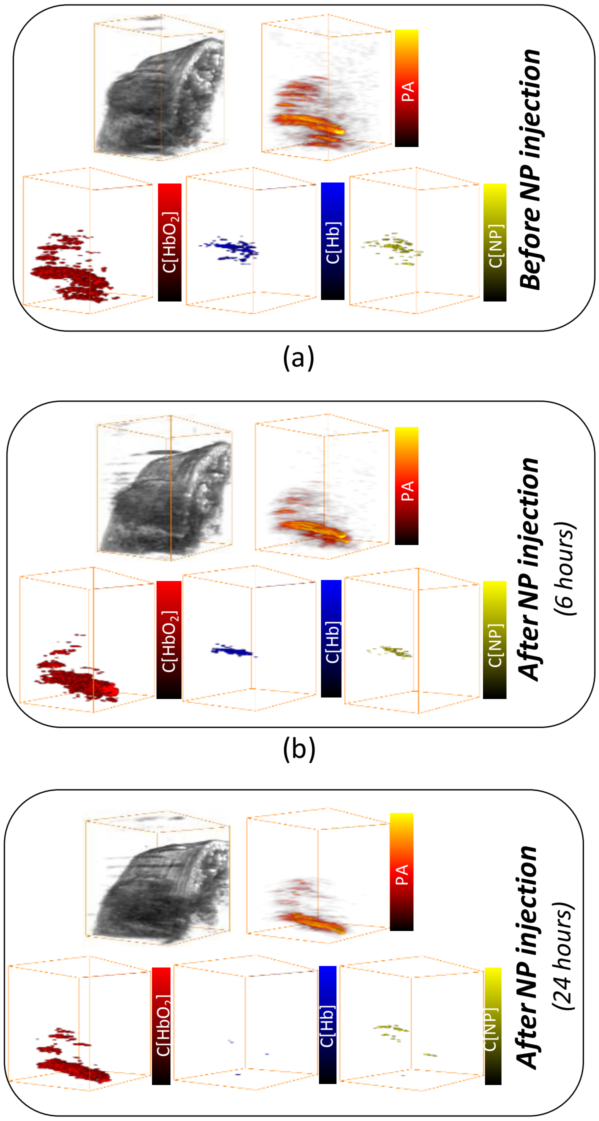

(a)

(b)

(c)

Figure 7.2: Spectroscopic photoacoustic images obtained at (a) before nanoparticle injection, (b) 6 hours and (c) 24 hours after the injection. Macrophage loaded with nanospheres of which absorption peak was around 530 nm was injected

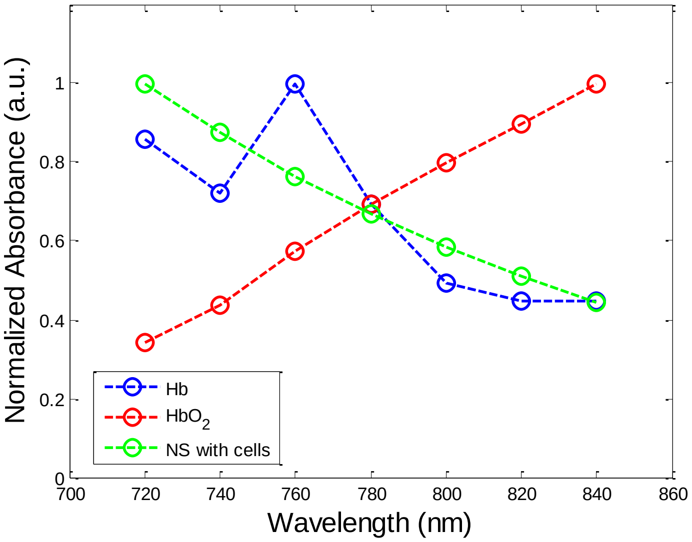

Figure 7.3: Normalized optical absorption specta of oxygenated hemoglobin (red), deoxygenated hemoglobin (blue), and macrophage cells loaded with nanospheres (green).

7.4 3-D PHOTOACOUSTIC BEAMFORMING

In this dissertation, 3-D photoacoustic imaging was performed using a commercial ultrasound 1-D array element transducer. In order to obtain 3-D volume of photoacoustic images, the transducer was scanned in the elevational direction. Each 2-D cross-section of 3-D volume was separately reconstructed using 2-D beamforming. Then, by stacking all 2-D photoacoustic images, 3-D volume images were obtained.

3-D photoacoustic images can be further improved by 3-D photoacoustic beamforming. Unlike ultrasound imaging, photoacoustic imaging doesn’t require ultrasound transmission through the transducer (i.e., only receive beamforming is needed to form photoacoustic images). Therefore, photoacoustic raw signals collected from a 1-D array transducer at different positions can be synthesized to mimic collecting raw signals from a 2-D array transducer (i.e., synthetic aperture focusing technique [4, 5]).

Figure 7.4 shows 3-D volume of photoaocoustic image obtained by 2-D and 3-D beamforming. The 3-D photoacoustic beamforming enhances elevational resolution (i.e., z direction) because of increasing elevational aperture size [6]. By applying the 3-D synthetic aperture photoacoustic beamforming technique using a 1-D array transducer, better quality of 3-D photoacoustic volume images can be obtained. However, more investigations are required to optimize all the imaging parameters such as 2-D synthetic aperture size, 2-D apodization function, and so on. Especially, acoustic lens, installed on the commercial ultrasound 1-D array transducer for focusing beam in the elevational direction, need to be removed to collect photoacoustic signals from wider angle.

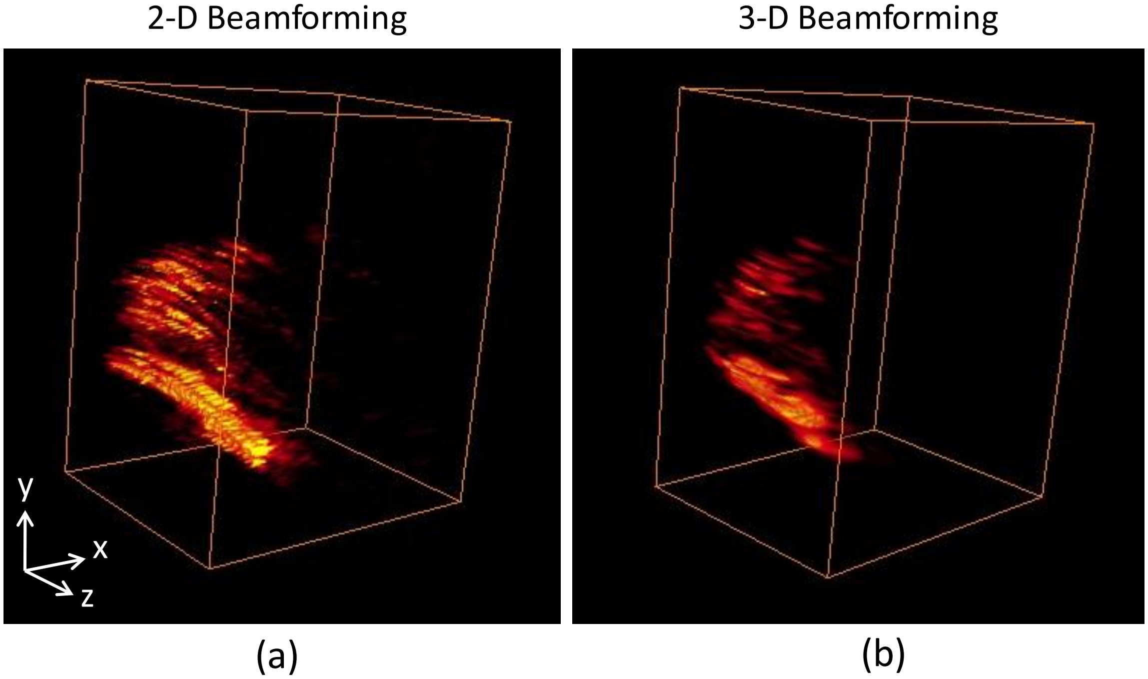

Figure 7.4: 3-D photoacoustic imaging by (a) 2-D beamforming and (b) 3-D beamforming.

7.5 SPECTROSCOPIC PHOTOACOUSTIC IMAGING FOR MONITORING MACROPHAGE CELLS WITH NANOPARTICLES

Spectroscopic photoacoustic imaging can be used for monitoring nanoparticle delievery [7-10]. By using this technique, more researches related to nanoparticles can be performed. Since macrophage cells are over expressed in the most of tumor regions [11], using the macrophage cells to deliver nanoparticles for molecular imaging or photothermal therapy may be beneficial. To evaluate the feasibility of using macrophage cells as nanoparticle carriers, *in-vivo* mouse imaging experiment was performed.

In order to easily separate nanoparticles from blood, nanorods, of which absorption peak was around 680 nm was used. Since macrophage cells selectively load nanoparticles based on their shapes (i.e., spherical shape can be loaded into macrophage cells), I used silica for coating around nanorods to make them spherical shapes. Macrophage cells were incubated with silica-coated nanorods for 18 hours. Then the cells were injected through tail vein of the mouse. Spectroscopic photoacoustic imaging was performed at 4 time points: before injection and 15 hours, 24 housrs, and 48 hours after the injection. Figure 7.5 shows the results of this study. The spectroscopic photoacoustic imaging results show that nanoparticles were started to accumulate at the tumor after the injection. After 48 hours, well recognizable nanoparticle uptake at the bottom of the tumor was observed. However, the verification process needs to be performed to confirm the spectroscopic photoacoustic imaging results.

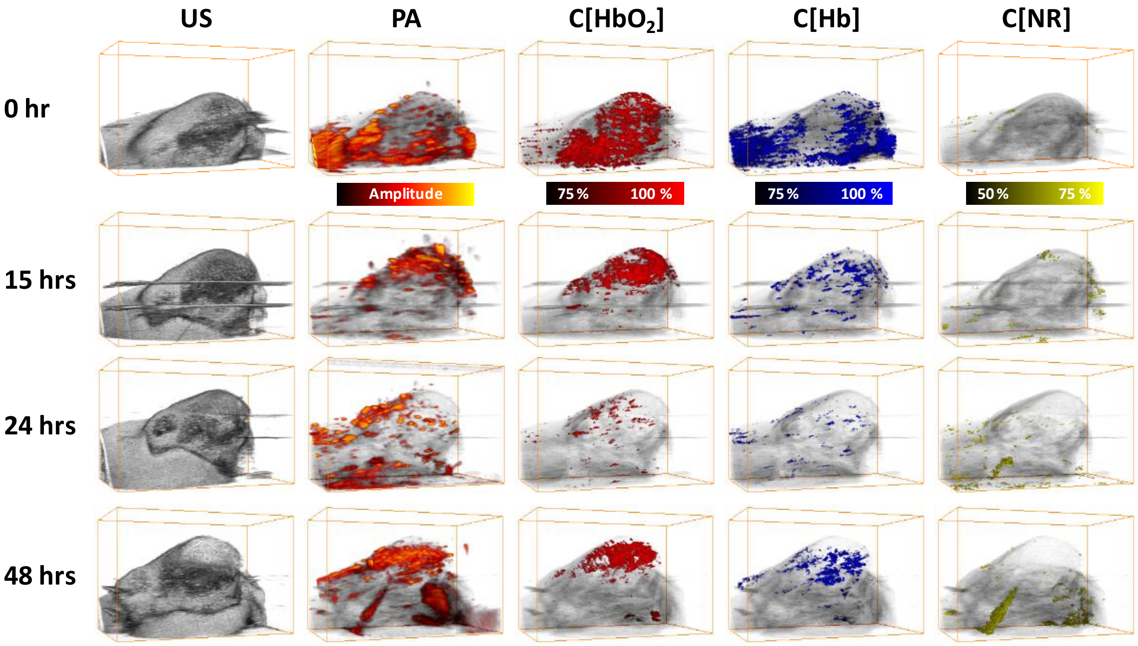

Figure 7.5: Spectroscopic photoacoustic imaging results to evaluate the feasibility of using macrophage cells for delivering nanoparticles.

7.6 ULTRASOUND ELASTICITY IMAGING FOR MONITORING PHOTOTHERMAL THERAPEUTIC OUTCOMES

Ultrasound elasticity imaging is a well-established technique used for the cancer detection and diagnosis. However, the feasibility of using ultrasound elasticity imaging for the assessment of thermal therapy outcomes can be studied. Since the transformation of tissues due to heat may cause changes of mechanical properties in the tissue over time, ultrasound elasticity imaging may help us verify success of cancer therapy.

Figure 7.6 shows preliminary results of using ultrasound elasticity imaging to assess photothermal therapeutic outcomes. A subcutaneous tumor bearing mouse was imaged before and after 5-minute photothermal therapy. The result shows that the stiffness of tumor was changed by thermal therapy. However, more investigations on elastic property changes by photothermal therapy need to be done in order to evaluate this technique for accessing photothermal therapy.

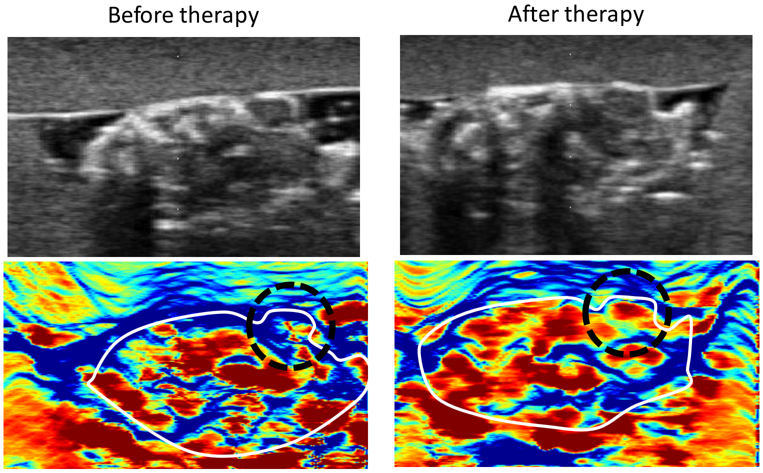

Figure 7.6: Ultrasound elasticity imaging for accessing photothermal therapeutic outcomes. Black dotted line indicates tumor.

7.7 CONCLUSIONS

The studies in this dissertation mainly focused on 3 specific imaging techniques: ultrasound beamforming, ultrasound elasticity imaging, and spectroscopic photoacoustic imaging. All those 3 imaging techniques were utilized for cancer detection and photothermal cancer therapy. By developing the image reconstruction methods (i.e., beamforming), ultrasound and photoacoustic imaging can fundamentally be improved. Therefore, better cancer detection and better therapy guidance is possible. Ultrasound elasticity imaging has been studied for the cost-effective implementation and prostate cancer detection. Finally, spectroscopic photoacoustic imaging algorithm has been developed and the developed algorithm was utilized to demonstrate image-guided photothermal cancer therapy.

The results of these studies suggest that ultrasound and photoacoustic imaging can assist both cancer detection and therapy guidance. Therefore, further development and more improvement of these imaging techniques will be beneficial for better detection of cancer and better guidance of photothermal therapy.

REFERENCES

[1] M. O'Donnell and L. J. Thomas, "Efficient synthetic aperture imaging from a circular aperture with possible application to catheter-based imaging," *IEEE Trans Ultrason Ferroelectr Freq Control*, vol. 39, pp. 366-80, 1992.

[2] J. S. Hwang and T. K. Song, "A study of the display pixel-based focusing method in ultrasound imaging," *Ultrason Imaging*, vol. 23, pp. 1-18, 2001.

[3] J. Shah, S. R. Aglyamov, K. Sokolov, T. E. Milner, and S. Y. Emelianov, "Ultrasound imaging to monitor photothermal therapy - feasibility study," *Opt Express*, vol. 16, pp. 3776-85, 2008.

[4] M. Soumekh, *Synthetic Aperture Radar. Signal Processing with MATLAB Algorithms*. New York: John Wiley & Sons, 1999.

[5] J. A. Jensen, S. I. Nikolov, K. L. Gammelmark, and M. H. Pedersen, "Synthetic aperture ultrasound imaging," *Ultrasonics*, vol. 44 Suppl 1, pp. e5-15, 2006.

[6] J. A. Jensen, *Imaging of Complex Media with coustic and Seismic Waves: Ultrasound imaging and its modeling*: Springer Verlag, 2002.

[7] S. Mallidi, T. Larson, J. Tam, P. P. Joshi, A. Karpiouk, K. Sokolov, and S. Emelianov, "Multiwavelength photoacoustic imaging and plasmon resonance coupling of gold nanoparticles for selective detection of cancer," *Nano Lett*, vol. 9, pp. 2825-31, 2009.

[8] K. H. Song, C. Kim, K. Maslov, and L. V. Wang, "Noninvasive in vivo spectroscopic nanorod-contrast photoacoustic mapping of sentinel lymph nodes," *Eur J Radiol*, vol. 70, pp. 227-31, 2009.

[9] W. J. Akers, C. Kim, M. Berezin, K. Guo, R. Fuhrhop, G. M. Lanza, G. M. Fischer, E. Daltrozzo, A. Zumbusch, X. Cai, L. V. Wang, and S. Achilefu, "Noninvasive photoacoustic and fluorescence sentinel lymph node identification using dye-loaded perfluorocarbon nanoparticles," *ACS Nano*, vol. 5, pp. 173-82, 2010.

[10] S.Kim, Y.-S. Chen, G.P. Luke, and S.Y. Emelianov, "In vivo three-dimensional spectroscopic photoacoustic imaging for monitoring nanoparticle delivery," *Biomedical Optics Express*, pp. in print, 2011.

[11] C. Lamagna, M. Aurrand-Lions, and B. A. Imhof, "Dual role of macrophages in tumor growth and angiogenesis," *J Leukoc Biol*, vol. 80, pp. 705-13, 2006.

[12] G. Pareek, E. R. Wilkinson, S. Bharat, T. Varghese, P. F. Laeseke, F. T. Lee, Jr., T. F. Warner, J. A. Zagzebski, and S. Y. Nakada, "Elastographic measurements of in-vivo radiofrequency ablation lesions of the kidney," *J Endourol*, vol. 20, pp. 959-64, 2006.

Bibliography

Aglyamov S, Skovoroda AR, Rubin JM, O'Donnell M, Emelianov SY. 2004. Model-based reconstructive elasticity imaging of deep venous thrombosis. *IEEE Trans Ultrason Ferroelectr Freq Control* 51: 521-31

Akers WJ, Kim C, Berezin M, Guo K, Fuhrhop R, et al. 2010. Noninvasive photoacoustic and fluorescence sentinel lymph node identification using dye-loaded perfluorocarbon nanoparticles. *ACS Nano* 5: 173-82

Arthur RM, Straube WL, Trobaugh JW, Moros EG. 2005. Non-invasive estimation of hyperthermia temperatures with ultrasound. *Int J Hyperthermia* 21: 589-600

Bamber JC, Hill CR. 1979. Ultrasonic attenuation and propagation speed in mammalian tissues as a function of temperature. *Ultrasound Med Biol* 5: 149-57

Basarab A, Liebgott H, Morestin F, Lyshchik A, Higashi T, et al. 2008. A method for vector displacement estimation with ultrasound imaging and its application for thyroid nodular disease. *Med Image Anal* 12: 259-74

Cespedes I, Huang Y, Ophir J, Spratt S. 1995. Methods for estimation of subsample time delays of digitized echo signals. *Ultrason Imaging* 17: 142-71

Chang JH, Yen JT, Shung KK. 2008. High-speed digital scan converter for high-frequency ultrasound sector scanners. *Ultrasonics* 48: 444-52

Chen H, Shi H, Varghese T. 2007. Improvement of elastographic displacement estimation using a two-step cross-correlation method. *Ultrasound Med Biol* 33: 48-56

Chen WR, Adams RL, Heaton S, Dickey DT, Bartels KE, Nordquist RE. 1995. Chromophore-enhanced laser-tumor tissue photothermal interaction using an 808-nm diode laser. *Cancer Lett* 88: 15-9

Chen X, Zohdy MJ, Emelianov SY, O'Donell M. 2004. Lateral speckle tracking using synthetic lateral phase. *IEEE Trans Ultrason Ferroelectr Freq Control* 51: 540-50

Cheong W-F, Prahl SA, Welch AJ. 1993. A review of the optical properties of biological tissues. *IEEE Quantum Electronics* 26: 2166-85

Christensen DA. 1988. *Ultrasonic bioinstrumentation*. New York: Wiley

Davis PH, Dawson JD, Riley WA, Lauer RM. 2001. Carotid Intimal-Medial Thickness Is Related to Cardiovascular Risk Factors Measured From Childhood Through Middle Age: The Muscatine Study. *Circulation* 104: 2815-9

Doyley MM, Bamber JC, Fuechsel F, Bush NL. 2001. A freehand elastographic imaging approach for clinical breast imaging: system development and performance evaluation. *Ultrasound Med Biol* 27: 1347-57

Duck FA. 1990. Physical properties of tissue. *Academic*

Erkamp RQ, Emelianov SY, Skovoroda AR, O'Donnell M. 2004. Nonlinear elasticity imaging: theory and phantom study. *IEEE Trans Ultrason Ferroelectr Freq Control* 51: 532-9

Feinstein SB. 2006. Contrast ultrasound imaging of the carotid artery vasa vasorum and atherosclerotic plaque neovascularization. *J Am Coll Cardiol* 48: 236-43

Foster SG, Embree PM, O'Brien WR. 1990. Flow velocity profile via time-domain correlation: error analysis and computer simulation. *IEEE Trans Ultrason Ferroelectr Freq Control* 37: 164-75

Fritz H. 1998. Evaluation of the digital rectal examination as a screening test for prostate cancer. Rotterdam section of the European Randomized Study of Screening for Prostate Cancer. *J. of National Cancer Inst.* 90: 1817-35

Fung YC. 1981. *Biomechanics: Mechanical properties of living tissues*. New York: Springer-Verlag

Garra BS, Cespedes EI, Ophir J, Spratt SR, Zuurbier RA, et al. 1997. Elastography of breast lesions: initial clinical results. *Radiology* 202: 79-86

Geiman BJ, Bohs LN, Anderson ME, Breit SM, Trahey GE. 2000. A novel interpolation strategy for estimating subsample speckle motion. *Phys Med Biol* 45: 1541-52

Hirsch LR, Stafford RJ, Bankson JA, Sershen SR, Rivera B, et al. 2003. Nanoshell-mediated near-infrared thermal therapy of tumors under magnetic resonance guidance. *Proc Natl Acad Sci U S A* 100: 13549-54

Huang X, El-Sayed IH, Qian W, El-Sayed MA. 2006. Cancer cell imaging and photothermal therapy in the near-infrared region by using gold nanorods. *J Am Chem Soc* 128: 2115-20

Huang X, Jain PK, El-Sayed IH, El-Sayed MA. 2008. Plasmonic photothermal therapy (PPTT) using gold nanoparticles. *Lasers Med Sci* 23: 217-28

Hwang JS, Song TK. 2001. A study of the display pixel-based focusing method in ultrasound imaging. *Ultrason Imaging* 23: 1-18

Institute ANS. 2000. American National Standard for the Safe Use of Lasers *ANSI Z136.1-2000, New York*

Jacques SL. 1993. Role of tissue optics and pulse duration on tissue effects during high-power laser irradiation. *Appl Opt* 32: 2447-54

Jensen JA. 2002. *Imaging of Complex Media with coustic and Seismic Waves: Ultrasound imaging and its modeling*: Springer Verlag

Jensen JA, Nikolov SI, Gammelmark KL, Pedersen MH. 2006. Synthetic aperture ultrasound imaging. *Ultrasonics* 44 Suppl 1: e5-15

Jiang J, Hall TJ. 2007. A parallelizable real-time motion tracking algorithm with applications to ultrasonic strain imaging. *Phys Med Biol* 52: 3773-90

Karlan BY. 1995. Ovarian cancer screening. The role of ultrasound in early detection. *Cancer* 76: 2011-5

Katouzian A, Sathyanarayana S, Baseri B, Konofagou EE, Carlier SG. 2008. Challenges in atherosclerotic plaque characterization with intravascular ultrasound (IVUS): from data collection to classification. *IEEE Trans Inf Technol Biomed* 12: 315-27

Kikoin IK. 1974. *Handbook of chemistry and physics*: CRC Press

Kim S, Aglyamov SR, Park S, O'Donnell M, Emelianov SY. 2011. An autocorrelation-based method for improvement of sub-pixel displacement estimation in ultrasound strain imaging. *IEEE Trans Ultrason Ferroelectr Freq Control* 58: 838-43

Kim S, Chen Y-S, Luke GP, Mehrmohammadi M, Cook JR, Emelianov SY. 2010. Ultrasound and photoacoustic image-guided photothermal therapy using silica-coated gold nanorods: in-vivo study. *in Proceedings of IEEE Conference on Ultrasonics, Ferroelectrics and Frequency Control (Institute of Electrical and Electronics Engineers, San Diego, 2010)*

Konig A, Margolis MP, Virmani R, Holmes D, Klauss V. 2008. Technology insight: in vivo coronary plaque classification by intravascular ultrasonography radiofrequency analysis. *Nat Clin Pract Cardiovasc Med* 5: 219-29

Konofagou E, Ophir J. 1998. A new elastographic method for estimation and imaging of lateral displacements, lateral strains, corrected axial strains and Poisson's ratios in tissues. *Ultrasound Med Biol* 24: 1183-99

Lai X, Torp H. 1999. Interpolation methods for time-delay estimation using cross-correlation method for blood velocity measurement. *IEEE Trans Ultrason Ferroelectr Freq Control* 46: 277-90

Lamagna C, Aurrand-Lions M, Imhof BA. 2006. Dual role of macrophages in tumor growth and angiogenesis. *J Leukoc Biol* 80: 705-13

Larina IV. 2005. Real-time optoacoustic monitoring of temperature in tissues. *Applied Physics* 38: 2633-9

Lerner RM, Huang SR, Parker KJ. 1990. "Sonoelasticity" images derived from ultrasound signals in mechanically vibrated tissues. *Ultrasound Med Biol* 16: 231-9

Li C, Wang LV. 2009. Photoacoustic tomography and sensing in biomedicine. *Phys Med Biol* 54: R59-97

Li M-L, Oh J-T, Xie X, Ku G, Wang W, et al. 2008. Simultaneous molecular and hypoxia imaging of brain tumors in vivo using spectroscopic photoacoustic tomography. *Proceedings of the IEEE* 96: 481-9

Li PC, Wang CR, Shieh DB, Wei CW, Liao CK, et al. 2008. In vivo photoacoustic molecular imaging with simultaneous multiple selective targeting using antibody-conjugated gold nanorods. *Opt Express* 16: 18605-15

Loo C, Lin A, Hirsch L, Lee MH, Barton J, et al. 2004. Nanoshell-enabled photonics-based imaging and therapy of cancer. *Technol Cancer Res Treat* 3: 33-40

Lubinski MA, Emelianov SY, O'Donnell M. 1999. Adaptive strain estimation using retrospective processing [medical US elasticity imaging]. *IEEE Trans Ultrason Ferroelectr Freq Control* 46: 97-107

Lubinski MA, Emelianov SY, O'Donnell M. 1999. Speckle tracking methods for ultrasonic elasticity imaging using short-time correlation. *IEEE Trans Ultrason Ferroelectr Freq Control* 46: 82-96

Luo J, Konofagou EE. 2009. Effects of various parameters on lateral displacement estimation in ultrasound elastography. *Ultrasound Med Biol* 35: 1352-66

Mallidi S, Larson T, Tam J, Joshi PP, Karpiouk A, et al. 2009. Multiwavelength photoacoustic imaging and plasmon resonance coupling of gold nanoparticles for selective detection of cancer. *Nano Lett* 9: 2825-31

Mallidi S, Wang B, Mehrmohammadi M, Qu M, Chen Y-S, et al. 2009. Ultrasound-based imaging of nanoparticles: from molecular and cellular imaging to therapy guidance. *Proceedings of the 2009 IEEE Ultrasonics Symposium*: 27-36

Marco R. 2002. Role of prostate fossa ultrasonography in the diagnosis of local recurrence after radical prostatectomy in case of PSA failure. *Associazione ricerche in urologia* 74: 304-8

Miller NR, Bamber JC, ter Haar GR. 2004. Imaging of temperature-induced echo strain: preliminary in vitro study to assess feasibility for guiding focused ultrasound surgery. *Ultrasound Med Biol* 30: 345-56

Miyagawa T, Tsutsumi M, Matsumura T, Kawazoe N, Ishikawa S, et al. 2009. Real-time elastography for the diagnosis of prostate cancer: evaluation of elastographic moving images. *Jpn J Clin Oncol* 39: 394-8

Miyanaga N, Akaza H, Yamakawa M, Oikawa T, Sekido N, et al. 2006. Tissue elasticity imaging for diagnosis of prostate cancer: a preliminary report. *Int J Urol* 13: 1514-8

Mucci R, Beranek B, Newman I, Cambridge MA. 1984. A comparison of efficient beamforming algorithms. *IEEE Transactions on Acoustics, Speech and Signal Processing* 32: 548-58

Nair A, Klingensmith JD, Vince DG. 2005. Real-time plaque characterization and visualization with spectral analysis of intravascular ultrasound data. *Stud Health Technol Inform* 113: 300-20

Nair A, Kuban BD, Tuzcu EM, Schoenhagen P, Nissen SE, Vince DG. 2002. Coronary plaque classification with intravascular ultrasound radiofrequency data analysis. *Circulation* 106: 2200-6

Nightingale KR, Palmeri ML, Nightingale RW, Trahey GE. 2001. On the feasibility of remote palpation using acoustic radiation force. *J Acoust Soc Am* 110: 625-34

Nikoobakht B, El-Sayed MA. 2003. Preparation and growth mechanism of gold nanorods (NRs) using seed-mediated growth method. *Chem. Mater* 15: 1957-62

Nissen SE, Yock P. 2001. Intravascular ultrasound: novel pathophysiological insights and current clinical applications. *Circulation* 103: 604-16

O'Donell M, Skovoroda AR, Shapo BM, Emelianov SY. 1994. Internal displacement and strain imaging using ultrasonic speckle tracking. *IEEE Trans Ultrason Ferroelectr Freq Control* 41: 314-25

O'Donnell M, Thomas LJ. 1992. Efficient synthetic aperture imaging from a circular aperture with possible application to catheter-based imaging. *IEEE Trans Ultrason Ferroelectr Freq Control* 39: 366-80

Ophir J, Alam SK, Garra B, Kallel F, Konofagou E, et al. 1999. Elastography: ultrasonic estimation and imaging of the elastic properties of tissues. *Proc Inst Mech Eng H* 213: 203-33

Ophir J, Cespedes I, Ponnekanti H, Yazdi Y, Li X. 1991. Elastography: a quantitative method for imaging the elasticity of biological tissues. *Ultrason Imaging* 13: 111-34

Oraevsky AA, Jacques SL, Tittel FK. 1997. Measurement of tissue optical properties by time-resolved detection of laser-induced transient stress. *Appl Opt* 36: 402-15

Oraevsky AA, Karabutov AA. 2003. *Optoacoustic tomography*

Pallwein L, Mitterberger M, Struve P, Pinggera G, Horninger W, et al. 2007. Real-time elastography for detecting prostate cancer: preliminary experience. *BJU Int* 100: 42-6

Pareek G, Wilkinson ER, Bharat S, Varghese T, Laeseke PF, et al. 2006. Elastographic measurements of in-vivo radiofrequency ablation lesions of the kidney. *J Endourol* 20: 959-64

Park S, Aglyamov SR, Emelianov SY. 2007. Elasticity imaging using conventional and high-frame rate ultrasound imaging: experimental study. *IEEE Trans Ultrason Ferroelectr Freq Control* 54: 2246-56

Park S, Aglyamov SR, Scott WG, Emelianov SY. 2007. Strain imaging using conventional and ultrafast ultrasound imaging: numerical analysis. *IEEE Trans Ultrason Ferroelectr Freq Control* 54: 987-95

Parpart S. 2007. Sensitivity and Specificity in Prostate Cancer Screening Methods and Strategies. *J. of Young Investigators* 16

Pesavento A, Perrey C, Krueger M, Ermert H. 1999. A time-efficient and accurate strain estimation concept for ultrasonic elastography using iterative phase zero estimation. *IEEE Trans Ultrason Ferroelectr Freq Control* 46: 1057-67

Prahl SA. Optical properties spectra compiled by Scott Prahl. *Available from: http://omlc.ogi.edu/spectra/*

R.Marco, Vincenzo S, Marco R, Paolo C, Francesco M, et al. 2002. Role of prostate fossa ultrasonography in the diagnosis of local recurrence after radical prostatectomy in case of PSA failure. *Associazione ricerche in urologia* 74: 304-8

Rubin JM, Xie H, Kim K, Weitzel WF, Emelianov SY, et al. 2006. Sonographic elasticity imaging of acute and chronic deep venous thrombosis in humans. *J Ultrasound Med* 25: 1179-86

S.Kim, Chen Y-S, Luke GP, Emelianov SY. 2011. In vivo three-dimensional spectroscopic photoacoustic imaging for monitoring nanoparticle delivery. *Biomedical Optics Express*: in print

Salomon G, Kollerman J, Thederan I, Chun FK, Budaus L, et al. 2008. Evaluation of prostate cancer detection with ultrasound real-time elastography: a comparison with step section pathological analysis after radical prostatectomy. *Eur Urol* 54: 1354-62

Sarvazyan AP, Rudenko OV, Swanson SD, Fowlkes JB, Emelianov SY. 1998. Shear wave elasticity imaging: a new ultrasonic technology of medical diagnostics. *Ultrasound Med Biol* 24: 1419-35

Schneider FK, Yoo YM, Agarwal A, Koh LM, Kim Y. 2006. New demodulation filter in digital phase rotation beamforming. *Ultrasonics* 44: 265-71

Schroder FH, van der Maas P, Beemsterboer P, Kruger AB, Hoedemaeker R, et al. 1998. Evaluation of the digital rectal examination as a screening test for prostate cancer. Rotterdam section of the European Randomized Study of Screening for Prostate Cancer. *J Natl Cancer Inst* 90: 1817-23

Seip R. 1995. Noninvasive estimation of tissue temperature response to heating fields using diagnostic ultrasound. *IEEE Trans Biomedical Engineering* 42: 828-39

Shah J, Aglyamov SR, Sokolov K, Milner TE, Emelianov SY. 2008. Ultrasound imaging to monitor photothermal therapy - feasibility study. *Opt Express* 16: 3776-85

Shah J, Park S, Aglyamov S, Larson T, Ma L, et al. 2008. Photoacoustic imaging and temperature measurement for photothermal cancer therapy. *J Biomed Opt* 13: 034024

Shukla R, Bansal V, Chaudhary M, Basu A, Bhonde RR, Sastry M. 2005. Biocompatibility of gold nanoparticles and their endocytotic fate inside the cellular compartment: a microscopic overview. *Langmuir* 21: 10644-54

Skovoroda AR, Emelianov SY, O'Donnell M. 1995. Tissue elasticity reconstruction based on ultrasonic displacementand strain images. *IEEE Transactions on Ultrasonics, Ferroelectrics and Frequency Control* 42: 747-65

Society AC. 2011. *Cancer Facts & Figures 2011*

Song KH, Kim C, Maslov K, Wang LV. 2009. Noninvasive in vivo spectroscopic nanorod-contrast photoacoustic mapping of sentinel lymph nodes. *Eur J Radiol* 70: 227-31

Soumekh M. 1999. *Synthetic Aperture Radar. Signal Processing with MATLAB Algorithms*. New York: John Wiley & Sons

Teh W. 1998. The role of ultrasound in breast cancer screening. A consensus statement by the european group for breast cancer screening. *European Journal of Cancer* 34: 449-50

Terris MK. 1999. Sensitivity and specificity of sextant biopsies in the detection of prostate cancer: preliminary report. *Urology* 54: 486-9

Tsutsumi M, Miyagawa T, Matsumura T, Kawazoe N, Ishikawa S, et al. 2007. The impact of real-time tissue elasticity imaging (elastography) on the detection of prostate cancer: clinicopathological analysis. *Int J Clin Oncol* 12: 250-5

Varghese T, Zagzebski JA, Chen Q, Techavipoo U, Frank G, et al. 2002. Ultrasound monitoring of temperature change during radiofrequency ablation: preliminary in-vivo results. *Ultrasound Med Biol* 28: 321-9

Viola F, Walker WF. 2005. A spline-based algorithm for continuous time-delay estimation using sampled data. *IEEE Trans Ultrason Ferroelectr Freq Control* 52: 80-93

Wang B, Su JL, Amirian J, Litovsky SH, Smalling R, Emelianov S. 2010. Detection of lipid in atherosclerotic vessels using ultrasound-guided spectroscopic intravascular photoacoustic imaging. *Opt Express* 18: 4889-97

Wang CC, Deng JM, Ateshian GA, Hung CT. 2002. An automated approach for direct measurement of two-dimensional strain distributions within articular cartilage under unconfined compression. *J Biomech Eng* 124: 557-67

Wang L, Jacques SL, Zheng L. 1995. MCML--Monte Carlo modeling of light transport in multi-layered tissues. *Comput Methods Programs Biomed* 47: 131-46

Wang L, Jacques SL, Zheng L. 1997. CONV--convolution for responses to a finite diameter photon beam incident on multi-layered tissues. *Comput Methods Programs Biomed* 54: 141-50

Wang LV. 2009. *Photoacoustic imaging and spectroscopy*

Wang LV, Wu HI. 2007. *Biomedical optics - Principles and imaging*: Wiley

Yamakoshi Y, Sato J, Sato T. 1990. Ultrasonic imaging of internal vibration of soft tissue under forced vibration. *IEEE Trans Ultrason Ferroelectr Freq Control* 37: 45-53

Yang X, Skrabalak SE, Li ZY, Xia Y, Wang LV. 2007. Photoacoustic tomography of a rat cerebral cortex in vivo with au nanocages as an optical contrast agent. *Nano Lett* 7: 3798-802

Zahiri-Azar R, Salcudean SE. 2006. Motion estimation in ultrasound images using time domain cross correlation with prior estimates. *IEEE Trans Biomed Eng* 53: 1990-2000

Zhu QL, Jiang YX, Liu JB, Liu H, Sun Q, et al. 2008. Real-time ultrasound elastography: its potential role in assessment of breast lesions. *Ultrasound Med Biol* 34: 1232-8

Vita

Seungsoo Kim was born in Seoul, Korea, on June 19, 1979. He graduated with honors from Sogang University, Seoul, Korea for his both Bachelor of Science and Master of Science in Electronic Engineering in 2005 and 2007, respectively. He started ultrasound-related researches from 2005 as a M.S. student at Sogang University and continued his research at the University of Texas at Austin, Austin, TX, USA as a Ph.D. student. During his master studies, he concentrated on ultrasound beamforming, especially for synthetic aperture focusing. During his doctoral studies, he focused on ultrasound and photoacoustic imaging, especially for ultrasound elasticity imaging and spectroscopic photoacoustic imaging. The results of his work were presented at 3 international conferences. He wrote 2 first-author papers on journals. One more first-author paper is in preparation for the journal publication. In addition, he was a contributor to 9 journal papers as a co-author. He was a recipient of William S. Livingston Outstanding Graduate Student Academic Employee Award for Teaching Assistant in 2010 and Professional Development Award in 2011 from the University of Texas at Austin. After his graduation, he will join Siemens Healthcare in Issaquah, WA as a senior ultrasound systems engineer.

Permanent address: seungsookim@utexas.edu
This dissertation was typed by Seungsoo Kim.